Springer Theses
Recognizing Outstanding Ph.D. Research

James A. Dolan

Gyroid Optical Metamaterials

Solvent Vapour Annealing, Confined Crystallisation, and Optical Anisotropy

Springer

Springer Theses

Recognizing Outstanding Ph.D. Research

Aims and Scope

The series "Springer Theses" brings together a selection of the very best Ph.D. theses from around the world and across the physical sciences. Nominated and endorsed by two recognized specialists, each published volume has been selected for its scientific excellence and the high impact of its contents for the pertinent field of research. For greater accessibility to non-specialists, the published versions include an extended introduction, as well as a foreword by the student's supervisor explaining the special relevance of the work for the field. As a whole, the series will provide a valuable resource both for newcomers to the research fields described, and for other scientists seeking detailed background information on special questions. Finally, it provides an accredited documentation of the valuable contributions made by today's younger generation of scientists.

Theses are accepted into the series by invited nomination only and must fulfill all of the following criteria

- They must be written in good English.
- The topic should fall within the confines of Chemistry, Physics, Earth Sciences, Engineering and related interdisciplinary fields such as Materials, Nanoscience, Chemical Engineering, Complex Systems and Biophysics.
- The work reported in the thesis must represent a significant scientific advance.
- If the thesis includes previously published material, permission to reproduce this must be gained from the respective copyright holder.
- They must have been examined and passed during the 12 months prior to nomination.
- Each thesis should include a foreword by the supervisor outlining the significance of its content.
- The theses should have a clearly defined structure including an introduction accessible to scientists not expert in that particular field.

More information about this series at http://www.springer.com/series/8790

James A. Dolan

Gyroid Optical Metamaterials

Solvent Vapour Annealing, Confined Crystallisation, and Optical Anisotropy

Doctoral Thesis accepted by
the University of Cambridge, Cambridge, UK

Springer

Author
Dr. James A. Dolan
University of Cambridge
Cambridge, UK

Supervisors
Prof. Ullrich Steiner
Soft Matter Physics Group, Adolphe Merkle Institute
University of Fribourg
Fribourg, Switzerland

Prof. Jeremy J. Baumberg
NanoPhotonics Centre, Cavendish Laboratory
University of Cambridge
Cambridge, UK

Prof. Timothy D. Wilkinson
Centre of Molecular Materials for Photonics and Electronics, Department of Engineering
University of Cambridge
Cambridge, UK

ISSN 2190-5053 ISSN 2190-5061 (electronic)
Springer Theses
ISBN 978-3-030-03010-0 ISBN 978-3-030-03011-7 (eBook)
https://doi.org/10.1007/978-3-030-03011-7

Library of Congress Control Number: 2018958933

© Springer Nature Switzerland AG 2018
This work is subject to copyright. All rights are reserved by the Publisher, whether the whole or part of the material is concerned, specifically the rights of translation, reprinting, reuse of illustrations, recitation, broadcasting, reproduction on microfilms or in any other physical way, and transmission or information storage and retrieval, electronic adaptation, computer software, or by similar or dissimilar methodology now known or hereafter developed.
The use of general descriptive names, registered names, trademarks, service marks, etc. in this publication does not imply, even in the absence of a specific statement, that such names are exempt from the relevant protective laws and regulations and therefore free for general use.
The publisher, the authors and the editors are safe to assume that the advice and information in this book are believed to be true and accurate at the date of publication. Neither the publisher nor the authors or the editors give a warranty, express or implied, with respect to the material contained herein or for any errors or omissions that may have been made. The publisher remains neutral with regard to jurisdictional claims in published maps and institutional affiliations.

This Springer imprint is published by the registered company Springer Nature Switzerland AG
The registered company address is: Gewerbestrasse 11, 6330 Cham, Switzerland

Everything stinks till it's finished.

—Dr. Seuss

Dedicated to
Douglas William Richard Tate
1934–2005
Engineer, teacher, friend.

Supervisor's Foreword

The concept of a "left-handed" or negative-index material was first proposed by Victor Veselago in 1968 through his theoretical predictions of the electrodynamic behaviour of materials that simultaneously exhibit negative values of dielectric permittivity and magnetic permeability. Thirty years later, John B. Pendry demonstrated that artificial electromagnetic materials—"metamaterials"—consisting, in this case, of interpenetrated ordered arrays of wires and split-ring resonators could also exhibit similar phenomena. Initially demonstrated for microwave radiation, metamaterials have borne out Pendry's predictions, and the quest since then has been their implementation in the visible range of the electromagnetic spectrum. Whilst the physical principles are scale-invariant, practical realisation of the sub-wavelength structural elements that constitute an optical metamaterial is far from trivial, as it requires periodic arrays of well-defined structural features in three dimensions on the 10–50 nm length scale. Nearly all approaches so far employ some type of lithographic method, which is not well suited for the manufacture of 3D architectures on such small length scales.

James Dolan's thesis makes an important contribution to the quest for optical metamaterials. As opposed to "top-down" lithographic methods, his thesis explores "bottom-up" polymer self-assembly methods for the manufacture of 3D metamaterials in the visible range of the spectrum. This methodology, however, presents the researcher with a new set of challenges. First, macromolecular self-assembly must be controlled with a hitherto unprecedented level of precision. This is difficult not only from a thermodynamic point of view, but also because the outcome of self-assembly is "invisible". Since molecular self-assembly takes place on the sub-100 nm length scale, the morphologies attained cannot be probed by optical microscopy. Whilst X-ray scattering and electron and atomic force microscopy are all possible, the lack of optical methods is cumbersome for the experimenter. The first part of the thesis addresses these two challenges: the control of polymer self-assembly in thin films and the optical visualisation of its structural perfection. Chapter 4 explores in detail the structural evolution of block copolymer films that are exposed to a solvent atmosphere in the so-called solvent vapour annealing experiment. The results of this chapter provide the thermodynamic basis for the

control over polymer self-assembly that is required to fabricate optical metamaterials. The following chapter, Chap. 5, tackles the "invisibility" issue. By exploiting the crystallisation of one of the copolymer blocks, the lateral organisation of the self-assembled morphology gives rise to birefringence. This chapter carefully investigates this effect and develops a model that directly links the birefringence to the structural organisation, thereby offering a valuable new tool to optimise polymer self-assembly for the manufacture of optical metamaterials. This chapter also, for the first time, demonstrates 100 μm large domains of the self-assembled gyroid morphology, from which some of the most interesting metamaterial properties are predicted to arise.

The second part of the thesis focuses on the optical properties of metamaterials created by polymer self-assembly. To this end, the copolymer morphologies were partially voided and then replicated into a plasmonic metal (gold). Chapter 6 explores the question of whether long-range order in this optical metamaterial is required. By combining experimental studies, simulations, and analytical calculations, this chapter explores the optical response of locally-ordered gyroid morphologies that are disordered on the micrometre-length scale. The finding that the optical spectra of these disordered gyroids are well described by an effective medium model illustrates, on the one hand, that order is required to access the most interesting aspects of optical metamaterials, but also, on the other hand, that these materials have interesting properties in their own right (e.g. a change of sign in the permittivity as a function of wavelength). The final experimental chapter, Chap. 7, solves a long-standing puzzle in the field of self-assembled optical metamaterials, thereby providing an important stepping stone in metamaterial research. The puzzle in question is the strong linear dichroism of gyroid metamaterials, which is unexpected given the cubic nature of the gyroid unit cell. By combining experimental observations with numerical simulations, this chapter demonstrates that gyroid samples can be considered as a bulk metamaterial terminated by a distinct metasurface—the 2D equivalent of a metamaterial. It is the symmetry-breaking of the metasurface that induces the strong, experimentally observed linear dichroism. Importantly, this chapter uncovers that the in-coupling and out-coupling of light to and from the metamaterial depend extremely sensitively on the specific surface termination of the metamaterial. The control of such terminations will require a manufacturing precision of around 1 nm, thereby setting a high bar for the reliable manufacture of optical metamaterials for visible wavelengths.

The scalable manufacture of optical metamaterials with a negative refractive index has the potential for transformative changes in the application of optical materials, utilising, for example, their super-focusing and "cloaking" properties. This thesis demonstrates, on the one hand, that the manufacture of these materials by self-assembly is a promising way forward. On the other hand, the results of the

four main thesis chapters elucidate the significant challenges in mastering this approach, thereby setting future researchers a set of challenging tasks that they will have to overcome on the path to the demonstration and use of optical metamaterial effects visible to the naked eye.

Fribourg, Switzerland
October 2018

Prof. Ullrich Steiner
Soft Matter Physics Group
Adolphe Merkle Institute
University of Fribourg

Abstract

The optical properties of matter are intrinsically linked to morphology. It is the vast range of possible forms, structures, and arrangements of matter, across various different length scales, which give rise to the great wealth of optical phenomena we observe. In this thesis, the interplay between optics and morphology in gyroid-structured optical metamaterials, and the triblock terpolymers from which they are fabricated, is explored.

Optical metamaterials are artificially engineered materials which, by virtue of their sub-wavelength structure and not only their chemical composition, may exhibit various electromagnetic properties not otherwise encountered in nature (e.g. negative refraction). Triblock terpolymers are a class of polymer consisting of three chemically distinct monomer types grouped together into "blocks". Their self-assembly is a particularly promising means to fabricate intricate one-, two-, and three-dimensional morphologies on the nanometre length scale, from which optical metamaterials may be fabricated. The gyroid is one such morphology, a three-dimensional, cubic, and chiral triply periodic network possessing a constant mean curvature surface. These unique geometrical properties impart to gyroid optical metamaterials a range of interesting optical properties (e.g. linear and circular dichroism). However, these anisotropic optical properties are only evident when the long-range order of the self-assembled triblock terpolymer template is sufficient.

As demonstrated in this thesis, the long-range order of a gyroid-forming triblock terpolymer is significantly improved by solvent vapour annealing. An in situ grazing-incidence small-angle X-ray scattering study revealed that the gyroid phase is remarkably robust during annealing and that the unit cell size and long-range order can be controlled by swelling and quenching the terpolymer appropriately. Additionally, unique confined crystallisation behaviour of the semicrystalline block of the terpolymer is observed in templates fabricated via solvent vapour annealing. The gyroid network, to which the semicrystalline block is confined, preferentially aligns the polymer crystallites along directions of fastest growth, resulting in a striking and unexpected uniform birefringence.

Whereas gyroid optical metamaterials which exhibit only short-range order are shown to be optically equivalent to amorphous nanoporous gold, those fabricated from templates with good long-range order exhibit a strong linear dichroism. Although previously observed, the linear dichroism is unexpected for an optical metamaterial with cubic symmetry. Characterisation of the dichroism and comparison with simulations allows its underlying physical mechanism to be revealed. It is the termination surface of the gyroid optical metamaterial which breaks the symmetry of the bulk morphology and results in a strongly anisotropic optical response.

These results highlight the crucial importance of fabricating triblock terpolymer templates with good long-range order for optical metamaterial applications. Solvent vapour annealing is demonstrated to be one way of achieving such order. The resulting terpolymer templates and gyroid optical metamaterials both reveal the potential for deep sub-wavelength features, molecular anisotropy and surface termination, respectively, to have a striking effect upon the bulk optics of the materials.

Acknowledgements

It feels odd to precede something so technical with something so sentimental. However, as it is rare to get such an opportunity to acknowledge those people who have contributed, one way or another, to the process resulting in this thesis, I intend to take full advantage of it. I therefore ask the reader to allow me this little indulgence.

Over the last few years, I have had the great pleasure of becoming part of three different research groups. The first, the Centre of Molecular Materials for Photonics and Electronics (CMMPE) in the Department of Engineering, University of Cambridge, has been my "home" throughout the Ph.D. CMMPE was, and perhaps still remains, the envy of the building for its relaxed and sociable atmosphere, engendered in no small part by my supervisor, the inimitable Tim Wilkinson. I remain grateful to Tim for first accepting me as a student, and to the whole group for the help, support, and friendship provided to me during my tenure. Particular thanks must therefore go to Alex Macfaden, Ammar Khan, Calum Williams, Ananta Palani, Rachel Garsed, Philip Garsed, and George Gordon for the innumerable lunches, coffee breaks, evenings, and weekends which made my time in both Cambridge and CMMPE such an absolute delight.

The second group of which I was a part was the Thin Films and Interfaces Group (TFI) in the Department of Physics, University of Cambridge, latterly the Soft Matter Physics Group, Adolphe Merkle Institute, Switzerland. As the challenges associated with sample fabrication became increasingly clear, I ended up spending more time amongst this group than I (perhaps anyone) had originally envisioned. However, as such, there are a number of members of this group who deserve and require particular recognition.

Firstly, I must thank Raphael Dehmel, a fellow Ph.D. student one year my senior, whose shadow looms large over the entirety of this thesis. Raph and I worked closely together on much of the content herein, and I cannot overstate how fruitful and enjoyable I found this collaboration to be. Indeed, without Raph's frequent and invaluable input, and his seemingly limitless practical knowledge, I doubt very much that anywhere near the equivalent progress would have been

made. I learnt a huge amount from our almost daily interactions and cannot therefore thank him enough.

Secondly, I would like to thank Bodo Wilts and Ilja Gunkel, two postdocs, latterly an Ambizione Fellow and Marie Skłodowska-Curie Fellow, respectively. Bodo has known me since the very start of my Ph.D. and helped co-author, with infinite patience, my first papers on the topics of this thesis. A ruthless editor, he has contributed greatly to both the quality of my writing and my optics research. Ilja, with whom I co-authored my first successful beamtime proposal, similarly deserves significant thanks for his endless patience and encouragement, whilst I grappled with the basics of polymer physics and the subtleties of writing about it. Bodo and Ilja have together provided truly incredible support during the writing of this thesis, for which I can only reiterate my most heartfelt thanks.

Finally, I would like to thank Ulli Steiner, who accepted me as a student whilst he was still in Cambridge and continued to provide wonderful supervision even after (indeed despite) his move to Switzerland. I suspect that Ulli, as a co-supervisor, did not expect to see quite as much of me as he did, but he was nonetheless inordinately attentive and supportive, far beyond any reasonable expectations. I am therefore supremely grateful for the generosity, kindness, and ongoing support he has shown me over the years.

Of course, the TFI group consisted of more than the above four, and I have to thank all remaining members for their friendship and help over the years. Karl Gödel, Harry Beeson, Jonathan Lim, and Tobey Wenzel in Cambridge deserve particular thanks, so too does Karolina Korzeb in Switzerland.

The third group of which I was a part was the NanoPhotonics Centre (NP) in the Department of Physics, University of Cambridge. Despite my very best intentions, I fear I was a rather spectral presence in the group, and it is to their immense credit that Will Deacon, Marie-Elena Kleeman, Cloudy Carnegie, Yago Valle-Inclán Redondo, and Sean Cormier were so very welcoming and such wonderful company whenever I happened to appear. I immensely enjoyed my time spent in NP and am therefore truly grateful to Jeremy Baumberg for both the opportunity to do so and the excellent supervision and guidance I have received from him since, once again far exceeding what I might reasonably have expected.

Jeremy also deserves additional thanks for running the Nanotechnology Doctoral Training Centre (NanoDTC), through which I was admitted to Cambridge. It is because of the NanoDTC's commitment to interdisciplinary research that I had the privilege of becoming part of three groups across two departments, and the opportunity therefore of co-supervision by Tim, Ulli, and Jeremy. It has become increasingly clear to me that the atmosphere of the NanoDTC, its vibrancy and efficiency, which make being part of it such a joy, is almost entirely down to Jeremy. He thus deserves particular recognition and thanks for the enthusiasm and dedication with which he fills this role. That said, the NanoDTC would not be the same without the additional and tireless efforts of its teaching fellows, Aga Iwasiewicz-Wabnig and, latterly, Karishma Jain, both of whom I would like to thank for their care and attentiveness over the years.

Of course, there are countless others to whom thanks are owed, for their collaboration and friendship; due to brevity, my efforts here will necessarily appear paltry. These include: Ortwin Hess, Matthias Saba, Angela Demetriadou, and Sang Soon Oh (Imperial College); Giovanni Offeddu, Laurie Young, Silvia Vignolini, and Matt Cole (Cambridge); Jackie Ouchikh and Rob Doubleday (Centre for Science and Policy); and Patrick Wollner, Harry Armstrong, Helen Ewles, Dave Bosworth, Fiona Docherty, Joe Gladstone, Tim Guilliams, and Alberto García-Mogollón (Cambridge University Science and Policy Exchange). Interactions with all of the above greatly enriched my time here in Cambridge, for which I am most deeply grateful.

Although this thesis was conceived in Cambridge, it was born in Orkney. I must therefore thank Ruta Noreika for so kindly allowing me use of the "peedie hoose" from which to write, and Debbie Davidson, Maurice Davidson, Zoe Davidson, and Cinta for their friendship whilst there.

I was sustained throughout the Ph.D., as I am at all times, by my closest friends and family. The members of my family (families), despite all they have done for me, are too numerous to thank individually. However, I must at least mention my parents, Mum (Penni), Dad (Andrew), and Mütyi (Agnes), without whose unconditional love and acceptance I could never have come this far. I can but hope that they are proud. Thankfully, my closest friends are fewer in number. I can therefore thank, from the very bottom of my heart, Alex Macfaden, Lewis Roy, Jamie Holwill, and James Golding for their endless (and frankly unfathomable) affection and support over many years. I cannot express how much their friendship means to me, although I often try.

Above all, I would like to thank Marco, the only person with whom I would gladly abandon academia to start a tropical bird sanctuary. All that I could write he (hopefully) already knows.

Contents

1 Preamble 1
References 2

2 Introduction 5
2.1 Gyroids 5
2.1.1 Level Surfaces 6
2.1.2 Gyroid Surface 6
2.1.3 Single Gyroid 7
2.1.4 Double Gyroid 8
2.2 Block Copolymer Self-assembly 8
2.2.1 Diblock Copolymers 10
2.2.2 Triblock Terpolymers 12
2.3 Solvent Vapour Annealing 15
2.3.1 Diblock Copolymers 16
2.3.2 Triblock Copolymers and Terpolymers 16
2.3.3 Gyroid-Forming Block Copolymers 17
2.4 Block Copolymer Crystallisation 18
2.4.1 Spherulites 19
2.4.2 Crystallisation Temperature 19
2.4.3 Gyroid-Forming Block Copolymers 20
2.5 Metamaterials 21
2.6 Gyroid Optical Metamaterials 22
2.6.1 Fabrication 22
2.6.2 Optical Properties 23
2.6.3 Simulations and Theoretical Description 25
References 30

3 Methods 37
3.1 Terpolymer Thin Films 37
3.2 Differential Scanning Calorimetry 38

3.3 Annealing . . . 38
3.3.1 Thermal Annealing . . . 38
3.3.2 In Situ Solvent Vapour Annealing . . . 38
3.3.3 Ex Situ Solvent Vapour Annealing . . . 39
3.4 Film Thickness Measurements . . . 40
3.5 Grazing-Incidence Small- and Wide-Angle X-Ray Scattering . . . 40
3.5.1 Paul Scherrer Institute . . . 40
3.5.2 Cornell High Energy Synchrotron Source . . . 41
3.5.3 Data Analysis . . . 41
3.6 Electrodeposition of Gold . . . 41
3.7 Optical Characterisation . . . 42
3.7.1 Optical Microscopy . . . 42
3.7.2 Reflection Goniometry . . . 42
3.7.3 Transmission Goniometry . . . 43
3.8 Optical Simulations . . . 43
References . . . 44

Part I Solvent Vapour Annealing of a Gyroid-Forming Triblock Terpolymer

4 In Situ GISAXS During Solvent Vapour Annealing of a Gyroid-Forming ISO Triblock Terpolymer . . . 47
4.1 Methods . . . 47
4.2 Results . . . 48
4.2.1 Solvent Vapour Annealing (SVA) Regimes . . . 48
4.2.2 Effect of Maximum Swelling Ratio and Solvent Removal Rate . . . 52
4.2.3 Effect of Different Solvent and Mixed Solvent Vapours . . . 57
4.3 Discussion . . . 61
4.3.1 Alternating Gyroid Morphology . . . 62
4.3.2 Robust Morphology and Flexible Unit Cell Size . . . 63
4.4 Conclusion . . . 65
References . . . 66

5 Preferentially Aligned Crystallisation Within a Single Gyroid Network of an ISO Triblock Terpolymer . . . 67
5.1 Methods . . . 68
5.2 Results . . . 68
5.2.1 Crystalline Superstructure . . . 69
5.2.2 Microphase-Separated Morphology . . . 71
5.2.3 Correlation of Crystalline Superstructure with Microphase-Separated Morphology . . . 75
5.3 Discussion . . . 76

5.3.1 Confined Crystallisation . . . 77
5.3.2 Multiple Individually Aligned Crystallites . . . 77
5.3.3 Crystallite Orientation Perpendicular to the Long Axis of the Gyroid Channels . . . 78
5.3.4 Preferentially Aligned Crystallisation Along the ⟨111⟩ and ⟨100⟩ Directions . . . 79
5.3.5 Distribution of Local Crystallite Orientations About the ⟨111⟩ and ⟨100⟩ Directions . . . 79
5.4 Conclusion . . . 82
References . . . 82

Part II Optical Anisotropy in Gyroid Optical Metamaterials

6 Multi-Domain Gyroid Optical Metamaterials . . . 87
6.1 Methods . . . 88
6.2 Effective Medium Theories . . . 88
6.2.1 Maxwell-Garnett Theory: Spherical Inclusions . . . 88
6.2.2 Bruggeman Theory: Spherical Inclusions . . . 90
6.2.3 Bruggeman Theory: Ellipsoidal Inclusions . . . 90
6.2.4 Model Fitting . . . 91
6.3 Results . . . 92
6.3.1 Multi-Domain Gyroid Optical Metamaterials . . . 92
6.3.2 Effective Medium Models . . . 93
6.3.3 Host Refractive Index and Volume Fill Fraction . . . 96
6.4 Discussion . . . 98
6.4.1 Bruggeman Random Wire Array . . . 99
6.4.2 Effective Permittivity and Nanoporous Gold . . . 101
6.4.3 Gyroid Surface and Morphology Effects . . . 102
6.5 Conclusion . . . 103
References . . . 103

7 Single-Domain Gyroid Optical Metamaterials . . . 105
7.1 Methods . . . 105
7.2 Results . . . 106
7.2.1 Fabricated Morphology and Terminations . . . 106
7.2.2 Experimental Dichroism . . . 109
7.2.3 Uniform Terminations . . . 111
7.2.4 Anisotropic Effective Medium Layer . . . 114
7.2.5 Accounting for Non-uniform Terminations . . . 117
7.3 Discussion . . . 118
7.3.1 Deep Sub-wavelength Sensitivity . . . 119
7.3.2 Nature of the Linear Dichroism . . . 119
7.3.3 Distribution of Terminations . . . 120
7.3.4 Termination-Induced Anisotropy . . . 122

7.4 Conclusion 123
References 124

8 Conclusion and Outlook 125
8.1 Solvent Vapour Annealing of a Gyroid-Forming Triblock Terpolymer 125
8.2 Optical Anisotropy in Gyroid Optical Metamaterials 126
8.3 Outlook 127
References 129

Curriculum Vitae 131

Chapter 1
Preamble

The optical properties of matter are intrinsically linked to morphology. It is the vast range of possible forms, structures, and arrangements of matter, and their characteristic length scales, which give rise to the great wealth of optical phenomena we observe. At the atomic length scale, the amorphous or crystalline arrangement of atoms and their associated electronic interactions give rise to the refractive indices of a material and determine the existence and nature of the electronic band gap and the associated optical transitions [1]. Significantly larger than the atomic length scale but still below the length scale of visible light, one can define and arrange synthetic "meta-atoms" or "meta-molecules". From these it is possible to construct a "metamaterial", an artificially engineered material designed to possess chosen electromagnetic properties not otherwise found in nature [2–4]. Alternatively, at the length scale of visible light, constructive and destructive interference resulting from cumulative interfacial reflections within a material can give rise to photonic crystal effects and the associated photonic band gaps [5–8]. A fascinating morphology may therefore lead to fascinating optics, the underlying mechanism of which will depend sensitively on the length scale of that morphology. In this thesis, the interplay between optics and morphology in gyroid-structured optical metamaterials, and the triblock terpolymers from which they are fabricated, is explored.

Discovered in 1970 by Alan Schoen, the "Schoen G" or "gyroid" surface is a triply periodic minimal surface of genus three [9, 10]. It possesses a constant mean curvature of zero and is periodic in all three principal spatial directions [11]. It also possesses no reflection symmetries and exhibits an array of continuous channels along different principal crystallographic axes [12]. Its name derives from the observation that each continuous channel in the structure has connections to additional channels which "gyrate" along their length. These channels join as triads throughout the overall structure [13–15]. Closely related to, and derived from, the gyroid surface, are the single and double gyroid morphologies. The unique geometrical properties exhibited by the gyroid surface and its related morphologies ensure gyroid-structured materials are a particularly fascinating case study of the complex relationship between

© Springer Nature Switzerland AG 2018

J. A. Dolan, *Gyroid Optical Metamaterials*, Springer Theses,
https://doi.org/10.1007/978-3-030-03011-7_1

morphology and optical properties. Indeed, it is therefore unsurprising that such a rich variety of optical phenomena, from linear and circular dichroism to the recent prediction and observation of Weyl points and line nodes, should be observed in gyroid-structured materials [16–18].

Gyroid optical metamaterials are fabricated via the self-assembly of triblock terpolymers. The study of the optical properties of gyroid optical metamaterials is therefore impossible without the ability to successfully and reliably control the self-assembly of this particular class of macromolecule. However, although the aim may be simply to engineer the desired morphology on a particular length scale, much fascinating polymer physics may be gleaned in the process. In this thesis, the physics and engineering associated with both the fabrication (Part I) and characterisation (Part II) of gyroid optical metamaterials are therefore investigated.

The theory and literature relevant to block copolymer self-assembly, the confined crystallisation behaviour of amorphous-semicrystalline block copolymers (the class of copolymer used here), and a particularly promising means by which to encourage long-range order during their self-assembly, solvent vapour annealing, are first briefly reviewed (Chap. 2). So too are the existing theory and literature relevant to the optical properties of the resulting gyroid optical metamaterials (Chap. 2). The experimental methods used to fabricate, characterise, and simulate gyroid-forming triblock terpolymer thin films and gyroid optical metamaterials are also introduced (Chap. 3). Thereafter, experimental results contributing to our understanding of the polymer physics and optics of gyroid-structured materials are presented: in Part I, an in situ study of the thermodynamics and kinetics of a triblock terpolymer under the action of solvent vapour annealing, and an ex situ study of the confined crystallisation mechanism in the resulting solvent-annealed terpolymer thin films (Chaps. 4 and 5); and in Part II, a study of the isotropic and anisotropic optical properties of gyroid optical metamaterials possessing both short- and long-range order, respectively (Chaps. 6 and 7).

References

1. Hecht, E. (1997). *Optics*. Boston: Addison Wesley Publishing Company. ISBN 0201838877.
2. Capolino, F. (2009). *Applications of metamaterials*. Florida: CRC Press. ISBN 1420054236.
3. Pendry, J. B., Holden, A. J., Stewart, W. J., & Youngs, I. (1996). Extremely low frequency plasmons in metallic mesostructures. *Physical Review Letters*, *76*, 4773–4776.
4. Shelby, R. A., Smith, D. R., & Schultz, S. (2001). Experimental verification of a negative index of refraction. *Science*, *292*, 77–79.
5. Fleming, J. G., Lin, S. Y., El-Kady, I., Biswas, R., & Ho, K. M. (2002). All-metallic threedimensional photonic crystals with a large infrared bandgap. *Nature*, *417*, 1548–1551.
6. Maldovan, M., & Thomas, E. L. (2004). Diamond-structured photonic crystals. *Nature Materials*, *3*, 593–600.
7. Vukusic, P., & Sambles, J. R. (2003). Photonic structures in biology. *Nature*, *424*, 852–855.
8. Joannopoulos, J. D., Johnson, S. G., Winn, J. N., & Meade, R. D. M. (2008). *Photonic crystals: Molding the flow of light*. New Jercy: Princeton University Press. ISBN 0691124566.
9. Schoen, A. H. (1970). *Infinite periodic minimal surfaces without self-intersections*. Technical Notes TN D-5541, NASA.

10. Schoen, A. H. (2012). Reflections concerning triply-periodic minimal surfaces. *Interface Focus*, *2*, 658–668.
11. Hyde, S. (1997). *The language of shape: The role of curvature in condensed matter: Physics, chemistry and biology*. Amsterdam: Elsevier. ISBN 0444815384.
12. Wohlgemuth, M., Yufa, N., Hoffman, J., & Thomas, E. L. (2001). Triply periodic bicontinuous cubic microdomain morphologies by symmetries. *Macromolecules*, *34*, 6083–6089.
13. Michielsen, K., & Stavenga, D. G. (2008). Gyroid cuticular structures in butterfly wing scales: Biological photonic crystals. *Journal of the Royal Society Interface*, *5*, 85–94.
14. Saranathan, V., Osuji, C. O., Mochrie, S. G. J., Noh, H., & Narayanan, S. (2010). Structure, function, and self-assembly of single network gyroid (I4132) photonic crystals in butterfly wing scales. *Proceedings of the National Academy of Sciences*, *107*, 11676–11681.
15. Schröder-Turk, G. E., Wickham, S., Averdunk, H., Brink, F., Fitz Gerald, J. D., Poladian, L., et al. (2011). The chiral structure of porous chitin within the wing-scales of Callophrys rubi. *Journal of Structural Biology*, *174*, 290–295.
16. Saba, M., Thiel, M., Turner, M. D., & Hyde, S. T. (2011). Circular dichroism in biological photonic crystals and cubic chiral nets. *Physical Review Letters*, *103902*, 1–4.
17. Lu, L., Fu, L., Joannopoulos, J. D., & Soljac, M. (2013). Weyl points and line nodes in gyroid photonic crystals. *Nature Photonics*, *7*, 294–299.
18. Lu, L., Wang, Z., Ye, D., Ran, L., Fu, L., Joannopoulos, J. D., et al. (2015). Experimental observation of Weyl points. *Science*, *349*(101), 622–624.

Chapter 2
Introduction

The gyroid optical metamaterials presented in this thesis were all fabricated via self-assembly of a triblock terpolymer. However, only single-domain gyroid optical metamaterials (i.e. those for which the terpolymer template exhibits sufficient long-range order) exhibit the most interesting optical properties. It is therefore important to review the theory and literature relevant to both block copolymer self-assembly (Sect. 2.2) and, in particular, solvent vapour annealing (Sect. 2.3), a promising means of fabricating triblock terpolymer templates with the necessary long-range order. However, the triblock terpolymers used here are not amorphous but amorphous-semicrystalline, and it is additionally important to therefore understand any potential effects resulting from the crystallisation of the semicrystalline block during, or after, solvent vapour annealing (Sect. 2.4). Thereafter, the concept of a metamaterial (Sect. 2.5) and the existing theory and literature relevant to gyroid optical metamaterials (Sect. 2.6) are also reviewed.[1]

2.1 Gyroids

Before continuing, it is first prudent to define more carefully the various gyroid morphologies, elucidate their relationships to the gyroid surface and, indeed, one another, and present their most convenient mathematical representation.

[1]This chapter is based on portions of: Dolan, J. A., Wilts, B. D., Vignolini, S., Baumberg, J. J., Steiner, U., & Wilkinson, T. D. (2015). Optical properties of gyroid structured materials: From photonic crystals to metamaterials. *Advanced Optical Materials*, *3*, 12–32.

© Springer Nature Switzerland AG 2018

J. A. Dolan, *Gyroid Optical Metamaterials*, Springer Theses,
https://doi.org/10.1007/978-3-030-03011-7_2

2.1.1 Level Surfaces

Although a precise analytical expression for the gyroid surface exists, it is convenient for purposes of clarity and efficient modelling to approximate its form through a level surface [1, 2]. These are defined by functions of the form $F : R^3 \rightarrow R$ and are expressed as

$$F(x, y, z) = t, \tag{2.1}$$

where $F(x, y, z)$ determines the form of the surface via a space-dividing function and t is a constant which determines the volume fractions of the divided space.

2.1.2 Gyroid Surface

Substitution of the lowest allowed Miller indices for the structure with space group $I4_132$ into the appropriate form of function $F(x, y, z)$, and setting the parameter t to zero, results in the level surface approximation of the gyroid surface

$$\sin(\tilde{x})\cos(\tilde{y}) + \sin(\tilde{y})\cos(\tilde{z}) + \sin(\tilde{z})\cos(\tilde{x}) = 0, \tag{2.2}$$

where $\tilde{x}$, $\tilde{y}$, and $\tilde{z}$ are scaled spatial ordinates such that $\tilde{x} = 2\pi x/a$, $\tilde{y} = 2\pi y/a$, and $\tilde{z} = 2\pi z/a$ (Fig. 2.1). The variable a is the cubic unit cell edge length (referred to hereafter simply as the unit cell size). For a more detailed derivation see e.g. [1]. Although both the true gyroid surface and its level surface approximation are constant mean curvature surfaces, the former possesses zero mean curvature and the latter a small non-zero curvature. This approximate surface divides space into two sub-volumes of equal volume fraction and opposite handedness. The sub-volume on either side of the level surface has a morphology referred to as the "single gyroid".

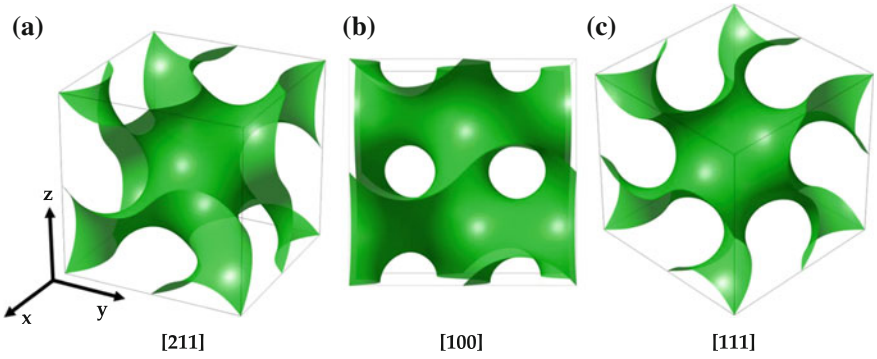

Fig. 2.1 The gyroid surface. Level surface approximation of the zero mean curvature gyroid surface (one unit cell) as defined by Eq. (2.2). The surfaces are viewed along the following crystallographic directions: **a** [211], **b** [100], and **c** [111]. The gyroid surface divides space into two sub-volumes of equal volume fraction and opposite handedness. Reprinted from [3] with permission from John Wiley and Sons

2.1.3 Single Gyroid

Setting the parameter t to $0 < |t| \leq 1.413$ results in a more general level surface approximation of the single gyroid

$$\sin(\tilde{x})\cos(\tilde{y}) + \sin(\tilde{y})\cos(\tilde{z}) + \sin(\tilde{z})\cos(\tilde{x}) = t. \tag{2.3}$$

This level surface exhibits increased absolute mean curvature and now divides space into two sub-volumes (single gyroids) of unequal volume fraction (Fig. 2.2a).[2] The coupled increase and decrease of the two sub-volumes, the increase in absolute mean curvature of the dividing surface, and the offset of the new level surface from the $t = 0$ surface are all monotonic with increasing $|t|$ [4]. At $|t| = 1.413$, one of the two sub-volumes is no longer continuous, referred to as "pinch-off" of the level surface. Discontinuity of one of the sub-volumes persists in the range $1.413 < |t| \leq 1.5$, the morphology then having a body-centred cubic symmetry. For values of $|t| > 1.5$, the single gyroid level surface is no longer mathematically defined.

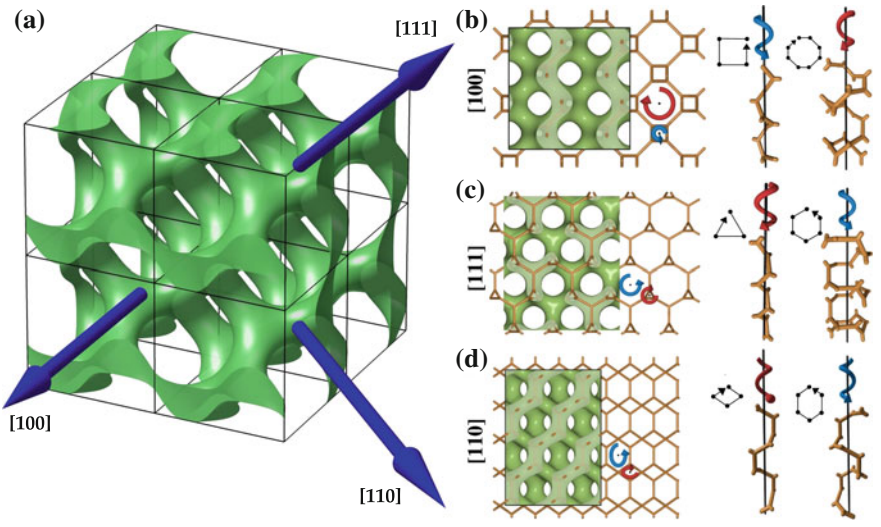

Fig. 2.2 The single gyroid morphology. **a** Level surface approximation of the single gyroid (eight unit cells arranged $2 \times 2 \times 2$) as defined by Eq. (2.3) with $t = 0.9$ (i.e. roughly 20% volume fill fraction). Projections along the crystallographic directions (high-symmetry directions) **b** [100] (H), **c** [111] (P), and **d** [110] (N) of the single gyroid level morphology and its srs-net (orange), highlighting the screw axes and their cross-sections. The high symmetry directions are useful for later interpretation of gyroid metamaterial band diagrams (Fig. 2.11). A left-handed local helical element is indicated by a blue arrow; a right-handed helical element by a red arrow. **a** reprinted from [3] with permission from John Wiley and Sons. **b–d** reprinted from [5] with permission from Elsevier

[2] As mentioned, the gyroid surface already divides space into two single gyroids of equal volume fraction. However, the distinction between the dividing surface (i.e. the gyroid surface) and the resulting three-dimensional morphology (i.e. the single gyroid) is useful.

The single gyroid is unique amongst similar morphologies based on cubic minimal surfaces in that it is inherently chiral (i.e. its mirror image cannot be transformed to coincide with itself by translation and rotation) [5, 6]. Indeed, by joining the centrelines of the gyroid to create a periodic graph (srs-net), one can readily identify local helices along the various screw axes of the gyroid [5]. For each of the [100], [111], and [110] directions, two screw axes can be identified and the associated helices exhibit opposing handedness and different average radii (Fig. 2.2b–d). For example, note that the [100] direction possesses local right-handed (left-handed) helical elements with a large (small) average radius, whereas the [110] direction possess local right- and left-handed helical elements with similar average radii. Although chirality is a symmetry property of the overall structure, it will be seen in Sect. 2.6 that the above considerations (i.e. the existence and handedness of local helical elements) impart a strong anisotropy to the chiro-optic properties of any gyroid-structured material.

2.1.4 Double Gyroid

Whereas the single gyroid level surfaces divide space into only two sub-volumes, a further simple alteration to the level surface equation allows the space to be divided into three continuous sub-volumes. By defining simultaneously both a positive and negative value of t, the level surfaces

$$\sin(\tilde{x})\cos(\tilde{y}) + \sin(\tilde{y})\cos(\tilde{z}) + \sin(\tilde{z})\cos(\tilde{x}) = \pm t \tag{2.4}$$

result in two interpenetrating single gyroid networks ($0 < |t| \leq 1.413$) of equal volume fraction but opposite handedness, together forming the so-called "double gyroid" with space group $Ia\bar{3}d$ (Fig. 2.3).[3] The double gyroid may be conceptualised as the sub-volumes either side of a $t = 0$ (gyroid) surface with finite thickness. Borrowing language from the block copolymer community, this thickened gyroid surface may then be referred to as the "matrix" which separates the two single gyroid networks. As $|t|$ increases so does the volume fraction of the matrix phase.

2.2 Block Copolymer Self-assembly

Self-assembly is the process by which a molecular system lowers its free energy by arranging itself into various energetically favourable configurations. The single and double gyroid morphologies may be found in a variety of natural and synthetic systems which undergo self-assembly. Block copolymers, a class of polymer consisting

[3]Note that the term "double gyroid" may also refer to the block copolymer microphase-separated morphology in which two chemically equivalent single gyroids are separated by a chemically distinct matrix (Sect. 2.2).

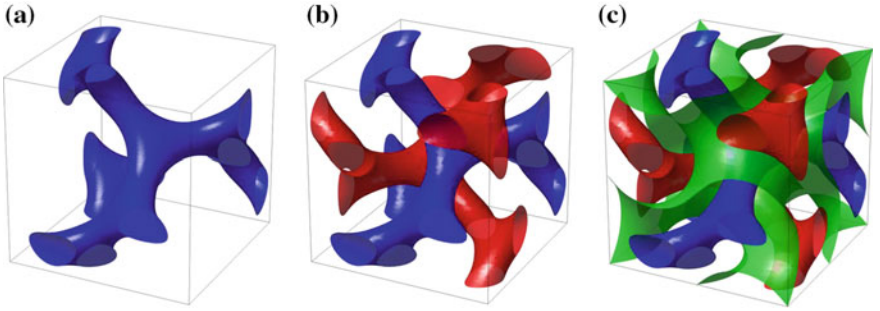

Fig. 2.3 The double gyroid morphology. The level surface approximation (one unit cell) is defined by Eq. (2.4) with $t = \pm 1.3$ (i.e. each single gyroid network is roughly 10% volume fill fraction). **a** The single gyroid morphology ($t = 1.3$) without either the matrix or the second interpenetrating single gyroid phase. **b** The double gyroid morphology ($t = \pm 1.3$) without the matrix. The two interprenetrating and enantiomorphic single gyroid networks are shown differently coloured but possess equal volume fill fractions. **c** The double gyroid morphology ($t = \pm 1.3$) and the gyroid surface ($t = 0$) which defines the centre of the matrix. Usually the matrix would entirely fill the void between the two single gyroid networks. Reprinted from [3] with permission from John Wiley and Sons

of two or more chemically distinct monomer types grouped together into "blocks", are one such system [7, 8]. The simplest block copolymer is the amorphous linear diblock copolymer, and its phase behaviour captures the essential elements of the behaviour of the more complex block copolymers used throughout this thesis.[4] Linear diblock copolymers have two monomer types (A and B; Fig. 2.4a) grouped together into a pair of covalently bonded homopolymers (i.e. AB; Fig. 2.4b, c). By comparison, linear triblock terpolymers have three monomer types (A, B, and C) arranged similarly (i.e. ABC; Fig. 2.4d). The chemical dissimilarity between blocks can lead to microphase-separation, a particular form of self-assembly. Although still used, the terms "microphase-separation" and "microdomain" are historic and in fact refer to phase separation and the resulting structures on the nanoscale, respectively. A particularly fascinating use of block copolymers is therefore to create one-, two- and three-dimensional inorganic materials structured on that length scale, including the subject of this thesis, optical metamaterials [9–11]. The basics of block copolymer self-assembly are therefore briefly reviewed, although this short introduction cannot hope to be comprehensive. Indeed, a number of excellent reviews on the topic already exist [12, 12–19].

[4] Amorphous block copolymers contain no semicrystalline etc. homopolymer block and is in contrast to amorphous-semicrystalline block copolymers introduced in Sect. 2.4.

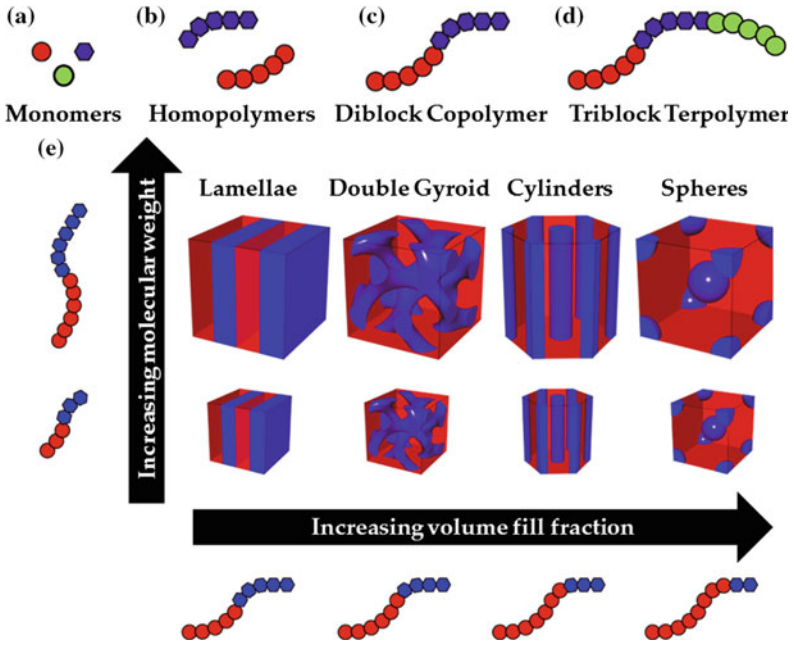

Fig. 2.4 Diblock copolymers and their self-assembled equilibrium morphologies. **a** Three chemically distinct monomers. **b** Homopolymers composed of two chemically distinct monomers. **c** Linear diblock copolymer in which the two homopolymers are covalently tethered. **d** Linear triblock terpolymer in which three homopolymers are covalently tethered. **e** Equilibrium morphology and characteristic periodicity for a microphase-separated diblock copolymer. Variation in volume fraction of the copolymer blocks determines the equilibrium morphology adopted by the copolymer; variation in the overall molecular weight determines the periodicity of the resulting morphology. Adapted from [20] with permission from Springer Nature

2.2.1 Diblock Copolymers

The bulk thermodynamic equilibrium morphology of an amorphous diblock copolymer depends on three parameters: N, the total degree of polymerisation; f_A or f_B, the volume fractions of homopolymer A or B, respectively ($f_A + f_B = 1$); and χ_{AB}, the Flory-Huggins interaction parameter specific to the chemical properties of the two homopolymers (a measure of the repulsion of the monomers). The interaction parameter χ_{AB} is the effective AB interaction energy, in units of $k_B T$, and is generally small and positive for incompatible monomers. For copolymers without

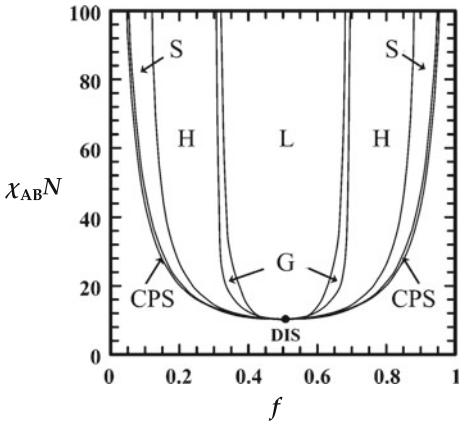

Fig. 2.5 Theoretical phase diagram for a linear diblock copolymer. The product $\chi_{AB}N$ determines the equilibrium microphase-separated morphology for a particular composition of copolymer, where χ_{AB} is the Flory-Huggins interaction parameter between the two blocks and is N the total degree of polymerisation of the copolymer. The parameter f is the fill fraction of one or other of the two blocks (i.e. f_A or f_B). The various equilibrium morphologies which minimise the thermodynamic free energy of the segregated system are: lamellae (L), the double gyroid (G), hexagonally-packed cylinders (H), body-centred cubic spheres (S), and close-packed spheres (CPS). Otherwise the system is disordered (DIS) (e.g. for $\chi_{AB}N \leq 10.5$ at $f = 0.5$). Reprinted (adapted) with permission from [21]. Copyright 2006 American Chemical Society

strong specific interactions (e.g. hydrogen bonds), χ_{AB} varies inversely with temperature. It is the product $\chi_{AB}N$, the overall "incompatibility" of the copolymer, which determines the existence and type of microphase-separated morphology at a particular composition and temperature. The schematic (Fig. 2.4e) and theoretical phase diagram (Fig. 2.5) for such a copolymer highlight the expected equilibrium morphologies (e.g. spheres, cylinders, the double gyroid, or lamellae). The equilibrium microphase-separated morphology minimises the overall free energy of the system by balancing the enthalpic (interfacial) and entropic (chain stretching) energy contributions. However, an intuition may be gained by considering only the necessity to minimise the interaction area between the two blocks (i.e. the enthalpic portion of the overall free energy). As long as the enthalpic interaction between the blocks (χ_{AB}) or the total molecular weight of the copolymer (N) are sufficiently large (i.e. the total enthalpic interaction between the blocks is sufficiently unfavourable), the copolymer will microphase-separate (e.g. for $\chi_{AB}N > 10.5$ for symmetric diblock copolymers; cf. Fig. 2.5). Note that the double gyroid phase, consisting of two interpenetrating single gyroid networks of one block separated by a matrix of the second, exists for a narrow value of block volume fractions between cylinders and lamellae.[5]

[5]Take care that the double gyroid morphology previously shown highlighted the two constituent single gyroid networks in different colours (Fig. 2.4). However, these gyroid networks are composed of the same block of the copolymer in the double gyroid phase.

Although a particular microphase-separated morphology may well be a thermodynamic minimum of the free energy of the bulk system, there are additional effects which may prevent the formation of this morphology. First are interfacial and commensurability effects which can dominate the behaviour of polymer thin films. For example, any difference in surface energy of the various blocks of the copolymer at either the substrate-polymer or polymer-air interfaces (which might also depend on the nature and concentration of any solvent present) may lead to the preferential wetting of one the blocks at the interfaces. Any morphology thus imposed by the interfaces will persist for a finite distance into the copolymer film which, if the film is particularly thin, may be a significant proportion of its thickness. Alternatively, should the total thickness of the copolymer film be incommensurate with the characteristic periodicity of the equilibrium morphology, then either the morphology or its orientation may alter to accommodate imposed boundary conditions. In thin films, the effect of surface energies of the blocks may therefore be substantial, and hence the microphase-separated morphology in a thin film may differ markedly from that of the bulk.

Kinetic effects may also prevent the self-assembly of a block copolymer, bulk or thin film, into its thermodynamic equilibrium morphology. For example, the copolymer may become trapped in a metastable state due to finite kinetic barriers (e.g. the hexagonally-perforated lamellae phase) or the self-assembly process may simply take place over a prohibitively long period of time [22, 23]. Indeed, whereas the periodicity of the block copolymer phase increases with increasing N, the rate of diffusion of polymer chains within the system, and therefore the time over which the equilibrium morphology is achieved, decreases with increasing N. Similarly, the kinetic penalties of reorienting variously oriented microdomains to create a minimum free energy structure with long-range order (i.e. fewer energetically unfavourable grain boundaries) may be prohibitively large given the low rate of diffusion of the polymer chains. Note that the thermodynamic equilibrium morphology nucleates randomly and in multiple locations from either a disordered copolymer melt or neighbouring ordered microphase-separated morphologies, thereby generally resulting in numerous variously oriented microdomains (though by no mean always).

2.2.2 Triblock Terpolymers

The phase behaviour of a diblock copolymer is completely described by the three aforementioned parameters: f_A, χ_{AB}, and N [25, 26]. However, to describe the phase behaviour of a triblock terpolymer for which the block order is known, twice as many parameters are required: f_A, f_B, χ_{AB}, χ_{BC}, χ_{AC}, and N [27]. The phase behaviour of triblock terpolymers is therefore significantly more rich and complicated than that of diblock copolymers. Despite this additional complexity, non-frustrated linear ABC triblock terpolymers are a class of triblock terpolymers which are particularly amenable to both experimental and theoretical study. A non-frustrated triblock terpolymer is one for which the block sequence and the thermodynamically preferred

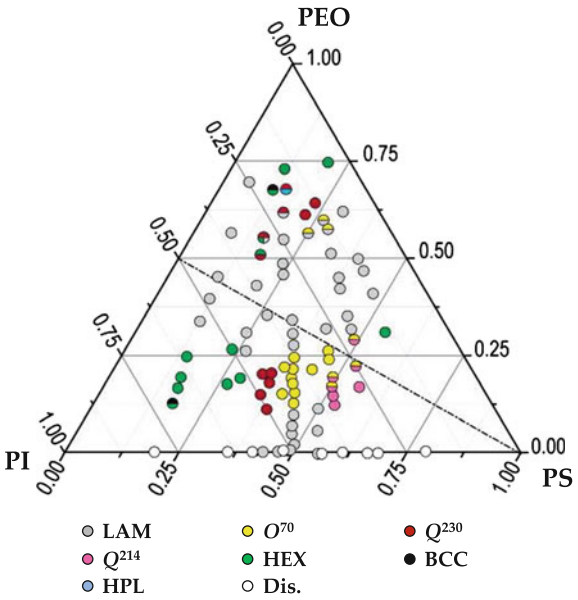

Fig. 2.6 Phase map of polyisoprene-*b*-polystyrene-*b*-poly(ethylene oxide) (ISO) triblock terpolymers. Six stable ordered phases are shown and coloured as follows: lamellae (LAM; grey); alternating gyroid (Q^{214}; pink); orthorhombic (O^{70}; yellow); hexagonal (HEX; green); core-shell double gyroid (Q^{230}; red); and body-centred cubic (BCC; black). A metastable phase, hexagonally-perforated lamellae (HPL; blue), and the disordered phase (Dis.; white) are also shown. Order-order transitions are shown with multicoloured symbols: top and bottom halves represent high and low temperature states, respectively. The dashed line is the $f_{\mathrm{PI}} = f_{\mathrm{PEO}}$ isopleth. The axes correspond to the volume fractions of the polyisoprene (PI), polystyrene (PS), and poly(ethylene oxide) (PEO) blocks of the terpolymer. The block volume fractions of the ISO terpolymers used in this thesis are $f_{\mathrm{PI}} \approx 0.30$, $f_{\mathrm{PS}} \approx 0.52$, and $f_{\mathrm{PEO}} \approx 0.17$, placing them in the alternating gyroid region of the phase map (Chap. 3). Reprinted (adapted) with permission from [24]. Copyright 2007 American Chemical Society

placement of the blocks are mutually reinforcing [24]. Such terpolymers are characterised by Flory-Huggins interactions parameters whereby $\chi_{\mathrm{AC}} \gg \chi_{\mathrm{AB}} \approx \chi_{\mathrm{BC}}$ [28]. These interaction parameters ensure that interfaces between the two end blocks are highly unfavourable (i.e. that only two interfaces are formed between each of the end blocks and the middle block) and that the resulting morphologies are likely either core-shell versions of diblock copolymer microphase-separated morphologies or "alternating" morphologies.[6] Tyler et al. in 2005 noted a number of systems which satisfy the conditions of a non-frustrated triblock terpolymer: polybutadiene-*b*-polystyrene-*b*-poly(vinyl pyridine) (PB-*b*-PS-*b*-PVP); poly(methyl methacrylate)-*b*-polystyrene-*b*-polybutadiene (PMMA-*b*-PS-*b*-PB); polyisoprene-*b*-polystyrene-*b*-poly(vinyl pyridine) (PI-*b*-PS-*b*-PVP); and, of most direct relevance to this thesis, polyisoprene-*b*-polystyrene-*b*-poly(ethylene oxide) (ISO) [28].

[6] A example of such a morphology, the core-shell double gyroid, may be seen in Fig. 2.7a.

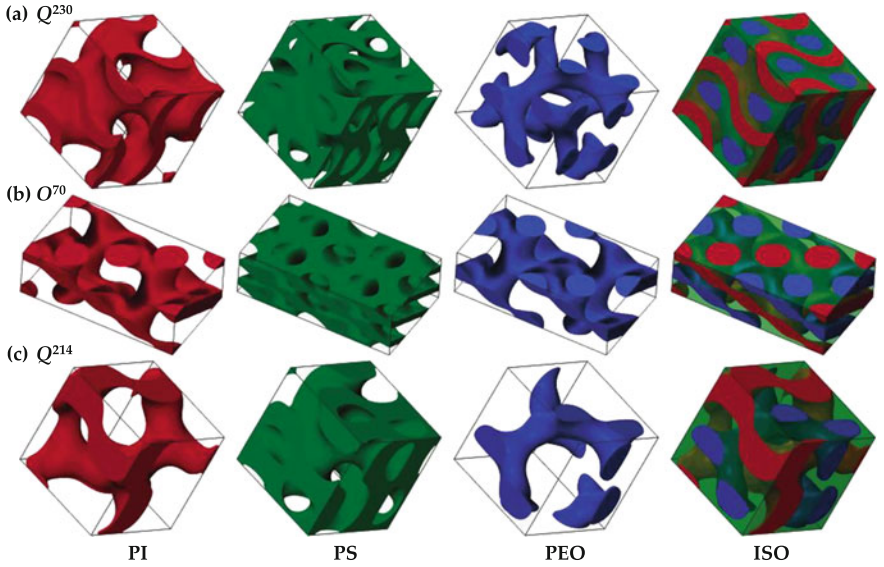

Fig. 2.7 Polyisoprene-*b*-polystyrene-*b*-poly(ethylene oxide) (ISO) triblock terpolymer network morphologies. Polyisoprene (PI; red), polystyrene (PS; green), and poly(ethylene oxide) (PEO; blue) phases are shown both individually and combined. **a** The core-shell double gyroid phase (Q^{230}). This may be considered as a PEO double gyroid surrounded by a core-shell matrix of PS and PI. **b** The orthorhombic phase (O^{70}). This phase is similar to the alternating gyroid but, unlike many other network phases, does not possess a cubic unit cell. **c** The alternating gyroid (Q^{214}). During gyroid optical metamaterial fabrication, the PI phase is removed to create a single gyroid template (Sect. 2.6). Reprinted (adapted) with permission from [29]. Copyright 2007 American Chemical Society

ISO triblock terpolymers have been studied extensively as a model non-frustrated ABC linear triblock terpolymer and, in particular, one likely to exhibit various multicontinuous network morphologies. By 2007, Chatterjee et al. were able to present the comprehensive phase map of ISO triblock terpolymers at weak to intermediate segregation strengths (Fig. 2.6) [24]. In doing so, they built upon prior work by Bailey et al. on the phase behaviour of ISO along the $f_{\mathrm{PI}} = f_{\mathrm{PS}}$ isopleth ($0 \leq f_{\mathrm{PEO}} \leq 0.33$), which first identified the existence of a non-cubic triply periodic network morphology in the region $0.12 \leq f_{\mathrm{PEO}} \leq 0.24$ [30]. Similarly, work by Epps et al. in the region $0.2 \leq f_{\mathrm{PI}} \leq 0.58$, $0.25 \leq f_{\mathrm{PS}} \leq 0.69$, and $0 \leq f_{\mathrm{PEO}} \leq 0.37$, which classified this new network morphology as the orthorhombic (O^{70}) phase, was also used [29, 31]. Epps et al. additionally identified the existence of the core-shell double gyroid (Q^{230}) and alternating gyroid (Q^{214}) morphologies either side of the orthorhombic phase (Fig. 2.7) [29, 31]. It is the alternating gyroid morphology, consisting of two interpenetrating polyisoprene (PI) and poly(ethylene oxide) (PEO) single gyroids separated by a polystyrene (PS) matrix, from which gyroid optical metamaterials have so far been fabricated (Sect. 2.6). The triblock terpolymer alternating gyroid phase differs from the diblock copolymer double gyroid phase as the

two single gyroid networks are chemically distinct and need not have the same volume fractions.[7] In total, six stable microphase-separated morphologies were identified: two- and three-domain lamellae; the "hexagonal phase" (assumed to be cylindrical); the "body-centred cubic (BCC) phase" (assumed to be spherical); and the three aforementioned network phases, the orthorhombic, the core-shell double gyroid, and the alternating gyroid [24]. These morphologies were confirmed as true equilibrium morphologies of both idealised (non-frustrated) ABC triblock copolymers and ISO by self-consistent field theory [28].

All of the ISO terpolymers studied above were synthesised such that their order-disorder transition (ODT) temperatures lay in the experimentally accessible window 0–90 °C (i.e. molecular weights $\approx$ 15–25 kg mol^{-1}) [24, 29–31]. Experiments on higher molecular weight ISO terpolymers, such as those used in this thesis, determined that whereas the slowed kinetics might inhibit the establishment of the equilibrium microphase-separated morphologies of Fig. 2.7, they do not necessarily preclude their existence [32]. Of course, in all cases the microphase-separated morphologies were explored as a function of temperature rather than, say, solvent concentration (i.e. the ISO terpolymers were not solvent-annealed).

2.3 Solvent Vapour Annealing

Block copolymers are most readily equilibrated (i.e. encouraged to relax into their thermodynamic equilibrium morphology) by heating [7, 8]. Many block copolymers used to template inorganic materials possess a glassy block, for mechanical stability during subsequent processing steps. It is therefore necessary to thermally anneal the copolymer to above the highest glass transition temperature T_g of any glassy block present, to allow reorganisation and self-assembly to take place.[8] However, in the temperature window above the highest T_g but below the thermal degradation temperature of the film, the mobility of high molecular weight copolymer chains is relatively low. Indeed, the kinetics of reorganisation of the copolymer microdomains during annealing slow with increasing viscosity of the melt and molecular weight of the copolymer. It is therefore advantageous to lower the T_g of the copolymer to below ambient temperature such that it may anneal without the application of heat. This may be achieved by the introduction of controlled amounts of solvent into the copolymer in a process termed solvent vapour annealing (SVA).[9] In addition to avoiding potential degradation of the film, the mobility of the copolymer chains is greatly increased in the presence of a solvent, reducing the time scale over which the

[7] It is only the alternating gyroid phase, through selective etching of a single block, which allows ready access to the single gyroid morphology.

[8] Thermal annealing will be used to create the multi-domain gyroid optical metamaterials characterised in Chap. 6.

[9] Solvent vapour annealing will be used to create the single-domain gyroid optical metamaterials characterised in Chap. 7.

copolymer relaxes into its thermodynamic equilibrium morphology and increasing the resulting domain size substantially [33–35]. However, the solvent often reduces the value of any interaction parameters (e.g. χ_{AB}).

2.3.1 Diblock Copolymers

The effect of SVA on linear diblock copolymers has been studied extensively [36, 37]. A neutral solvent will swell both blocks of the copolymer equally, leaving the effective volume fractions f_A and f_B unaltered, but screening the interaction between the two blocks (i.e. lowering χ_{AB}). A sufficiently high solvent concentration will lower χ_{AB} to such an extent that the microphase-separated morphology is no longer thermodynamically favourable and the copolymer disorders. A selective solvent will preferentially swell only one of the blocks, altering the effective volume fractions and, therefore, the equilibrium morphology of the copolymer [38, 39]. It is thus possible to explore the entire phase space of diblock copolymers (i.e. spheres, cylinders, the double gyroid, and lamellae) with only a single copolymer, by varying the solvent concentration and selectivity [39].

2.3.2 Triblock Copolymers and Terpolymers

In contrast, the effect of SVA on linear triblock copolymers (ABA) and terpolymers (ABC), the subject of this thesis, has received substantially less attention. Early studies on polystryene-*b*-polybutadiene-*b*-polystyrene (PS-*b*-PB-*b*-PS) triblock copolymers focused on the morphological transitions resulting from the exposure to selective and neutral solvents [40], the improvement in symmetry and long-range order of the cylindrical and lamellar microphase-separated morphologies [40], and the effect of solvent evaporation rate on the orientation of cylindrical microdomains [41]. More recent studies focused further on the effect of solvent removal rate upon the orientation of cylindrical microdomains in poly(deuterated styrene)-*b*-polyisoprene-*b*-poly(deuterated styrene) (PdS-*b*-PI-*b*-PdS) [42] and polystyrene-*b*-polyisoprene-*b*-polystyrene (PS-*b*-PI-*b*-PS) [43]. Most recently, a poly(2-vinyl pyridine)-*b*-polystryene-*b*-poly(2-vinyl pyridine) (P2VP-*b*-PS-*b*-P2VP) triblock copolymer treated by SVA has been demonstrated to achieve the desired perpendicular orientation and long-range order of lamellae for the fabrication of sub-10 nm lithographic templates [44].

Similarly, early studies on polystyrene-*b*-poly(2-vinyl pyridine)-*b*-poly(*tert*-butyl methacrylate) (PS-*b*-P2VP-*b*-PtBMA) triblock terpolymers investigated the effect of solvent [45], solvent removal rate [45, 46], and annealing time [47] upon the microphase-separated morphology and microdomain orientation. The morphological transitions observed during SVA of polystyrene-*b*-polybutadiene-*b*-poly(2-vinyl pyridine) (PS-*b*-PB-*b*-P2VP) [48], which included the sequence of core-

shell cylinders, spheres in "diblock gyroid", spheres in lamellae, and spheres, in both neat terpolymer [49] and homopolymer blends [50], were also investigated in detail. Although most of the above studies have concentrated on triblock terpolymers which form hexagonal and lamellar microphase-separated morphologies, SVA and controlled solvent evaporation may also be used to control the orientation of double-helical microdomains in films of polystyrene-*b*-polybutadiene-*b*-poly(methyl methacrylate) (PS-*b*-PB-*b*-PMMA) [51]. Finally, the gyroid phase could be accessed during solvent annealing of a poly(ethylene oxdide)-*b*-poly(ethyl acrylate)-*b*-polystyrene (PEO-*b*-PEA-*b*-PS) triblock terpolymer blended with phenolic resin oligomers (resol) to create bicontinuous mesoporous carbon films [52]. However, it was only through an order-order transition (OOT) from the cylinder to the gyroid phase during thermopolymerisation of the resol that the gyroid morphology could be accessed in the carbonised films.

2.3.3 Gyroid-Forming Block Copolymers

Apart from the study above, where the gyroid morphology was ultimately accessed through the cylinder phase, there are only a handful of efforts to apply SVA directly to gyroid-forming block copolymers. It is precisely this, the application of SVA to a gyroid-forming triblock terpolymer, which is of concern here. She et al. demonstrated controlled ordering of the double gyroid morphology in polystyrene-*b*-poly(L-lactide) (PS-*b*-PLLA) diblock copolymers (block molecular weights 34 and 27 kg mol^{-1}, respectively; $f_{\mathrm{PLLA}} = 0.39$) upon annealing in a neutral solvent (1,2-dichloroethane) and employing a functionalised silicon dioxide substrate [53]. The resulting double gyroid microphase-separated morphology presented the (211) plane parallel to the substrate. If annealed in a partly selective solvent for the PS (chloroform), a morphological transition from the gyroid to cylinder morphology, via a reorientation of the gyroid morphology to present the (110) plane parallel to the substrate, was identified. The transition was determined to be driven by preferential segregation of the PS block to the surface of the film. Of course, for the transition to be observed, the film had to remain microphase-separated throughout the annealing protocol. Continuing to work with PS-*b*-PLLA, Wu et al. explored the effect of swollen thickness and solvent removal rate on the resulting morphology of the solvent-annealed diblock copolymer [54]. However, on this occasion, the authors made sure to swell the films to such an extent that the copolymer was no longer microphase-separated before removal of the solvent. The authors identified three regimes of morphological evolution as a function of swollen film thickness: the "anisotropic structure" regime (in which cylinders are formed with varying orientations depending on the solvent removal rate); the "phase transition" regime (in which the cylinder and gyroid morphologies coexist and the plane of the gyroid parallel to the surface is closely related to the orientation of the cylindrical microdomains in the first region); and the "isotropic structure" regime (in which various planes of

the gyroid may be parallel to the surface but the driving force is thermodynamic and therefore independent of solvent removal rate). None of these few studies were performed in situ (e.g. using X-ray scattering techniques) or on a triblock terpolymer. Such a study is presented in Chap. 4.

2.4 Block Copolymer Crystallisation

Whereas the above primarily concerns the behaviour of purely amorphous block copolymers, the ISO triblock terpolymers used in this thesis are not amorphous but, rather, amorphous-semicrystalline.[10] This class of block copolymers (i.e. those possessing both amorphous and semicrystalline homopolymer blocks) introduces additional complexity due to the delicate interplay between the driving forces of crystallisation and microphase-separation [55]. Indeed, a rich variety of behaviour is observed in even simple linear diblock amorphous-semicrystalline copolymers, for which the taxonomy of crystallisation is based on three key parameters: the order-disorder transition temperature of the copolymer T_{ODT}; the glass transition temperature of the amorphous block T_g; and the crystallisation temperature of the semicrystalline block T_c [56]. Respectively, these parameters characterise the relative strength of the driving forces of microphase-separation, vitrification, and crystallisation.

If the crystallisation temperature is lower than the order-disorder transition temperature ($T_c < T_{ODT}$), then the copolymer will crystallise from an ordered microphase-separated melt. Crystallisation from a disordered melt ($T_c > T_{ODT}$) will almost inevitably result in a crystalline lamellar structure (i.e. a structure consisting of alternating semicrystalline and amorphous lamellae). Instead, crystallisation from an ordered melt will depend sensitively on the volume fraction of the semicrystalline block, the state of the amorphous block (e.g. rubbery or glassy), the segregation strength of the copolymer, and the kinetics of crystallisation. If the crystallisation temperature is well below the glass transition temperature of the amorphous block ($T_c \ll T_g$), then the semicrystalline block undergoes confined crystallisation.[11] As the crystallisation temperature approaches the glass transition temperature of the amorphous block, the semicrystalline block may first begin to distort ($T_c \approx T_g$) and finally "break out" ($T_c \gg T_g$) of the increasingly rubbery amorphous block [57]. However, if the segregation strength (i.e. $\chi_{AB}N$) of a rubbery-semicrystalline copolymer at the crystallisation temperature is sufficiently high relative to the segregation strength at the order-disorder transition temperature, the semicrystalline block may again undergo confined crystallisation, depending also on the kinetics of crystallisation

[10] Poly(ethylene oxide) (PEO) is a semicrystalline polymer; polyisoprene (PI) and polystyrene (PS) are both amorphous. At room temperature, PS is glassy and PI is rubbery [31].

[11] In our ISO triblock copolymers, the glassy PS is the majority phase ($f_{PS} \approx 52\%$) and the one surrounding the semicrystalline PEO.

[58, 59]. Should the segregation strength of the rubbery-semicrystalline copolymer be weak, then breakout crystallisation and a destruction of the initial melt morphology is almost inevitable.

2.4.1 Spherulites

When breakout crystallisation occurs, the resulting crystalline superstructure is usually spherulitic, indicating radial crystallisation of the semicrystalline block of the copolymer [8]. The optical birefringence of semicrystalline polymers and the spherically symmetrical growth pattern together result in the classic "Maltese cross" birefringent texture under crossed polarisers. The formation of spherulites often accompanies the large scale rearrangement of the copolymer into alternating lamellae of the amorphous and semicrystalline blocks, and the associated destruction of any previous microphase-separated morphology.[12] Within the semicrystalline lamellae, the stretched polymer chains are oriented perpendicular to the radial crystallisation growth direction (i.e. tangentially). The ability with which a particular copolymer forms spherulites is a function of the semicrystalline block fraction, segregation strength, and sample thickness (e.g. bulk or thin film) [60, 61]. Although spherulites are most often associated with breakout crystallisation, it is not the case that a spherulitic superstructure necessarily implies breakout crystallisation [62–65]. Indeed, spherulites have been observed to coexist with lamellae [59, 65–69] and other [61, 71] microphase-separated morphologies in both rubbery- and glassy-semicrystalline block copolymers. Crucially, the crystalline morphology and resulting superstructure of any copolymer are often a sensitive function of crystallisation conditions, especially in the case of confined crystallisation [60, 68, 71].

2.4.2 Crystallisation Temperature

One such condition, which has a profound effect upon the crystallisation behaviour of the semicrystalline block, is the crystallisation temperature. In the case of polystyrene-*b*-poly(ethylene oxide) (PS-*b*-PEO) diblock copolymers, there is a clear relationship between the crystallisation temperature and the orientation of the PEO crystallites relative to the interface with the amorphous block, which is near identical irrespective of whether the PEO is confined to lamellae [72], cylinders [73, 74], hexagonally-perforated lamellae [75, 76], or inverse cylinders [77]. As the crystallisation temperature is increased (i.e. the degree of supercooling is reduced), the PEO crystallite *c*-axis (the long axis of the polymer chains) transitions from a random orientation to parallel, tilted, and then perpendicular with respect to interface between

[12] Semicrystalline homopolymers readily form spherulites, whereby the amorphous and semicrystalline lamellae are both formed from the same polymer.

the PEO block and the surrounding glassy PS block. Additionally, for confinement within hexagonally-perforated lamellae and inverse cylinders at high crystallisation temperatures (i.e. low degrees of supercooling), the PEO crystallites are oriented in two dimensions and are aligned to grow along the $\{10\bar{1}0\}$ planes of the hexagonally arranged PS perforations and cylinders. A further condition, which may alter the delicate balance between the driving forces of crystallisation and microphase-separation, and therefore also the resulting crystalline morphology, is the presence and selectivity of solvents [66, 71, 78–80]. It is likely that some effects of a solvent (e.g. the reorientation of crystalline lamellae upon solvent evaporation) are qualitatively similar to those of crystallisation temperature and may therefore be understood by a judicious comparison [81]. However, the presence of a solvent will also have a substantial effect upon both the thermodynamics and kinetics of self-assembly of any block copolymer through the alteration of the relevant segregation strengths, changes in volume fractions due to selective swelling, and the rate of diffusion of the copolymer chains. The introduction of solvent into a amorphous-semicrystalline block copolymer is therefore anticipated to greatly increase the already substantial complexity of the observed behaviour.

2.4.3 Gyroid-Forming Block Copolymers

Notable by its absence from the above studies on crystallite alignment in diblock copolymer equilibrium morphologies is the double gyroid morphology, in which one block of the copolymer forms two interpenetrating single gyroid networks separated by a continuous matrix of the second block. Although confined crystallisation has been observed for gyroid-forming amorphous-semicrystalline block copolymers, no preferential orientation or alignment of the confined crystallites has been reported [82–84]. Instead, a templating effect is observed when breakout crystallisation occurs from an aligned double gyroid melt. Preferential orientation of the resulting crystalline lamellar morphology has been found to be templated by both the {211} and {220} planes of the double gyroid in rubbery-semicrystalline diblock copolymers [63, 85]. Notwithstanding the potential effect of the curved interfaces, confined crystallisation within a gyroid network can result in a reduced crystallinity and slowed crystallisation kinetics in a manner entirely analogous to confined crystallisation within other microphase-separated morphologies of varying dimensionality, connectivity, and cooperativity [69, 86]. As a continuous three-dimensional morphology with high cooperativity between adjacent grains, the gyroid can allow crystallisation on a macroscopic length scale from a number of heterogenous nuclei far fewer than the number of microdomains [82–84]. A study of confined crystallisation within a single gyroid network is presented in Chap. 5.

2.5 Metamaterials

In this thesis, block copolymer self-assembly and solvent vapour annealing, both introduced above, are used to fabricate optical metamaterials. Metamaterials are artificially engineered materials which, by virtue of their structure and not only their chemical composition, may exhibit various electromagnetic properties not otherwise encountered in nature [87]. Unlike photonic crystals, the structural units of metamaterials, termed "meta-atoms" or "meta-molecules", are deeply sub-wavelength. The response of the material may therefore be described in terms of bulk (homogeneous) effective parameters, i.e. the permittivity $\varepsilon_{\text{eff}}(\omega)$, the permeability $\mu_{\text{eff}}(\omega)$, and the electromagnetic coupling parameter $\gamma_{\text{eff}}(\omega)$. These effective parameters may be anisotropic and will almost certainly be temporally (and perhaps also spatially) dispersive.[13] It is the nature and morphology of these structural units which impart to a metamaterial its unique electromagnetic properties.

One such property not generally found in nature, but which has generated intense interest, is negative refraction. Veselago in 1968 first theoretically demonstrated that a material with simultaneously negative (real) values of permittivity and permeability (a "doubly negative" medium) would exhibit negative refraction [89, 90]. However, without access to any natural doubly negative materials, it was over thirty years until the phenomenon was first experimentally demonstrated, by Smith et al. in 2000, using split-ring resonator metamaterials [91]. That same year, Pendry made the first of a number of predictions regarding the potential applications of negatively refracting materials, namely that they could be used to create a cloaking device or "super lens" capable of resolving sub-wavelength features [92, 93]. Thus the history of metamaterials since the turn of the century has been near synonymous with the pursuit of negatively refracting materials.

An alternative route to negative refraction, other than the fabrication of a doubly negative medium, is to create a material with a strong chiral response [94]. If the chiro-optic effect is sufficient, such a material will exhibit negative refraction for one handedness of circularly polarised light [95, 96]. It is for this reason, amongst others, that chiral metamaterials, including single gyroid optical metamaterials, have also received intense interest [97, 98].[14]

Negative refraction is, however, only one electromagnetic property of potential interest. Of perhaps more immediate technological relevance is access to particularly large and small, or strongly anisotropic (e.g. hyperbolic), material parameters and their associated science and engineering [99]. Indeed, the great attraction of metamaterials is that one may theoretically design any arbitrary electromagnetic response as desired. Metamaterials therefore offer huge flexibility to exploit exotic situations, combinations, or spatial arrangements of effective material parameters in electromagnetic material design, thereby greatly expanding the range of electromagnetic responses otherwise found in natural and synthetic bulk materials.

[13] Spatial dispersion is where the material response is dependent on wave vector $\mathbf{k}$ (i.e. the medium is non-local). A temporally and spatially dispersive permittivity would be denoted $\varepsilon(\omega, \mathbf{k})$ [88].

[14] Recall that the single gyroid is chiral; the double gyroid is achiral (Sect. 2.1).

Some materials which would today be classified as metamaterials have in fact been studied for many decades [87]. Those early metamaterials (e.g. artificial dielectrics) were designed to operate in the microwave regime and were therefore macroscopic in their unit cell structure and periodicity [100]. In contrast, an optical metamaterial requires structural units tens of nanometres across in order to satisfy the condition of sub-wavelength feature sizes. Achievements in the field of optical metamaterials have therefore gone hand in hand with advances in nanofabrication technologies, without which the ability to pattern materials on the required length scale would be near impossible [101]. However, many early top-down lithographic techniques were either intrinsically two-dimensional (e.g. a single material layer) or ventured into the third dimension only by tedious and non-scalable stacking of individual layers. These techniques are arguably still incapable of fabricating three-dimensional nanostructures over macroscopically large areas with sufficient speed and cost-effectiveness to allow optical metamaterials to attain true technological relevance. Therefore, until recently, three-dimensional optical metamaterials presented a considerable challenge [102].

2.6 Gyroid Optical Metamaterials

Block copolymer self-assembly presents an alternative means by which to fabricate intricate one-, two-, and three-dimensional morphologies on nanometre length scales, which may act as templates for optical metamaterial fabrication [103]. In linear triblock terpolymers, one such morphology is the alternating gyroid: two single gyroid networks, each composed of one block, separated by a matrix of the third. As the two single gyroid networks in the alternating gyroid are chemically distinct, it is possible to selectively remove just one such network and use the remaining voided terpolymer as a sacrificial template for metal deposition [11, 54]. The resulting structure is fully three-dimensional and intrinsically chiral, thus possibly also negatively refracting. Such three-dimensional (chiral) optical metamaterials simply cannot otherwise be fabricated over large areas with comparable rapidity using existing top-down fabrication techniques [101]. Gyroid optical metamaterials are therefore a rich source of interesting physics inaccessible by other means.

2.6.1 Fabrication

Gyroid optical metamaterials were first fabricated and demonstrated by Vignolini et al. in 2012 [104]. Working with a $53\,\mathrm{kg\,mol^{-1}}$ polyisoprene-*b*-polystyrene-*b*-poly(ethylene oxide) (ISO) triblock terpolymer, the authors used a crude solvent

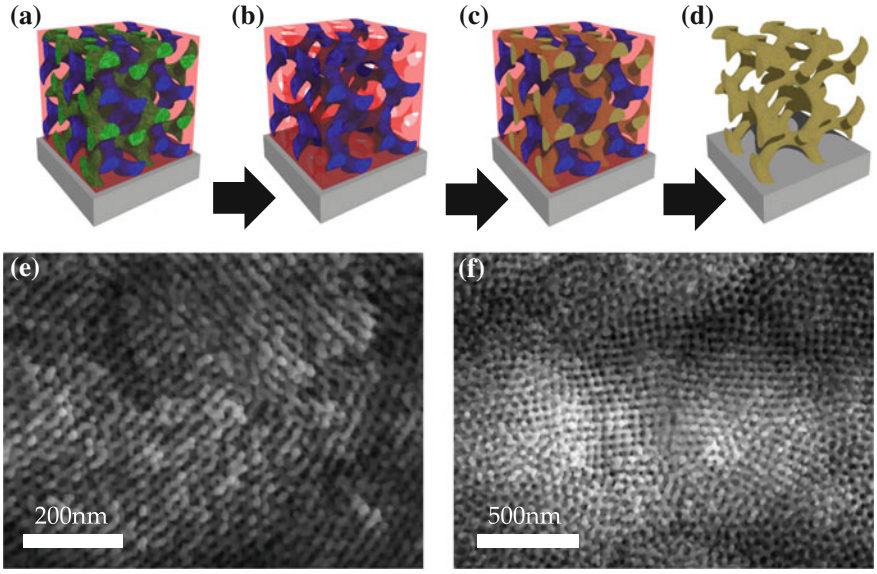

Fig. 2.8 Fabrication of gyroid optical metamaterials from a triblock terpolymer. **a** Alternating gyroid equilibrium morphology formed from a triblock terpolymer (red, blue, and green). **b** Selective etching of a single gyroid network (i.e. one terpolymer block; green) resulting in a single gyroid template. **c** Back-filling of the gyroid template with metal (e.g. gold) by electrodeposition. **d** Removal of the remaining terpolymer (red and blue) resulting in a single gyroid optical metamaterial. Scanning electron micrographs of **e** 35 and **f** 50 nm unit cell gold gyroids with fill fractions of around 30% fabricated from a 35 kg mol^{-1} and 80 kg mol^{-1} ISO triblock terpolymer, respectively. These samples were thermally annealed and therefore exhibit only relatively short-range order

vapour annealing technique to achieve domains between 10–100 μm in size.[15] The polyisoprene (PI) phase was selectively removed from the self-assembled gyroid structure by ozonolysis to leave behind a single gyroid template. This template was then back-filled with gold by electrodeposition to create, upon removal of the remaining organic material, a gold single gyroid thin film of roughly 200 nm in thickness (Fig. 2.8). The gold gyroid structure possessed a unit cell size of ≈50 nm and a fill fraction of 30% [104, 105]. Note that gold was chosen because of its plasmonic properties and chemical stability.

2.6.2 Optical Properties

Reflectance and transmittance spectra of the gold gyroid thin film fabricated by Vignolini et al. were obtained using unpolarised light, highlighting the characteristic

[15]Note that, hereafter, "domain" may refer both to regions of the optical metamaterial and the triblock terpolymer template from which they are fabricated.

gyroid extinction peak at around 600 nm, associated with the striking red colour of the sample [104]. Investigation of individual domains with linearly and circularly polarised light allowed identification of both linear and circular dichroism, respectively. The linear dichroism manifested as a shift in the extinction peak as a function of relative orientation between the direction of polarisation and the single gyroid morphology. The extinction peak was maximally blue- and red-shifted when the direction of polarisation was parallel and perpendicular, respectively, to the [100] direction of the gyroid (Fig. 2.9a, b; cf. Fig. 2.2).[16] Like all single domain gyroid samples considered here, the sample investigated by Vignolini et al. exhibited the [110] orientation out-of-plane (cf. Chaps. 5 and 7). Circular dichroism was not observed along the [110] direction but instead occurred when the incident light coincided with the [111] chiral axis of the gyroid structure, which could only be accessed by tilting the sample by 35° and rotating it about its normal (Fig. 2.9c).

Salvatore et al. further investigated the potential to tune the optical properties of gold gyroid optical metamaterials by three distinct mechanisms: varying the unit cell size, the volume fill fraction, and the refractive index of the surrounding media [106]. Using two ISO triblock terpolymers with different molecular weights but identical block volume fractions, the authors first demonstrated the shift in extinction peak caused by variation in unit cell size. The two terpolymers formed gyroids with 35 and 50 nm unit cell sizes and exhibited extinction peaks at 550 and 620 nm, respectively (i.e. the extinction peak was red-shifted with increasing unit cell size). The volume fill fraction of either gyroid could be increased by electrodepositing additional gold onto the gyroid optical metamaterial, from 30% up to 90%. As the fill fraction increased, the extinction peak and the "plasma edge" both blue-shifted due to the modification of the mobility of electrons in the larger struts.[17] Also noticeable with the increase in fill fraction was the reduction in linear dichroism of the structure. The linear dichroism, measured as the shift in plasma edge for incident light polarised perpendicular and parallel to the [100] direction of the gyroid, reduced from its maximum at a fill fraction of 30% to zero for fill fractions $\gtrsim$50%. Finally, the extinction peak was further varied by infiltration of the structure with media of various refractive indices, thereby changing the dielectric contrast between the gold and its surrounding. As the refractive index of the surrounding medium was successively increased from that of air to that of an oil with refractive index $n = 1.7$, the extinction peak and plasma edge red-shifted by around 200 nm. The effects of these three parameters on the response of the gyroid optical metamaterials are summarised in Table 2.1.

[16] The physical mechanism underlying this linear dichroism is revealed in Chap. 7.

[17] The plasma edge is a useful metric for characterisation of gyroid optical metamaterials (and indeed other highly interconnected metallic structures) and is the wavelength at the point of inflection of the reflectance spectrum.

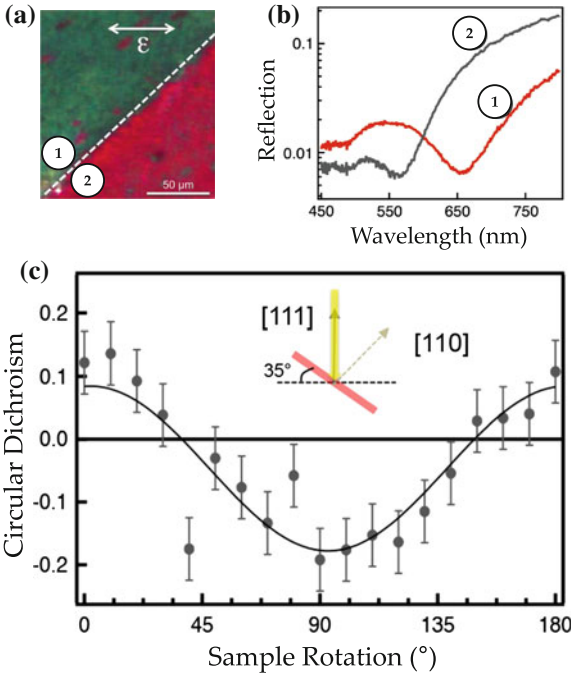

Fig. 2.9 Linear and circular dichroism of gold gyroid optical metamaterials. **a** Optical micrograph of a 50 nm unit cell and 30% fill fraction gold gyroid metamaterial under linearly polarised light (as indicated by the white arrow); regions labelled "1" and "2" are two domains for which the orientation of the gyroid is roughly parallel to and perpendicular to the [100] axis, respectively. **b** Reflection spectra of the two domains visible in the optical micrograph. **c** Difference between the transmission (averaged over the wavelengths 600–750 nm) for right- and left-handed circularly polarised light for the same gyroid when rotated around the [110] axis at an angle of 35° to the plane of the substrate. The solid line is a guide for the eye. Reprinted (adapted) from [104] with permission from John Wiley and Sons

Table 2.1 Effect of increase in various structural parameters on the effective plasma wavelength λ_p and linear and circular dichroism of gyroid metamaterials. "↑" indicates a proportional relationship, "↓" an inverse relationship, and "–" that the relationship is as yet unexplored

	λ_p	Linear and circular dichroism
Unit cell size (a)	↑	↓
Fill fraction (f)	↓	↓
Host refractive Index (n_{fill})	↑	–

2.6.3 Simulations and Theoretical Description

Whereas all of the above experiments were performed on single gyroids, the research to first highlight (theoretically) the potential for metallic gyroids to act as metama-

terials, by Hur et al. in 2011, investigated also double and "hollow" double gyroids [103]. The authors notably predicted negative refraction for low-loss (e.g. silver or aluminium) double gyroids in the visible and near-infrared. According to simulations, lossless gold double gyroids with a 100 nm unit cell size and a 34% fill fraction did not exhibit a metallic band gap but instead showed low frequency bands, not otherwise expected considering the high volume fraction of metal. Closer investigation of these low frequency propagation bands revealed that some exhibited all-angle negative refraction. The introduction of damping losses had little effect on these negative refraction bands. However, utilisation of an experimentally derived dielectric constant for gold highlighted the prevention of negative refraction by the strong absorption resulting from interband transitions [103]. It was hypothesised that the two enantiomorphic single gyroid networks which comprise the double gyroid form a capacitor structure via the coupled surface plasmon resonances of the two individual networks. This capacitor may act as a metal-insulator-metal waveguide, which supports surface plasmon polariton propagation, and the resulting waveguide bands were found to be responsible for the negative refraction. Note that according to this hypothesis, the negative refraction predicted in double gyroids is clearly not a product of the chirality of the structure, which is overall achiral. Though given less attention, single gyroids (termed alternating gyroids after the associated triblock terpolymer microphase-separated morphology) were also investigated. Lacking a "counter electrode", the low frequency propagation of light from coupled surface plasmon resonances was forbidden and single gyroids therefore demonstrated a metallic band gap (i.e. a plasma frequency) at low frequencies.

Taking a somewhat different approach, the optical response of the gold gyroid optical metamaterials fabricated by Vignolini et al. and described above were first explained intuitively with respect to the classic sparse cubic wire array investigated by Pendry et al. in 1996 [107]. This prototypical metamaterial exhibited a greatly reduced plasma frequency from that of the constituent metal. As part of their study, Vignolini et al. noted that an amorphous composite of gold and air with the same volume fill fraction should exhibit near-perfect reflection in the red and infrared, contrary to the experimental results [104].[18] It was therefore hypothesised that the gyroid optical metamaterial acted as a dilute metal, similar to Pendry's cubic wire array, with an effective plasma frequency substantially reduced from that of gold. According to the model, such a decrease in plasma frequency comes about from both a reduction in average electron density due to the porosity of the structure, and the increased self-inductance of the highly interconnected and ordered network of metal. It was with respect to this simple model that many of the initial experimental results were interpreted.

Although the intuitive model introduced above describes well some aspects of the gyroid metamaterial electromagnetic response, it fails to model its anisotropic optical properties. Developed by Demetriadou et al. in 2013 and further elucidated by Oh et al. the same year, the tri-helical metamaterial (THM) model was proposed as an ana-

[18] This assertion is tested in Chap. 6, in which an effective medium model for multi-domain gyroid optical metamaterials is found.

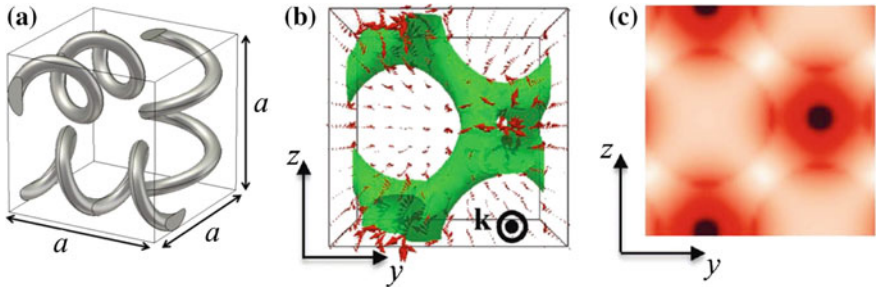

Fig. 2.10 The tri-helical metamaterial (THM) model of gyroid optical metamaterials. a THM approximation of the gyroid, consisting of unconnected helices oriented along the three cubic axes, where a is the unit cell size. Reprinted (adapted) from [108] with permission from the Institute of Physics and Deutsche Physikalische Gesellschaft. **b** Magnetic field distribution within a perfect electrical conductor (PEC) gyroid demonstrating the dominance of the small helices. Magnetic field vectors (arrows) at a point in time during propagation of the longitudinal mode travelling in the x direction (into the page). **c** The line integral along the x direction of the square of the magnetic field strength; dark and light represent areas of maxima and minima of the field strength, respectively. Reprinted (adapted) from [109] with permission from John Wiley and Sons

lytical model to investigate the (chiral) electromagnetic response of gyroid metamaterials and their underlying physics [106, 108, 109]. The THM model approximates the single gyroid structure as a network of unconnected helices oriented along the three cubic axes (Fig. 2.10a). The model allows the identification of two transverse and one longitudinal propagating mode and their dispersion relations, which were found to agree well with finite-difference time-domain (FDTD) band calculations of a perfect electrical conductor (PEC) THM.[19] As expected, due to the chirality of the structure, the two transverse modes were non-degenerate, leading to negative refraction for one handedness of circularly polarised light. However, a FDTD band calculation of a PEC gyroid along the [100] and [111] directions highlighted no such degeneracy of the transverse modes for k values away from the Brillouin zone boundaries, implying that the gyroid possesses significantly weaker chiro-optic properties than the THM. Further investigation of the magnetic fields associated with the propagating longitudinal and transverse modes in the gyroid determined that the induced currents are highly localised along the smaller helices present in the structure (Fig. 2.10b, c). These smaller helices therefore dominate and alone determine the electromagnetic response of the metamaterial. It is this dominance, the interconnectivity of the structure, and the mixture of right- and left-handed helices present along any orientation of the gyroid which appear to be responsible for the significant weakening of any chiro-optic effect and the associated absence of negative refraction [108, 109].

Although it incorrectly predicts negative refraction, the THM model may still be applied to the PEC gyroid, using the geometrical parameters of the small helices,

[19] Although not considered in detail here, the existence of a longitudinal mode implies that spatial dispersion may well be non-negligible in gyroid optical metamaterials [88].

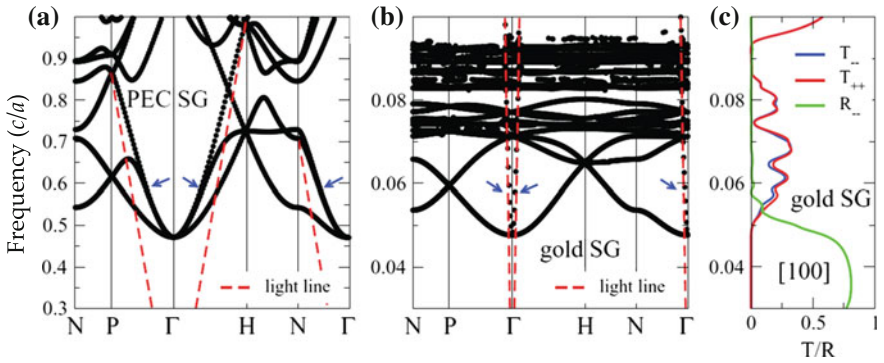

Fig. 2.11 Gyroid optical metamaterial band diagrams and transmittance and reflectance spectra. **a** Band diagram for a perfect electrical conductor (PEC) gyroid with 40 nm unit cell size and 10% volume fill fraction. **b** Band diagram of an equivalent gold gyroid, where the gold is modelled as a Drude metal. High-symmetry directions (N, P, and H) labelled according to Fig. 2.2. Reduced frequency (c/a), where c is the speed of light in free space and a is the unit cell size. **c** Transmittance (T) and reflectance (R) spectra of the same gold gyroid along the [100] direction. The subscripts "++" and "−−" refer to right and left circularly polarised light, respectively. Reprinted (adapted) from [109] with permission from John Wiley and Sons

to predict with reasonable accuracy the plasma frequency of the metamaterial. Confirming the qualitative explanation offered previously, the plasma frequency is indeed significantly red-shifted due to the self-inductance of the structure. Notwithstanding the effect of a finite cross-coupling between circular polarisations upon the reflectance and transmittance spectra for light incident on a finite slab of PEC gyroid, the spectra also differ significantly for right- and left-handed circularly polarised light, confirming theoretically the circular dichroism of the metamaterial, particularly along the [111] and [100] directions [109].

Whereas comparison between the PEC THM and PEC gyroid highlights structural contributions to the electromagnetic response of the gyroid optical metamaterial, comparison between a PEC gyroid and gold gyroid highlights the material contribution. A gyroid composed of gold (modelled as a Drude metal) was calculated to exhibit bands which were red-shifted ten-fold compared to the PEC gyroid due to the penetration of the electromagnetic field into the wires (Fig. 2.11). Accounting for the induced current resulting from complete penetration of the metal by the surrounding electromagnetic fields allows the analytical derivation of the plasma frequency of a gold THM. Using this improved THM model allows quantitative prediction of the effect of unit cell size, volume fill fraction, and host dielectric constant on the optical properties of the metamaterial.[20] Differences between the analytical and numerically calculated plasma wavelengths were attributed to high density localised plasmon modes not accounted for in the model. These localised

[20]These predictions are revisited in Chap. 6, in which an effective medium model of multi-domain gyroid optical metamaterials is similarly used to predict the effect of volume fill fraction and host dielectric constant.

plasmon modes, resulting from the three-dimensional structure of the gyroid, appear relatively fixed in frequency as the fill fraction of the gyroid increases, unlike the propagating modes. When the fill fraction is around 30%, that of the experimentally fabricated gold gyroid, the propagating modes are immersed in the frequency range of the localised plasmon modes which, due to their absorptive character, affect the transmittance and reflectance spectra. Again, circular dichroism is identified in the gold gyroid, but the magnitude of the dichroism is much smaller than for the PEC gyroid. This is attributed to improved impedance matching between the gyroid and its surroundings, the penetration of the electromagnetic field into the gyroid, and increased losses. Material properties therefore appear to affect the circular dichroism of the metamaterial gyroid more significantly than its structural properties.

Recently a more succinct set of approximate analytical expressions for the permittivity and extinction peak of the gold gyroid optical metamaterial have been derived [110]. Building on the above THM work, Farah et al. demonstrated that the effective permittivity of the gold gyroid ε_{gyr} can be approximated as

$$\varepsilon_{\text{gyr}} = \frac{l\sqrt{2}}{a}\left[1 - \left(\frac{4r_{\text{g}}}{\lambda_{\text{g}}}\right)^2 \left(\frac{\pi\sqrt{-\varepsilon_{\text{m}}}}{2\sqrt{2}n_{\text{fill}}} - 1\right)^2\right], \tag{2.5}$$

where l is the normalised helix length, a is the unit cell size, $r_{\text{g}} \approx 0.29a\sqrt{f}$ is the smallest radius of the gyroid strut, f is the volume fill fraction, n_{fill} is the refractive index of the surrounding medium, and λ_{g} is the effective plasma wavelength of a PEC gyroid. Finally, ε_{m} is the permittivity of gold when fashioned into 10 nm diameter struts (e.g. taking into account the polycrystalline nature of the metal). Furthermore, the wavelength of the extinction peak was also derived based on a number of further assumptions and the condition that minimum reflection occurs when $\Re\left\{\varepsilon_{\text{gyr}}\right\} = \varepsilon_{\text{air}} = 1$. The wavelength of the dip in reflectivity λ_{dip} (i.e. the extinction peak) is therefore given as

$$\frac{\lambda_{\text{dip}}^2}{\lambda_{\text{p}}^2} = \varepsilon_\infty + \frac{8n_{\text{fill}}^2}{\pi^2}\left(1 + \frac{\eta\lambda_{\text{g}}}{4r_{\text{g}}}\right)^2, \tag{2.6}$$

where, say, for gold modelled as a Drude metal, $\lambda_{\text{p}} = 146\,\text{nm}$, $\varepsilon_\infty = 7$, and $\eta^2 = 1 - a/l\sqrt{2}$. Despite the inability of the model to account for the anisotropic response of the gold gyroid optical metamaterials, the above equation was shown to predict remarkably well the extinction peaks in the reflection spectra for a 35 nm gold gyroid with different refractive indices of the surrounding medium.

Although much is understood about the optical properties of gyroid optical metamaterials, including the behaviour of the plasma edge and the origin of the circular dichroism, the nature of the linear dichroism remains a mystery [109]. Similarly, suitable estimates of the effective material parameters remain elusive, thereby hindering a true appraisal of the metamaterial's potential utility. For example, the THM model and its derivative above, otherwise successful at modelling various optical

properties of the metamaterial, do not describe the linear dichroism of gyroid optical metamaterial. Indeed, the linear dichroism is thoroughly unexpected given the cubic symmetry of the single gyroid. Similarly, the model is unsuitable to average over an ensemble of small multi-domains of random orientation and handedness, such as may be obtained through thermal annealing of the triblock terpolymer. It is therefore also of interest to correctly identify the effective material parameters of gyroid metamaterials and to understand to what extent the ordered sub-wavelength structure continues to affect the optical response when the macroscopic order is relatively poor.

References

1. Wohlgemuth, M., Yufa, N., Hoffman, J., & Thomas, E. L. (2001). Triply periodic bicontinuous cubic microdomain morphologies by symmetries. *Macromolecules*, *34*, 6083–6089.
2. Saba, M., Turner, M. D., Mecke, K., Gu, M., & Schröder-Turk, G. E. (2013). Group theory of circular-polarization effects in chiral photonic crystals with four-fold rotation axes applied to the eight-fold intergrowth of gyroid nets. *Physical Review B*, *88*, 245116.
3. Dolan, J. A., Wilts, B. D., Vignolini, S., Baumberg, J. J., Steiner, U., & Wilkinson, T. D. (2015). Optical properties of gyroid structured materials: From photonic crystal to metamaterials. *Advanced Optical Materials*, *3*, 12–32.
4. Grosse-Brauckmann, K. (1997). On gyroid interfaces. *Journal of Colloid and Interface Science*, *187*, 418–428.
5. Hyde, S. T., & Schröder-Turk, G. E. (2012). Geometry of interfaces: Topological complexity in biology and materials. *Interface Focus*, *2*, 529–538.
6. Saba, M., Wilts, B. D., Hielscher, J., & Schröder-Turk, G. E. (2014). Absence of circular polarisation in reflections of butterfly wing scales with chiral gyroid structure. *Materials Today: Proceedings*, *1*, 193–208.
7. Hiemenz, P., & Lodge, T. (2007). *Polymer Chemistry*. London: Taylor & Francis. ISBN 9781574447798.
8. Strobl, G. (2007). *The physics of polymers: Concepts for understanding their structures and behavior*. Berlin: Springer. ISBN 9783540684114.
9. Crossland, E., Snaith, H. & Steiner, U. (2016). *Electrochemical nanofabrication: Principles and applications*. In D. Wei (Ed.) (pp. 59-111). California: Pan Stanford. ISBN: 978- 981-4613-86-6.
10. Stefik, M., Guldin, S., Vignolini, S., Wiesner, U., & Steiner, U. (2015). Block copolymer self-assembly for nanophotonics. *Chemical Society Reviews*, *44*(15), 5076–5091.
11. Hsueh, H.-Y., Yao, C.-T., & Ho, R.-M. (2015). Well-ordered nanohybrids and nanoporous materials from gyroid block copolymer templates. *Chemical Society Reviews*, *44*(7), 1974–2018.
12. Albert, J. N. L., Bogart, T. D., Lewis, R. L., Beers, K. L., Fasolka, M. J., Hutchison, J. B., et al. (2011). Gradient solvent vapor annealing of block copolymer thin films. *Nano Letters*, *11*, 1351–1357.
13. Segalman, R. A. (2005). Patterning with block copolymer thin films. *Materials Science and Engineering: R: Reports*, *48*, 191–226.
14. Darling, S. B. (2007). Directing the self-assembly of block copolymers. *Progress in Polymer Science*, *32*, 1152–1204.
15. Koo, K., Ahn, H., Kim, S.-W., Ryu, D. Y., & Russell, T. P. (2013). Directed self-assembly of block copolymers in the extreme: Guiding microdomains from the small to the large. *Soft Matter*, *9*, 9059.

16. She, M.-S., Lo, T.-Y., Hsueh, H.-Y., & Ho, R.-M. (2013). Nanostructured thin films of degradable block copolymers and their applications. *NPG Asia Materials*, *5*, e42.
17. Mai, Y., & Eisenberg, A. (2012). Self-assembly of block copolymers. *Chemical Society Reviews*, *41*, 5969–5985.
18. Hamley, I. W. (2009). Ordering in thin films of block copolymers: Fundamentals to potential applications. *Progress in Polymer Science*, *34*, 1161–1210.
19. Hyde, S. (1997). *The language of shape: The role of curvature in condensed matter: physics, chemistry and biology*. Amsterdam: Elsevier. ISBN 0444815384.
20. Scherer, M. R. J. (2013). *Double-gyroid-structured functional materials* (2013 ed.). Berlin: Springer. ISBN: 3319003534.
21. Cochran, E. W., Garcia-Cervera, C. J., & Fredrickson, G. H. (2006). Stability of the gyroid phase in diblock copolymers at strong segregation. *Macromolecules*, *39*, 2449–2451.
22. Vigild, M. E., Almdal, K., Mortensen, K., Fairclough, J. P. A., & Ryan, A. J. (1998). Transformations to and from the gyroid phase in a diblock copolymer. *Macromolecules*, *31*, 5702–5716.
23. Wang, C.-Y., & Lodge, T. P. (2002). Kinetics and mechanisms for the cylinder-to-gyroid transition in a block copolymer solution. *Macromolecules*, *35*, 6997–7006.
24. Chatterjee, J., Jain, S., & Bates, F. S. (2007). Comprehensive phase behavior of poly(isoprene-b-styrene- b-ethylene oxide) triblock copolymers. *Macromolecules*, *40*, 2882–2896.
25. Bates, F. S., & Fredrickson, G. H. (1990). Block copolymer thermodynamics: Theory and experiment. *Annual Review of Physical Chemistry*, *41*, 525–557.
26. Bates, F. S., & Fredrickson, G. H. (1999). Block copolymers-designer soft materials. *Physics Today*, *52*, 32.
27. Meuler, A. J., Hillmyer, M. A., & Bates, F. S. (2009). Ordered network mesostructures in block polymer materials. *Macromolecules*, *42*, 7221–7250.
28. Tyler, C., & Morse, D. (2005). Orthorhombic Fddd network in triblock and diblock copolymer melts. *Physical Review Letters*, *94*, 208302.
29. Epps, T. H., Cochran, E. W., Hardy, C. M., Bailey, T. S., Waletzko, R. S., & Bates, F. S. (2004). Network phases in ABC triblock copolymers. *Macromolecules*, *37*, 7085–7088.
30. Bailey, T. S., Hardy, C. M., Epps, T. H., & Bates, F. S. (2002). A noncubic triply periodic network morphology in poly(isoprene- b-styrene- b-ethylene oxide) triblock copolymers. *Macromolecules*, *35*, 7007–7017.
31. Epps, T. H., Cochran, E. W., Bailey, T. S., Waletzko, R. S., Hardy, C. M., & Bates, F. S. (2004). Ordered network phases in linear poly(isoprene-b-styrene-b-ethylene oxide) triblock copolymers. *Macromolecules*, *37*, 8325–8341.
32. Epps, T. H., & Bates, F. S. (2006). Effect of molecular weight on network formation in linear ABC triblock copolymers. *Macromolecules*, *39*, 2676–2682.
33. Gu, X., Gunkel, I., Hexemer, A., & Russell, T. P. (2016). Controlling domain spacing and grain size in cylindrical block copolymer thin films by means of thermal and solvent vapor annealing. *Macromolecules*, *49*, 3373–3381.
34. Baruth, A., Seo, M., Lin, C. H., Walster, K., Shankar, A., Hillmyer, M. A., et al. (2014). Optimization of long-range order in solvent vapor annealed poly(styrene)-block-poly(lactide) thin films for nanolithography. *ACS Applied Materials & Interfaces*, *6*, 13770–13781.
35. Gu, X., Gunkel, I., Hexemer, A., Gu, W., & Russell, T. P. (2014). An in situ grazing incidence X-ray scattering study of block copolymer thin films during solvent vapor annealing. *Advanced Materials*, *26*, 273–281.
36. Sinturel, C., Morris, M., & Hillmyer, M. A. (2013). Solvent vapor annealing of block polymer thin films. *Macromolecules*, *46*, 5399–5415.
37. Posselt, D., Zhang, J., Smilgies, D.-M., Berezkin, A., Potemkin, I. I., & Papadakis, C. M. (2016). *Restructuring in block copolymer thin films: In situ GISAXS investigations during solvent vapor annealing*. *Progress in Polymer Science* (In Press).
38. Paik, M. Y., Bosworth, J. K., Smilges, D.-M., Schwartz, E. L., Andre, X., & Ober, C. K. (2010). Reversible morphology control in block copolymer films via solvent vapor processing: An in situ GISAXS study. *Macromolecules*, *43*, 4253–4260.

39. Chavis, M. A., Smilgies, D. M., Wiesner, U. B., & Ober, C. K. (2015). Widely tunable morphologies in block copolymer thin films through solvent vapor annealing using mixtures of selective solvents. *Advanced Functional Materials*, *25*, 3057–3065.
40. Albalak, R. J., Capel, M. S., & Thomas, E. L. (1998). Solvent swelling of roll-cast triblock copolymer films. *Polymer*, *39*, 1647–1656.
41. Kim, G., & Libera, M. (1998). Morphological development in solvent-cast polystyrenepolybutadiene- polystyrene (SBS) triblock copolymer thin films. *Macromolecules*, *31*, 2569–2577.
42. Albert, J. N. L., Young, W.-S., Lewis, R. L., Bogart, T. D., Smith, J. R., & Epps, T. H. (2012). Systematic study on the effect of solvent removal Rrte on the morphology of solvent vapor annealed ABA triblock copolymer thin films. *ACS Nano*, *6*, 459–466.
43. Seppala, J. E., Lewis, R. L., & Epps, T. H. (2012). Spatial and orientation control of cylindrical nanostructures in ABA triblock copolymer thin films by raster solvent vapor annealing. *ACS Nano*, *6*, 9855–9862.
44. Xiong, S., Wan, L., Ishida, Y., Chapuis, Y. A., Craig, G. S. W., Ruiz, R., et al. (2016). Directed self-assembly of triblock copolymer on chemical patterns for sub- 10-nm nanofabrication via solvent annealing. *ACS Nano*, *10*, 7855–7865.
45. Fukunaga, K., Elbs, H., Magerle, R., & Krausch, G. (2000). Large-scale alignment of ABC block copolymer microdomains via solvent vapor treatment. *Macromolecules*, *33*, 947–953.
46. Elbs, H., Drummer, C., Abetz, V., & Krausch, G. (2002). Thin film morphologies of ABC triblock copolymers prepared from solution. *Macromolecules*, *35*, 5570–5577.
47. Fukunaga, K., Hashimoto, T., Elba, H., & Krausch, G. (2003). Self-assembly of a lamellar ABC triblock terpolymer thin film. *Effect of substrates. Macromolecules*, *36*, 2852–2861.
48. Luo, C., Huang, W., & Han, Y. (2009). Formation of two kinds of hexagonally arranged structures in ABC triblock copolymer thin films induced by a strongly selective solvent vapor. *Macromolecular Rapid Communications*, *30*, 1917–1921.
49. Luo, C., Huang, W., & Han, Y. (2009). Order-order transition of C → sdG → sL → S in ABC triblock copolymer thin film induced by solvent vapor. *Macromolecular Rapid Communications*, *30*, 515–520.
50. Yu, X., Luo, C., Zhao, Q., Yang, H., & Han, Y. (2014). Order-order transitions of a triblock copolymer with a homopolymer (ABC/A) blend film induced by saturated solvent vapor annealing. *Journal of Polymer Science, Part B: Polymer Physics*, *52*, 1030–1036.
51. Hong, S., Higuchi, T., Sugimori, H., Kaneko, T., Abetz, V., Takahara, A., et al. (2012). Highly oriented and ordered double-helical morphology in ABC triblock terpolymer films up to micrometer thickness by solvent evaporation. *Polymer Journal*, *44*, 567–572.
52. Deng, G., Zhang, Y., Ye, C., Qiang, Z., Stein, G. E., Cavicchi, K. A., et al. (2014). Bicontinuous mesoporous carbon thin films via an order-order transition. *Chemical Communications*, *50*, 12684–7.
53. She, M.-S., Lo, T.-Y., & Ho, R.-M. (2014). Controlled ordering of block copolymer gyroid thin films by solvent annealing. *Macromolecules*, *47*, 175–182.
54. Wu, Y.-H., Lo, T.-Y., She, M.-S., & Ho, R.-M. (2015). Morphological evolution of gyroidforming block copolymer thin films with varying solvent evaporation rate. *ACS Applied Materials & Interfaces*, *7*, 16536–16547.
55. He, W.-N., & Xu, J.-T. (2012). Crystallization assisted self-assembly of semicrystalline block copolymers. *Progress in Polymer Science*, *37*, 1350–1400.
56. Nandan, B., Hsu, J.-Y., & Chen, H.-L. (2006). Crystallization behavior of crystallineamorphous diblock copolymers consisting of a rubbery amorphous block. *Journal of Macromolecular Science, Part C: Polymer Reviews*, *46*, 143–172.
57. Zhu, L., Chen, Y., Zhang, A. Q., Calhoun, B. H., Chun, M. S., Quirk, R. P., et al. (1999). Phase structures and morphologies determined by competitions among self-organization, crystallization, and vitrification in a disordered poly(ethylene oxide)- b-polystyrene diblock copolymer. *Physical Review B*, *60*, 10022–10031.
58. Loo, Y.-L., Register, R. A., & Ryan, A. J. (2002). Modes of crystallization in block copolymer microdomains: breakout, templated, and confined. *Macromolecules*, *35*, 2365–2374.

59. Quiram, D. J., Register, R. A., & Marchand, G. R. (1997). Crystallization of asymmetric diblock copolymers from microphase-separated melts. *Macromolecules*, *30*, 4551–4558.
60. Xu, J., Liang, G., & Fan, Z. (2004). Comparison of crystallization rate and macroscopic morphology of two oxyethylene/oxybutylene triblock copolymers. The effect of molecular architecture. *Polymer Journal*, *36*, 465–471.
61. Kim, G., Han, C. C., Libera, M., & Jackson, C. L. (2001). Crystallization within melt ordered semicrystalline block copolymers: exploring the coexistence of microphase-separated and spherulitic morphologies. *Macromolecules*, *34*, 7336–7342.
62. Floudas, G., Ulrich, R., & Wiesner, U. (1999). Microphase separation in poly(isoprene-b-ethylene oxide) diblock copolymer melts. I. Phase state and kinetics of the order-to-order transitions. *The Journal of Chemical Physics*, *110*, 652.
63. Xu, J. T., Turner, S. C., Fairclough, J. P. A., Mai, S. M., Ryan, A. J., Chaibundit, C., et al. (2002). Morphological confinement on crystallization in blends of poly(oxyethylene-block-oxybutylene) and poly(oxybutylene). *Macromolecules*, *35*, 3614–3621.
64. Balsamo, V., Navarro, C. U. D., & Gil, G. (2003). Microphase separation vs crystallization in polystyrene- b-polybutadiene- b-poly(ε-caprolactone) ABC triblock copolymers. *Macromolecules*, *36*, 4507–4514.
65. Xu, J.-T., Liang, G.-D., & Fan, Z.-Q. (2004). Polarized optical microscopy study on the superstructures of oxyethylene/oxybutylene block copolymers. *Polymer*, *45*, 6675–6680.
66. Tsitsilianis, C., Staikos, G., Dondos, A., Lutz, P., & Rempp, P. (1992). Influence of annealing and casting solvent on the morphology of poly(ethylene oxide)- b-polystyrene- b-poly(ethylene oxide) triblock copolymer: compatibility effects. *Polymer*, *33*, 3369–3374.
67. Balsamo, V., von Gyldenfeldt, F., & Stadler, R. (1996). Thermal behavior and spherulitic superstructures of SBC triblock copolymers based on polystyrene (S), polybutadiene (B) and a crystallizable poly(ε-caprolactone) (C) block. *Macromolecular Chemistry and Physics*, *197*, 3317–3341.
68. Floudas, G., & Tsitsilianis, C. (1997). Crystallization kinetics of poly(ethylene oxide) in poly(ethylene oxide)-polystyrene-poly(ethylene oxide) triblock copolymers. *Macromolecules*, *30*, 4381–4390.
69. Balsamo, V., & Stadler, R. (1999). Influence of the crystallization temperature on the microphase morphology of a semicrystalline ABC triblock copolymer. *Macromolecules*, *32*, 3994–3999.
70. Grigorova, T., Pispas, S., Hadjichristidis, N., & Thurn-Albrecht, T. (2005). Magnetic field induced orientation in diblock copolymers with one crystallizable block. *Macromolecules*, *38*, 7430–7433.
71. Liu, L.-Z., Xu, W., Li, H., Su, F., & Zhou, E. (1997). Crystallization and intriguing morphologies of compatible mixtures of tetrahydrofuran-methyl methacrylate diblock copolymer with poly(tetrahydrofuran). *Macromolecules*, *30*, 1363–1374.
72. Zhu, L., Cheng, S. Z. D., Calhoun, B. H., Ge, Q., Quirk, R. P., Thomas, E. L., et al. (2000). Crystallization temperature-dependent crystal orientations within nanoscale confined lamellae of a self-assembled crystallineamorphous diblock copolymer. *Journal of the American Chemical Society*, *122*, 5957–5967.
73. Huang, P., Zhu, L., Cheng, S. Z. D., Ge, Q., Quirk, R. P., Thomas, E. L., et al. (2001). Crystal orientation changes in two-dimensionally confined nanocylinders in a poly(ethylene oxide)-b-polystyrene/polystyrene blend. *Macromolecules*, *34*, 6649–6657.
74. Huang, P., Guo, Y., Quirk, R. P., Ruan, J., Lotz, B., Thomas, E. L., et al. (2006). Comparison of poly(ethylene oxide) crystal orientations and crystallization behaviors in nano-confined cylinders constructed by a poly(ethylene oxide)- b-polystyrene diblock copolymer and a blend of poly(ethylene oxide)- b-polystyrene and polystyrene. *Polymer*, *47*, 5457–5466.
75. Zhu, B. L., Cheng, S. Z. D., Huang, P., Ge, Q., Quirk, R. P., Thomas, E. L., et al. (2002). Nanoconfined polymer crystallization in the hexagonally perforated layers of a self-assembled PS- b-PEO diblock copolymer. *Advanced Materials*, *14*, 31–34.
76. Zhu, L., Huang, P., Chen, W. Y., Ge, Q., Quirk, R. P., Cheng, S. Z. D., et al. (2002). Nanotailored crystalline morphology in hexagonally perforated layers of a self-assembled PS- b-PEO diblock copolymer. *Macromolecules*, *35*, 3553–3562.

77. Huang, P., Zheng, J. X., Leng, S., Van Horn, R. M., Jeong, K. U., Guo, Y., et al. (2007). Poly(ethylene oxide) crystal orientation changes in an inverse hexagonal cylindrical phase morphology constructed by a poly(ethylene oxide)-block- polystyrene diblock copolymer. *Macromolecules*, *40*, 526–534.
78. Yang, P., & Han, Y. (2009). Crystal growth transition from flat-on to edge-on induced by solvent evaporation in ultrathin films of polystyrene-b-poly(ethylene oxide). *Langmuir*, *25*, 9960–9968.
79. Yang, P., Yu, X., & Han, Y. (2010). Transition between crystallization and microphase separation in PS- b-PEO thin film influenced by solvent vapor selectivity. *Polymer*, *51*, 4948–4957.
80. Hamley, I. W., Fairclough, J. P. A., Terrill, N. J., Ryan, A. J., Lipic, P. M., Bates, F. S., et al. (1996). Crystallization in oriented semicrystalline diblock copolymers. *Macromolecules*, *29*, 8835–8843.
81. Liang, G.-D., Xu, J.-T., & Fan, Z.-Q. (2007). Lamellar orientation in thin films of symmetric semicrytalline polystyrene-b-poly(ethylene-co-butene) block copolymers: Effects of molar mass, temperature of solvent evaporation, and annealing. *Journal of Physical Chemistry B*, *111*, 11921–11928.
82. Sun, L., Zhu, L., Ge, Q., Quirk, R. P., Xue, C., Cheng, S. Z. D., et al. (2004). Comparison of crystallization kinetics in various nanoconfined geometries. *Polymer*, *45*, 2931–2939.
83. Loo, Y.-L., Register, R. A., Ryan, A. J., & Dee, G. T. (2001). Polymer crystallization confined in one, two, or three dimensions. *Macromolecules*, *34*, 8968–8977.
84. Weimann, P. A., Hajduk, D. A., Chu, C., Chaffin, K. A., Brodil, J. C., & Bates, F. S. (1999). Crystallization of tethered polyethylene in confined geometries. *Journal of Polymer Science Part B: Polymer Physics*, *37*, 2053–2068.
85. Fairclough, J. P. A., Mai, S.-M., Matsen, M. W., Bras, W., Messe, L., Turner, S. C., et al. (2001). Crystallization in block copolymer melts: Small soft structures that template larger hard structures. *The Journal of Chemical Physics*, *114*, 5425.
86. Müller, A. J., Balsamo, V., Arnal, M. L., Jakob, T., Schmalz, H., & Abetz, V. (2002). Homogeneous nucleation and fractionated crystallization in block copolymers. *Macromolecules*, *35*, 3048–3058.
87. Cai, W., & Shalaev, V. (2010). *Optical metamaterials*. Berlin: Springer. ISBN 978-1-4419-1151-3.
88. Demetriadou, A., & Pendry, J. B. (2008). Taming spatial dispersion in wire metamaterial. *Journal of Physics: Condensed Matter*, *20*, 295222.
89. Veselago, V. G. (1968). The electrodynamics of substances with simultaneously negative values of ε and μ. *Soviet Physics Uspekhi*, *10*, 509–514.
90. Veselago, V. G., & Narimanov, E. E. (2006). The left hand of brightness: Past, present and future of negative index materials. *Nature Materials*, *5*, 759–62.
91. Smith, D. R., Padilla, W. J., Vier, D. C., Nemat-Nasser, S. C., & Schultz, S. (2000). Composite medium with simultaneously negative permeability and permittivity. *Physical Review Letters*, *84*, 4184–7.
92. Pendry, J. B., Schurig, D., & Smith, D. R. (2011). Controlling electromagnetic fields. *Science*, *1780*, 1780–1782.
93. Pendry, J. B. (2000). Negative refraction makes a perfect lens. *Physical Review Letters*, *85*, 3966–9.
94. Pendry, J. B. (2004). A chiral route to negative refraction. *Science*, *306*, 1353–1355.
95. Zhang, S., Park, Y.-S., Li, J., Lu, X., Zhang, W., & Zhang, X. (2009). Negative refractive index in chiral metamaterials. *Physical Review Letters*, *102*, 023901.
96. Plum, E., Zhou, J., Dong, J., Fedotov, V., Koschny, T., Soukoulis, C., et al. (2009). Metamaterial with negative index due to chirality. *Physical Review B*, *79*, 035407.
97. Li, Z., Mutlu, M., & Ozbay, E. (2013). Chiral metamaterials: From optical activity and negative refractive index to asymmetric transmission. *Journal of Optics*, *15*, 023001.
98. Valev, V. K., Baumberg, J. J., Sibilia, C., & Verbiest, T. (2013). Chirality and chiroptical effects in plasmonic nanostructures: Fundamentals, recent progress, and outlook. *Advanced Materials*, *25*, 2517–34.

99. Poddubny, A., Iorsh, I., Belov, P., & Kivshar, Y. (2013). *Hyperbolic metamaterials. Nature Photonic*, *7*, 948–957.
100. Silin, R. A. (1972). Optical properties of artificial dielectrics (review). *Radiophysics and Quantum Electronics*, *15*, 615–624.
101. Boltasseva, A., & Shalaev, V. M. (2008). Fabrication of optical negative-index metamaterials: recent advances and outlook. *Metamaterials*, *2*, 1–17.
102. Soukoulis, C. M., & Wegener, M. (2011). Past achievements and future challenges in the development of three-dimensional photonic metamaterials. *Nature Photonics*, *5*, 523–530.
103. Hur, K., Francescato, Y., Giannini, V., Maier, S. A., Hennig, R. G., & Wiesner, U. (2011). Three-dimensionally isotropic negative refractive index materials from block copolymer self-assembled chiral gyroid networks. *Angewandte Chemie International Edition*, *50*, 11985–9.
104. Vignolini, S., Yufa, N. A., Cunha, P. S., Guldin, S., Rushkin, I., Stefik, M., et al. (2012). A 3D optical metamaterial made by self-assembly. *Advanced Materials*, *24*, OP23–OP27.
105. Salvatore, S. (2014). *Optical metamaterials by block copolymer self-assembly (Springer theses)*. Berlin: Springer. ISBN 3319053310.
106. Salvatore, S., Demetriadou, A., Vignolini, S., Oh, S. S., Wuestner, S., Yufa, N. A., et al. (2013). Tunable 3D extended self-assembled gold metamaterials with enhanced light transmission. *Advanced Materials*, *25*, 2713–2716.
107. Pendry, J. B., Holden, A. J., Stewart, W. J., & Youngs, I. (1996). Extremely low frequency plasmons in metallic mesostructures. *Physical Review Letters*, *76*, 4773–4776.
108. Demetriadou, A., Oh, S. S., Wuestner, S., & Hess, O. (2012). A tri-helical model for nanoplasmonic gyroid metamaterials. *New Journal of Physics*, *14*, 083032.
109. Oh, S. S., Demetriadou, A., Wuestner, S., & Hess, O. (2013). On the origin of chirality in nanoplasmonic gyroid metamaterials. *Advanced Materials*, *25*, 612–7.
110. Farah, P., Demetriadou, A., Salvatore, S., Vignolini, S., Stefik, M., Wiesner, U., et al. (2014). Ultrafast nonlinear response of gold gyroid three-dimensional metamaterials. *Physical Review Applied*, *2*, 044002.

Chapter 3
Methods

In this chapter, the experimental methods used to fabricate and characterise the triblock terpolymer thin films, and the resulting gyroid optical metamaterials, are introduced.

3.1 Terpolymer Thin Films

Polyisoprene-*b*-polysytrene-*b*-poly(ethylene oxide) (ISO) triblock terpolymers with molecular weights of 33 kg mol^{-1} (Chap. 4) and 80 kg mol^{-1} (Chaps. 5–7) were prepared by anionic polymerisation following synthesis procedures reported elsewhere [1, 2].[1] The block volume fractions of the 33 kg mol^{-1} terpolymer are $f_{PI} = 0.308$, $f_{PS} = 0.523$, and $f_{PEO} = 0.169$, respectively; the block volume fractions of the 80 kg mol^{-1} terpolymer are $f_{PI} = 0.30$, $f_{PS} = 0.532$, and $f_{PEO} = 0.168$, respectively. Thin films of the ISO terpolymer were prepared atop either silicon (for scattering measurements described below) or fluorine-doped tin oxide (FTO)-coated glass substrates (for optical metamaterial fabrication). The FTO-coated glass substrates were cleaned using a Piranha etch and subsequently functionalised by immersion for 15 s in a 0.2% solution (v/v) of octyltrichlorosilane (Sigma-Aldrich) in anhydrous cyclohexane (Sigma-Aldrich). The silicon substrates were cleaned by exposure to an oxygen plasma (Diener MRC 100 at 100% power for 2 min) without subsequent functionalisation. The thin films were spun from a 10% (w/w) solution of ISO terpolymer in anhydrous anisole (Sigma-Aldrich) for 60 s at 1200 rpm with an acceleration of

[1] The 33 and 80 kg mol^{-1} ISO triblock terpolymers were synthesised by Drs. Morgan Stefik and Yibei Gu, respectively, whilst students under the supervision of Prof. Ulrich Wiesner, Cornell University, USA.

© Springer Nature Switzerland AG 2018

J. A. Dolan, *Gyroid Optical Metamaterials*, Springer Theses,
https://doi.org/10.1007/978-3-030-03011-7_3

500 rpm s^{-1}. The resulting film thicknesses were ≈ 650 nm and ≈ 770 nm for the 33 and 80 kg mol^{-1} terpolymers, respectively, as determined by thin film interferometry (see below).

3.2 Differential Scanning Calorimetry

Differential scanning calorimetry (DSC) of the 80 kg mol^{-1} ISO triblock terpolymer was carried out using a Mettler Toledo DSC 2 (Chap. 5).[2] Bulk samples were loaded into aluminum DSC pans and then sealed with aluminum lids. The samples were initially heated to 125°C, then cooled to −80°C, and finally heated again to 125°C, all at 10°C min^{-1}. The first heating scan was ignored when determining the glass transitions temperatures of the PS and PI blocks and the melting temperature of the PEO block. The DSC measurement was repeated twice.

3.3 Annealing

The majority of the ISO triblock terpolymer thin films studied in this thesis were solvent-annealed (Chaps. 4, 5, and 7). However, when fabricating terpolymer templates with only short-range order, thermal annealing was also employed (Chap. 6).

3.3.1 Thermal Annealing

Samples were thermally annealed under vacuum at 180°C for 30 min (ramp rate 150°C h^{-1}) then allowed to cool over approximately 12 h (Chap. 6).

3.3.2 In Situ Solvent Vapour Annealing

Samples were exposed to controlled amounts of solvent vapour using a custom annealing chamber and associated experimental set-up (Chap. 4). The polyetheretherketone (PEEK) annealing chamber possessed sealed Kapton windows on two sides (for transmission of the incident and scattered X-ray beams) and a sealed quartz glass window in the lid (for measurement of the film thickness during annealing). Up to three gas lines could be mixed to control the solvent atmosphere in the chamber: one flowing only dry nitrogen and the other two flowing nitrogen bubbled through a solvent. By varying the mass flow rate of gas in each line with three independently

[2]DSC was performed by Dr. Ilja Gunkel, Adolphe Merkle Institute, Switzerland.

controlled mass flow controllers (MKS Type MF1, flow range 100 sccm, MKS Type 647 multichannel gas flow controller unit), the ratio of saturated to dry nitrogen (i.e. the "concentration" of the solvent or mixed solvent vapours in the chamber) was controlled. Custom-built software determined and controlled the required mass flow rates given a desired solvent vapour concentration, solvent vapour mixture ratio, and total mass flow rate, allowing automated implementation of desired solvent annealing protocols. Chloroform, tetrahydrofuran, and methanol (Sigma-Aldrich) were employed as solvents. Unless otherwise noted, the total mass flow rate of nitrogen in all lines was maintained at 20 sccm throughout. Upon exiting the chamber, the gas mixture flowed to an exhaust line through a manual mass flow controller which could be adjusted to ensure a sufficient solvent vapour pressure in the annealing chamber. The temperature of the sample within the annealing chamber was controlled using a Peltier element and copper plate, and the temperature of the solvent reservoirs using a water bath. Unless otherwise noted, the temperature of the solvent remained $\approx 23.0°C$ throughout, whereas the temperature of the sample was varied between ≈ 21.3–$24.4°C$, depending on the swelling ratio required (a lower sample temperature resulting in greater swelling). The temperature of the solvent was chosen to be close to room temperature ($\approx 23.7°C$) to avoid condensation of the solvent vapour in the gas lines. The ambient relative humidity remained constant at $\approx 33\%$.

3.3.3 Ex Situ Solvent Vapour Annealing

Samples were exposed to controlled solvent vapour atmospheres using a custom-built experimental set-up, different from, although similar to, that described above (Chaps. 5 and 7). Dry nitrogen gas was bubbled through a chloroform (Sigma-Aldrich) reservoir and mixed with dry nitrogen before entering a sealed Teflon annealing chamber. The ratio of saturated to dry nitrogen was controlled by independently varying the mass flow rate of both lines with two MKS Type 1179A mass flow controllers (100 sccm flow range; MKS PR4000B digital power supply). The total mass flow rate of nitrogen in the two lines was maintained at 20 sccm. The mass flow rate of the nitrogen bubbled through the chloroform reservoir (i.e. the proportion of saturated carrier gas) typically varied between 70–80% of the total mass flow rate, depending on the particular annealing protocol employed. The temperature of the solvent reservoir and sample were controlled using a water bath and Peltier element, respectively. The temperature of the water bath was held at $\approx 26°C$ and the Peltier element at $\approx 21°C$ (i.e. just below ambient room temperature). Although possible under some annealing conditions, condensation of the solvent vapour on the sample substrate was avoided in this work. The gas lines and solvent reservoir were kept at the temperature of the bath to prevent condensation of the solvent vapour.

3.4 Film Thickness Measurements

The thickness of the terpolymer thin film during in situ solvent vapour annealing was measured interferometrically using an Avantes AvaLight-DH-S-BAL deuterium halogen light source (only the halogen source was used here; 500–2500 nm wavelength range) and Avantes AvaSpec 2048L spectrometer (Chap. 4). Light was coupled through a bifurcated optical fibre (FCR-12UV200/600-2-ME) and focussed onto the sample via a collimator (FCR-COL UV/VIS). The thickness was estimated by assuming a refractive index $n = 1.5$ of the terpolymer film. The swelling ratio is a dimensionless measure of relative film thickness and is defined as

$$\varphi = \frac{t}{t_0}, \tag{3.1}$$

where t is the current (swollen) thickness and t_0 is the initial thickness of the as-spun film (i.e. before application of any solvent). Assuming no in-plane motion of the film during annealing, the swelling ratio is simply the reciprocal of the volume fraction of polymer in the swollen film.

3.5 Grazing-Incidence Small- and Wide-Angle X-Ray Scattering

Grazing-incidence small-angle X-ray scattering (GISAXS) measurements were performed at both the Paul Scherrer Institute, Swizterland (Chap. 4), and the Cornell High Energy Synchrotron Source, USA (Chap. 5). Grazing-incidence wide-angle X-ray scattering (GIWAXS) measurements were performed at the Cornell High Energy Synchrotron Source, USA (Chap. 5).

3.5.1 Paul Scherrer Institute

GISAXS measurements were performed in situ during solvent vapour annealing at the cSAXS beamline of the Swiss Light Source, Paul Scherrer Institute, Villigen, Switzerland (Chap. 4).[3] The X-ray energy was 11.2 keV and the sample-to-detector distance was determined to be 7230 mm by calibration with a silver behenate standard. Scattering patterns were recorded on a PILATUS 2M detector with a 1 s exposure time at angles of incidence ranging from $\alpha_i = 0.14$ to 0.18°. To avoid damaging the terpolymer film by overexposure to the X-rays, the film was translated laterally by 250 µm prior to each measurement (e.g. after the previous measurement and any alignment protocols).

[3] Scattering experiments were performed by the author, Karolina Korzeb, and Dr. Ilja Gunkel.

3.5.2 Cornell High Energy Synchrotron Source

GISAXS and GIWAXS measurements were performed ex situ at the D1 beamline of the Cornell High Energy Synchrotron Source, Cornell University, New York, USA, at a constant X-ray energy of 10.67 keV (Chap. 5).[4] A Medoptics CCD detector was used to record the scattering images at a typical exposure time of 1–2 s for a single image. The sample to detector distances were calibrated with a silver behenate standard and were 1820 mm (GISAXS) and 102 mm (GIWAXS), respectively.

3.5.3 Data Analysis

GISAXS scattering patterns were reduced using *Nika*, a software package for IGOR Pro 6 (WaveMetrics), and the in-plane line integrations were subsequently analysed using custom software to automatically determine peak locations and widths as a function of swelling ratio (Chap. 4) [3].[5] Peaks were analysed by fitting to the composite function

$$I(q_y) = I_0 + I_1 q_y^{-d} + \sum_{n=1}^{N} \frac{I_{(n)}^{\text{Peak}}}{1 + \left(\dfrac{q_y - q_{y(n)}^{\text{Peak}}}{q_{y(n)}^{\text{Width}}} \right)^2}, \tag{3.2}$$

where I_0, I_1, d, $I_{(n)}^{\text{Peak}}$, and $q_{y(n)}^{\text{Width}}$ were free parameters, and $q_{y(n)}^{\text{Peak}}$ was fixed, during the fitting procedure. Peak positions $q_{y(n)}^{\text{Peak}}$ were therefore found prior to fitting by a peak-finding algorithm; peak widths $q_{y(n)}^{\text{Width}}$ resulted from the fit. Either zero, one ($N = 1$), or two ($N = 2$) Lorentzian peaks were identified during fitting.

3.6 Electrodeposition of Gold

To create gyroid optical metamaterials from triblock terpolymer thin films, the polyisoprene (PI) block of the microphase-separated ISO was degraded by exposure to UV light (VWT International, 254 nm, $\approx 50\,\text{mW}\,\text{cm}^{-2}$ for 2 h) and subsequently removed by immersion of the film in ethanol for 10–15 min (Chaps. 5–7). The voided terpolymer network was replicated into gold by electrodeposition using a potentiostat (Autolab PGSTAT302N) and a commercial plating solution (Metalor ECF60 with 0.5% (v/v) E3 brightener). A three electrode cell was employed with the FTO-coated glass substrate as the working electrode, gold-coated glass as the counter electrode,

[4] Scattering experiments were performed by the author, Xiaoyuan Sheng, and Dr. Alessandro Sepe.
[5] Data reduction was undertaken by Karolina Korzeb and Dr. Ilja Gunkel.

and a saturated calomel reference electrode. A nucleation step (a cyclic voltammetry scan from 0 to −1.2 V and back to 0 V at a rate of 0.05 V s^{-1}) was followed by deposition at a constant potential (−0.8 V) to fill the terpolymer template with gold. After deposition, the remaining PS and PEO blocks were removed by exposure of the thin film to an oxygen plasma (Diener MRC 100 at 100% power for around 10 min). For the thermally-annealed samples used in Chap. 6 only, there is an additional processing step. During electrodeposition, gold is grown both within and atop the polymer template, and the layer of excess bulk gold is cleaved at the interface between the nanostructured and bulk gold using Kapton tape, to ensure a smooth top surface (i.e. low surface roughness). The remaining PS and PEO is then removed as above.

3.7 Optical Characterisation

Terpolymer thin films were characterised by optical microscopy (Chap. 5) and gyroid optical metamaterials by reflection and transmission goniometry (Chaps. 6 and 7).

3.7.1 Optical Microscopy

Birefringence and linear dichroism were observed in both reflection and transmission with a Olympus BX-60 polarising optical microscope (Chap. 5). A programmable hot-stage (Linkam HFS91 with TMS93) was used for crystal melting experiments (Chap. 5).

3.7.2 Reflection Goniometry

Optical characterisation was performed using one of two automated reflection goniometers with fixed illumination optics and moveable detection optics. The sample and detection arm on both goniometers were arranged to measure the specular reflection of the gyroid optical metamaterial (i.e whenever the sample was tilted by a polar angle θ, the detection arm was tilted by an angle 2θ). The first goniometer, used to characterise the multi-domain gyroid optical metamaterials (Chap. 6), employed a QP600-2-SR-BX 600 µm core fibre in the illumination arm, a QP230-2-XSR 230 µm core fibre in the detection arm, and a HPX-2000 Ocean Optics xenon light source. Spectra were recorded at angles of incidence between 15 and 65° in steps of 1°. The second goniometer, which could additionally be rotated around the azimuthal axis and was used to characterise the single-domain gyroid optical metamaterials (Chap. 7), employed a QP50-2-VIS-BX 50 µm core in the illumination arm, a QP600-2-UV-BX 600 µm core fibre in the detection arm, and the same light source. The illumination optics focused the light to a spot approximately 100 µm in

diameter situated within a single domain of the gyroid optical metamaterial, about which the sample was rotated. Specular reflections were recorded at 2° intervals for azimuthal angles between 0 and 180°. Linear polarisers were placed at the output of the illumination optics and at the input of the detection optics of both goniometers, fixed to the illumination and detection arms, respectively. For the first goniometer, these were aligned to produce transverse electric (TE) or transverse magnetic (TM) polarisations of light with respect to the sample. Reflectance spectra were normalised with respect to the reflectance of a silver mirror at each polar angle.

3.7.3 Transmission Goniometry

Further characterisation of the single-domain gyroid optical metamaterials was also performed using a custom-built automated transmission goniometer attached to a BX-51 Olympus optical microscope (Chap. 7).[6] The microscope's built-in transmission light source (infrared filter removed) was used to illuminate an area of the sample encompassing multiple domains of the gyroid optical metamaterial. Light from a spot approximately 100 µm in diameter situated within only a single domain was coupled through a long working distance objective (Olympus LMPLFLN5×) and microscope beam splitter into an optical fibre (QP400-2-SR 400 µm core) connected to a spectrometer (Ocean Optics QE6500). The transmission goniometer allowed the sample to be rotated about the azimuthal axis whilst continuing to collect light from within the same domain. Transmission spectra were normalised with respect to the transmission of the FTO-coated glass substrate without the presence of the gyroid optical metamaterial. Again, linear polarisers were placed both before and after the sample.

3.8 Optical Simulations

Simulations of the gyroid optical metamaterial were performed using *Lumerical* (Lumerical Solution, Inc.), a commercial-grade simulator based on the finite-difference time-domain (FDTD) method.[7] The single gyroid morphology was approximated by the level set equation

$$\sin(\tilde{x})\cos(\tilde{y}) + \sin(\tilde{y})\cos(\tilde{z}) + \sin(\tilde{z})\cos(\tilde{x}) \leq t, \tag{3.3}$$

where $\tilde{x}$, $\tilde{y}$, and $\tilde{z}$ are scaled spatial coordinates such that $\tilde{x} = 2\pi x/a$, $\tilde{y} = 2\pi y/a$, and $\tilde{z} = 2\pi z/a$, where a is the lattice constant of the cubic unit cell (the unit cell size). The threshold parameter t determines the volume fill fraction of the gyroid ϕ

[6] The transmission goniometer was built by Steve Drewitt, University of Cambridge, UK.

[7] Simulations were performed by Dr. Matthias Saba, Imperial College, UK.

described by the above equation, and was set to $t = 3(1/2 - \phi) = -0.6$ to model a 30% fill fraction single gyroid. The unit cell size was set to 65 nm. The gyroid optical metamaterial was modelled as being comprised of gold with a bulk permittivity equal to that measured by Johnson and Christy [4]. Its thickness was set equal to $6\sqrt{2}a$ (i.e. ≈ 551 nm). To take into account the surface roughness of the fabricated gyroid optical metamaterial, the reflectance spectra were modulated [5]

$$R = R_0 \left(\exp\left[-(4\pi\sigma)^2/\lambda^2 \right] + 2^5\pi^4(\sigma/\lambda)^4\alpha^2 \right), \tag{3.4}$$

where R_0 is the simulated reflectance, σ is the root mean square surface roughness (90 nm), λ is wavelength, and α (0.1) is the ratio of m, the root mean square slope of the surface, and $\Delta\theta$, the instrumental acceptance angle (i.e. $\alpha = \Delta\theta/m$).

References

1. Bailey, T. S., Hardy, C. M., Epps, T. H., & Bates, F. S. (2002). A noncubic triply periodic network morphology in poly(isoprene-b-styrene-b-ethylene oxide) triblock copolymers. *Macromolecules*, *35*, 7007–7017.
2. Bailey, T. S., Pham, H. D., & Bates, F. S. (2001). Morphological behavior bridging the symmetric AB and ABC states in the poly(styrene-b-isoprene-b-ethylene oxide) triblock copolymer system. *Macromolecules*, *34*, 6994–7008.
3. Ilavsky, J. (2012). Nika: Software for two-dimensional data reduction. *Journal of Applied Crystallography*, *45*, 324–328.
4. Johnson, P. B., & Christy, R. W. (1972). Optical constants of the noble metals. *Physical Review B*, *6*(12), 4370–4379.
5. Bennett, H. E., & Porteus, J. O. (1961). Relation between surface roughness and specular reflectance at normal incidence. *Journal of the Optical Society of America*, *51*, 123–129.

Part I
Solvent Vapour Annealing of a Gyroid-Forming Triblock Terpolymer

Block copolymer self-assembly is a particularly promising route to fabricate nanostructured materials over macroscopically large areas, such as optical metamaterials. Gyroid optical metamaterials may therefore be fabricated using gyroid-forming polyisoprene-b-polystyrene-b-poly(ethylene oxide) (ISO) triblock terpolymers by replication of the self-assembled three-dimensional morphology into gold. However, the resulting gyroid metamaterials only exhibit their most striking optical properties when the regions of long-range order are sufficiently large, typically on the order of several tens to several hundreds of micrometres. Such long-range order is most readily achieved by solvent vapour annealing (SVA), a process whereby a controlled quantity of solvent vapour is introduced to the terpolymer, lowering its glass transition temperature to below ambient temperature and drastically increasing its mobility. However, whereas both the kinetics and thermodynamics of solvent-annealed sphere-, cylinder-, and lamellae-forming linear diblock copolymers are now well understood, this is not the case for the next most complicated family of linear block copolymers, triblock terpolymers, or indeed network-forming diblocks or triblocks. In this part, we therefore present the results of *in situ* grazing-incidence small-angle X-ray scattering (GISAXS) on a 35 kg mol^{-1} gyroid-forming ISO triblock terpolymer, revealing the kinetics and thermodynamics of the self-assembly of the gyroid morphology during SVA (Chap. 4).

The triblock terpolymer used to fabricate gyroid optical metamaterials is not amorphous but rather amorphous–semicrystalline, and the behaviour of such copolymers is a delicate balance between the driving forces of crystallisation and microphase separation. In this part, we therefore also demonstrate the preferential alignment of poly(ethylene oxide) (PEO) crystallites confined within a single gyroid of a solvent-annealed 80 kg mol^{-1} ISO triblock terpolymer thin film (Chap. 5). The resulting crystalline superstructure is a hitherto unreported and unexpected birefringent texture consisting of domains of uniform birefringence. Moreover, the constituent PEO crystallites exhibit a preferred azimuthal alignment as determined by grazing-incidence wide-angle X-ray scattering (GIWAXS). We hypothesise that the PEO crystallites are preferentially aligned (on average) along the ⟨111⟩ and ⟨100⟩ directions of the gyroid morphology, which are at 35 and 45° to the substrate normal, respectively. These directions were identified previously as those of fastest growth within a gyroid-structured template and here provide the "straightest paths" for PEO crystallisation confined by the continuous glassy PS matrix.

Chapter 4
In Situ GISAXS During Solvent Vapour Annealing of a Gyroid-Forming ISO Triblock Terpolymer

In this chapter, we study the kinetics and thermodynamics of a 35 kg mol^{-1} gyroid-forming polystyrene-*b*-polyisoprene-*b*-poly(ethylene oxide) (ISO) linear triblock terpolymer during solvent vapour annealing (SVA) using grazing-incidence small-angle X-ray scattering (GISAXS). GISAXS is the most direct means by which to study the microphase-separated morphology of a block copolymer in situ during SVA, allowing simultaneous characterisation of both in- and out-of-plane electron density correlations in the film over a macroscopically large area in real time [1–8]. We anneal the terpolymer films in various solvent vapours (chloroform, tetrahydrofuran, and methanol) and their mixed vapours (tetrahydrofuran and methanol) and identify the resulting microphase-separated morphologies and long-range order upon varying the maximum solvent concentration and removal rate. The results provide crucial information regarding the behaviour of gyroid-forming triblock terpolymer thin films when exposed to solvent vapour, and therefore constitute a first step towards rational design of SVA protocols to successfully and reliably achieve large domains of the alternating gyroid morphology for optical metamaterial applications.[1]

4.1 Methods

Details of the methods used may be found in Chap. 3. Briefly, thin films of a 35 kg mol^{-1} ISO triblock terpolymer were spun atop silicon substrates from a 10% (w/w) solution of the terpolymer in anhydrous anisole. Samples were exposed to controlled amounts of solvent vapour using a custom annealing chamber and experimental set-up, which allowed for both simultaneous GISAXS and film thickness

[1]This chapter is based closely on the experimental section of: Dolan, J. A., Korzeb, K., Dehmel, R., Gödel, K. C., Stefik, M., Wiesner, U., Wilkinson, T. D., Baumberg, J. J., Wilts, B. D., Steiner, U., & Gunkel, I. Controlling self-assembly in gyroid terpolymer films by solvent vapor annealing (in press).

© Springer Nature Switzerland AG 2018

J. A. Dolan, *Gyroid Optical Metamaterials*, Springer Theses,
https://doi.org/10.1007/978-3-030-03011-7_4

measurements through side and top windows, respectively. Up to three gas lines could be mixed to control the ratio of saturated to dry gas (i.e. the "concentration" of the solvent vapour in the chamber): one flowing only nitrogen and the other two flowing nitrogen bubbled through a solvent. The terpolymer film thickness was measured interferometrically using a light source and spectrometer. GISAXS measurements were performed in situ at the cSAXS beamline of the Swiss Light Source, Paul Scherrer Institute, Villigen, Switzerland. The resulting scattering patterns were reduced and the in-plane line integrations were analysed to determine peak locations and widths as a function of swelling ratio.[2]

4.2 Results

To study the kinetics and thermodynamics of the ISO triblock terpolymer during SVA, thin films of the terpolymer were exposed to controlled amounts of solvent vapours and the resulting film thickness and GISAXS scattering patterns were recorded at regular intervals. An approach was undertaken whereby the constituent regimes within SVA were first studied by tracking the GISAXS scattering patterns and the associated peak statistics (e.g. positions and widths) as a function of swelling ratio (Sect. 4.2.1). The presence and behaviour of the peaks reveal the effect of the solvent on the microphase-separated morphology during SVA. The insights gained were then used to investigate both the effect of quench regime (i.e. maximum swelling ratio) and quench rate on the microphase-separated morphology and long-range order of the resulting dried films (Sect. 4.2.2). Finally, the effect of different solvent and mixed solvent vapours is similarly studied, whereby the varying selectivity of the solvents to the individual blocks of the terpolymer is investigated (Sect. 4.2.3).

4.2.1 Solvent Vapour Annealing (SVA) Regimes

To gain a first insight into the behaviour of ISO thin films subjected to SVA, and to provide a basis for further exploration of the SVA parameter space, different SVA "regimes" were identified (i.e. swelling ratios between which clear morphological transitions were observed). Figure 4.1 shows the eight such regimes identified during the swelling and deswelling of an ISO thin film in mixed vapours of tetrahydrofuran (THF) and methanol (80:20). As may readily be determined by simple homopolymer dissolution experiments, THF is a good solvent for PS, PI, and PEO, whereas methanol is a good solvent only for PEO (better than THF) and a bad solvent for PS and PI. A mixture of THF and methanol is therefore anticipated to be a good solvent

[2]Scattering experiments were performed by the author, Karolina Korzeb, and Dr. Ilja Gunkel. Data reduction and indexing was undertaken by Karolina Korzeb and Dr. Ilja Gunkel, respectively. Data analysis was undertaken by the author.

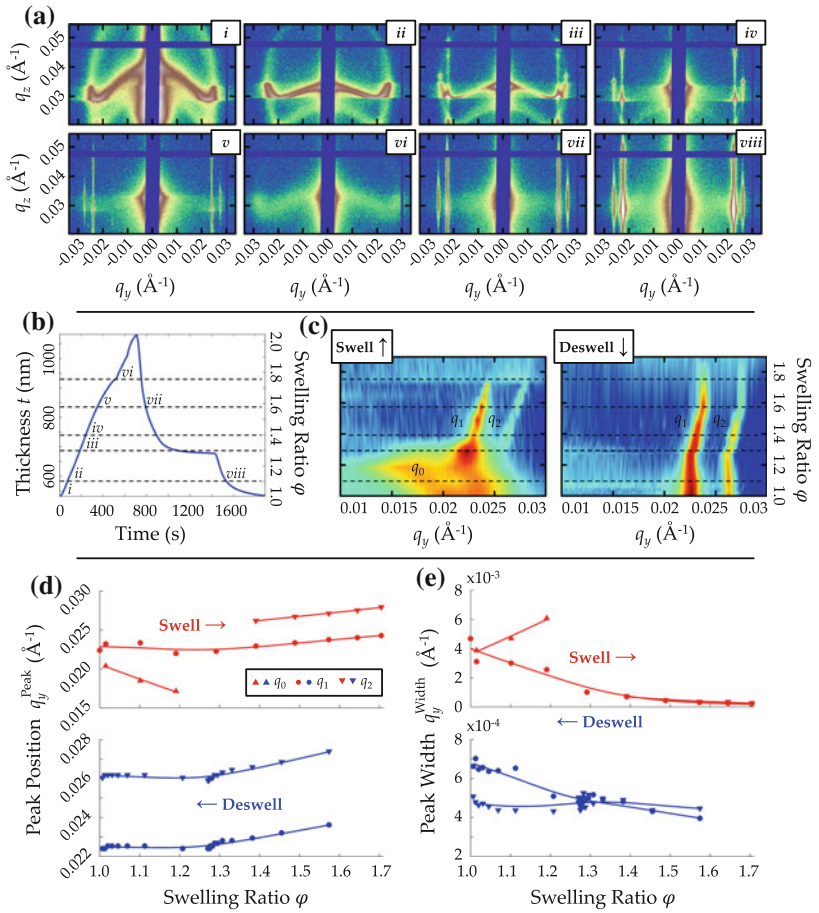

Fig. 4.1 Solvent vapour annealing (SVA) regimes during swelling and deswelling of an ISO thin film. Eight SVA regimes were identified during the swelling and deswelling of an ISO thin film in the mixed vapours of tetrahydrofuran (THF) and methanol (80:20). **a** GISAXS patterns at a fixed angle of incidence ($\alpha_i = 0.18°$) representative of the different SVA regimes. The regimes and corresponding onset swelling ratios (φ) were identified as: *i As-Spun* (1.00); *ii Plasticisation* (1.10); *iii Ordering* (1.29); *iv Order* (1.39); *v Disordering* (1.57); *vi Disorder* (1.74); *vii Re-Ordering* (1.57); and *viii Vitrification* (1.10). Logarithmic colour scales whereby the colour scale of each patterned is normalised to the maximum and minimum intensities of that pattern. **b** Film thickness and swelling ratio as a function of time during the experiment. **c** Swelling and deswelling line integral surfaces. The line integral through the GISAXS pattern at $q_z = 0.03\,\text{Å}^{-1}$ is plotted as a function of swelling ratio. The "peak" due to the diffuse Debye-Scherrer ring (DDSR) of the refracted beam is labelled q_0 and the true first and second order peaks are labelled q_1 and q_2, respectively. Logarithmic colours scales whereby the colour scale is normalised to the maximum and minimum intensities of the complete set of line integrals. **d** Peak positions q_y^{Peak} and **e** widths q_y^{Width} (i.e. full widths at half maximum) of the three peaks at $q_y \lesssim 0.020\,\text{Å}^{-1}$ (q_0; upward triangles), $q_y \approx 0.023\,\text{Å}^{-1}$ (q_1; circles) and $q_y \approx 0.026\,\text{Å}^{-1}$ (q_2; downward triangles) during swelling (red) and deswelling (blue) of the ISO thin films. Peak statistics are calculated from the GISAXS line integrals at $q_z = 0.03\,\text{Å}^{-1}$. Solid lines are guides to the eye

for all blocks of the ISO, an assumption which will be further explored in Sect. 4.2.3. Associated GISAXS patterns (Fig. 4.1a), film thickness (i.e. swelling ratio φ) measurements (Fig. 4.1b), line integral surfaces (Fig. 4.1c), and peak statistics (Fig. 4.1d, e) are presented. The line integral surfaces plot the evolution of a line integral through the GISAXS pattern at the out-of-plane wave vector $q_z = 0.03\,\text{Å}^{-1}$ as a function of swelling ratio. Peak statistics plot the variation in peak positions and widths during swelling and deswelling in the ordered (i.e. microphase-separated) regimes, calculated from the GISAXS line integrals. The peak positions of the two (positive q_y value) peaks at the in-plane wave vectors $q_y \approx 0.023\,\text{Å}^{-1}$ and $\approx 0.026\,\text{Å}^{-1}$, labelled q_1 and q_2, respectively, are plotted in Fig. 4.1d. Also plotted is the position of the "peak" at $q_y \lesssim 0.020\,\text{Å}^{-1}$, labelled q_0, which is associated with the "diffuse Debye-Scherrer ring" (DDSR) of the refracted beam [4]. The corresponding peak widths (i.e. full widths at half maximum) are plotted in Fig. 4.1e. The eight SVA regimes (and their corresponding onset swelling ratios) are identified and interpreted as follows:

i. AS- SPUN: After spin-coating and before application of the solvent vapour ($\varphi = 1.00$), the GISAXS scattering pattern exhibits significant intensity along the entirety of the DDSR, starting at $q_y \approx \pm 0.025\,\text{Å}^{-1}$ and ending at $q_z \approx 0.04\,\text{Å}^{-1}$ (Fig. 4.1a). This high intensity DDSR is attributed to the refracted beam, enhanced by the Yoneda band; the same DDSR from the transmitted and diffracted beams is also visible at lower and higher q_z values, respectively. The DDSR from the refracted (q_0) and diffracted (q_1) beams together appear as two broad peaks in the swelling line integral surface (Fig. 4.1c) and peak statistics (Fig. 4.1d, e).
The as-spun thin film possesses a kinetically-trapped and isotropic microphase-separated morphology with only short-range order.
ii. PLASTICISATION: As the solvent concentration in the film increases ($\varphi \approx 1.10$), the GISAXS pattern begins to change (Fig. 4.1a). The DDSR of the refracted beam shifts to lower q_z values, now ending at $q_z \approx 0.0325\,\text{Å}^{-1}$. This appears as a shift to lower q_y values and a broadening of the first "peak" (q_0) in the swelling line integral surface (Fig. 4.1c) and peak statistics (Fig. 4.1d, e).
The changing GISAXS pattern and swelling line integral surface indicates plasticisation of the film (i.e. a lowering of the glass transition temperature T_g below ambient temperature) and relaxation of the kinetically trapped as-spun morphology.
iii. ORDERING: As the solvent concentration in the film is further increased ($\varphi \approx 1.29$), the GISAXS pattern changes more dramatically (Fig. 4.1a). The DDSR of the refracted beam reduces in intensity and distinct "Bragg reflections" begin to appear in place of the DDSR of the diffracted beam [4]. Similarly, the swelling line integral surface (Fig. 4.1c) and peak statistics (Fig. 4.1d, e) now exhibit only a single peak (q_1) corresponding to the Bragg reflections within the Yoneda band at $q_y \approx \pm 0.0225\,\text{Å}^{-1}$. This peak shifts to a slightly lower q_y value (Fig. 4.1d) and narrows substantially (Fig. 4.1e).

The mobility of the triblock terpolymer has increased to the extent that the film is able to self-assemble towards an ordered microphase-separated morphology.[3]

iv. ORDER: With an increase in solvent concentration ($\varphi \approx 1.39$), the DDSRs of the diffracted and refracted beams completely disappear (Fig. 4.1a). They are replaced by high intensity Bragg reflections at $q_y \approx \pm 0.0225\,\text{Å}^{-1}$ and $\approx \pm 0.0275\,\text{Å}^{-1}$. The swelling line integral surface (Fig. 4.1c) and peak statistics (Fig. 4.1d, e) now exhibit both a high (q_1) and low (q_2) intensity peak corresponding to the Bragg reflections at $q_y \approx \pm 0.0225\,\text{Å}^{-1}$ and $\approx \pm 0.0275\,\text{Å}^{-1}$, respectively. Both peaks increase in q_y value (Fig. 4.1d) and continue to reduce in width (Fig. 4.1e).
The mobility imparted to the triblock terpolymer by the solvent has allowed it to self-assemble into its equilibrium ordered microphase-separated morphology in the presence of the solvent vapour.

v. DISORDERING: As the solvent concentration is increased further ($\varphi \approx 1.57$), the intensity of the Bragg reflections greatly diminishes and only weak "diffuse Bragg rods" are evident at near identical q_y values (Fig. 4.1a) [4]. The peaks in the swelling line integral surface begin to diminish relative to their intensity at lower swelling ratios (Fig. 4.1c). Both peaks continue to increase further in q_y value (Fig. 4.1d) and reduce in width (Fig. 4.1e).
The terpolymer is approaching its order-disorder transition (ODT) and is beginning to disorder.

vi. DISORDER: As the maximum solvent concentration used in the experiment is approached ($\varphi \approx 1.74$), the diffuse Bragg rods disappear and only a very faint DDSR is visible in the GISAXS patterns (Fig. 4.1a). No peak is evident in the swelling line integral surface (Fig. 4.1c) and no peak statistics are therefore generated.
Having crossed its ODT, the terpolymer film is disordered.

vii. RE- ORDERING: As the solvent concentration is decreased ($\varphi \approx 1.57$), the diffuse Bragg rods at $q_y \approx \pm 0.0225\,\text{Å}^{-1}$ and $\approx \pm 0.0275\,\text{Å}^{-1}$ begin to reappear in both the GISAXS pattern (Fig. 4.1a) and the deswelling line integral surface (Fig. 4.1c). The associated peaks reduce in q_y value (Fig. 4.1d) and broaden (Fig. 4.1e).
Once again the film has crossed its ODT and is therefore re-ordering into its equilibrium microphase-separated morphology.

viii. VITRIFICATION: As the solvent concentration is decreased further ($\varphi \approx 1.10$), the diffuse Bragg rods increase in intensity (Fig. 4.1a). The second peak at higher q_y value (q_2) in the deswelling line integral surface therefore increases in prominence (Fig. 4.1c). Both peaks continue to shift to lower and then slightly higher q_y values (Fig. 4.1d), and widen by a relatively small amount compared to the initial peak width in the as-spun film (Fig. 4.1e). The GISAXS pattern, deswelling line

[3] Note that, depending on context, the term "order" is used to describe both the state of microphase-separation and the degree of order of that microphase-separated morphology. Clearly, a copolymer cannot be ordered if not microphase-separated, but it may be both "disordered" and microphase-separated if it possesses only short-range order.

integral surface, and peak statistics do not change any further as remaining solvent is removed.
The glass transition temperature T_g has therefore once again been raised above ambient temperature as the solvent concentration in the film diminishes, and the terpolymer has vitrified.

Although the behaviour of ISO during annealing with different solvent vapours is explored in Sect. 4.2.3, it should be noted that entirely equivalent SVA regimes can be found when ISO films are swollen in other solvents (e.g. chloroform; not shown).

The GISAXS scattering patterns shown in Fig. 4.1a may be indexed to confirm the microphase-separated morphology present in the swollen and dried films. The two prominent peaks (q_1 and q_2) may be indexed as $q_1 = \sqrt{6}q_y^\star$ and $q_2 = \sqrt{8}q_y^\star$, where $q_y^\star$ is the fundamental wave vector. The relative peak positions correspond to those expected for the first two peaks of the Q^{230} core-shell double gyroid morphology with space group $Ia\bar{3}d$, and the second and third peaks of the Q^{214} alternating gyroid morphology with space group $I4_132$ (cf. Fig. 2.7) [9]. However, an additional peak at $q_y = \sqrt{2}q_y^\star$ would be expected for the Q^{214} alternating gyroid morphology, which is absent from the scattering patterns presented here. Despite this unexplained discrepancy, we confidently assign the microphase-separated morphology of the swollen and dried ISO terpolymer films as the alternating gyroid (Q^{214}). Scanning electron microscopy of gold replicas of this and other molecular weight ISO thin films have on no occasion, irrespective of fabrication protocol, exhibited the double gyroid morphology corresponding to the core-shell double gyroid (Q^{230}), yet the GISAXS scattering patterns similar can similarly lack the expected $\sqrt{2}q_y^\star$ peak.

4.2.2 *Effect of Maximum Swelling Ratio and Solvent Removal Rate*

Having identified the various regimes observed during SVA of ISO thin films, the SVA parameter space may now be explored with the goal of capturing the ordered swollen microphase-separated morphology in the dried film. The coupled effect of quenching the film from either the disordered or ordered regimes (i.e. the maximum swelling ratio), and the rate of solvent removal, is therefore explored in Fig. 4.2. Shown in Fig. 4.2 are the film thickness (swelling ratio) profiles and corresponding GISAXS scattering patterns for four terpolymer thin films subjected to various SVA protocols. The solvent vapours used to swell the terpolymer were again a mixture of THF and methanol (80:20).

THE MAXIMUM SWELLING RATIO of two films (red solid and dotted lines; $\varphi_{max} \approx 1.3$) ensured that they remained ordered throughout the entirety of the protocol. The maximum swelling ratios of the other two films (blue solid and dotted

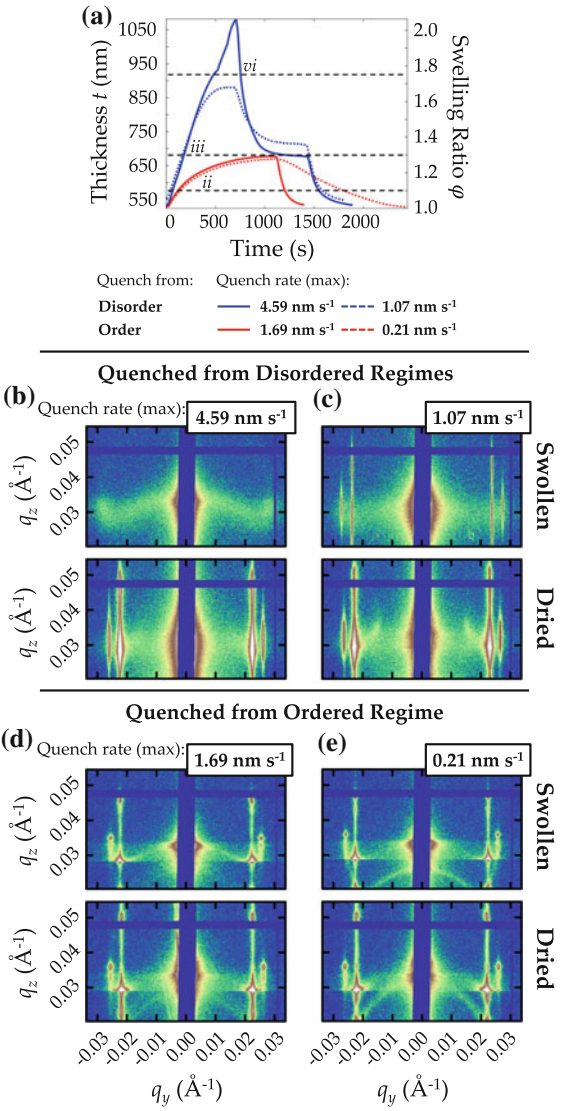

Fig. 4.2 Effect of maximum swelling ratio and solvent removal rate upon the dried film morphology. Film thickness profiles and GISAXS patterns of swollen and dried films subjected to two solvent removal (quench) rates whilst in the disordered and ordered regimes. Films were annealed in mixed vapours of THF and methanol (80:20). **a** Film thickness (swelling ratio) profiles of four films subjected to SVA. Two films were quenched whilst in the disordered (blue solid line) and disordering (blue dotted line) regimes with a maximum solvent removal (quench) rate of 4.59 and 1.07 nm s^{-1}, respectively. The other two films were quenched whilst in the ordered (red solid and dotted lines) regime with a maximum solvent removal rate of 1.69 and 0.21 nm s^{-1}, respectively. GISAXS patterns ($\alpha_i = 0.18°$) of the swollen (top row) and dried (bottom row) films during and after quench from disordered regimes with **b** 4.59 nm s^{-1} and **c** 1.07 nm s^{-1} solvent removal rates, and from ordered regimes with **d** 1.69 nm s^{-1} and **e** 0.21 nm s^{-1} solvent removal rates. Logarithmic colour scales whereby the colour scale of each patterned is normalised to the maximum and minimum intensities of that pattern

lines; $\varphi_{max} \approx 2.0$ and 1.6,[4] respectively) ensured that the films were disordered (i.e. disordered or in the process of disordering) upon quench. This behaviour can be seen in Fig. 4.3, which presents the swelling and deswelling line integral surfaces for the films quenched from the disordered (Fig. 4.3a, b) and ordered (Fig. 4.3c, d) regimes. Whereas the ordered peaks (q_1 and q_2; cf. Figure 4.1c) in the swelling line integral surface disappear for the film swollen to $\varphi_{max} \approx 2.0$ (Fig. 4.3a), they remain throughout in the swelling line integral surfaces for both the film swollen to $\varphi_{max} \approx 1.6$ (Fig. 4.3b) and the two films swollen to $\varphi_{max} \approx 1.3$ (Fig. 4.3c, d). The resulting GISAXS patterns of the swollen and dried films can be seen in Fig. 4.2b–e. It is clear that the two patterns corresponding to the dried films quenched from the disordered regimes (Fig. 4.2b, c) are qualitatively different from the two patterns corresponding to the dried films quenched from the ordered regimes (Fig. 4.2d, e). Whereas the former exhibit only diffuse Bragg rods at $q_y \approx \pm 0.023\,\text{Å}^{-1}$ and $\approx \pm 0.026\,\text{Å}^{-1}$, the latter exhibit highly distinct Bragg reflections at the same q_y values. Furthermore, when the peak statistics are analysed quantitatively (Table 4.1 and Fig. 4.4), it becomes apparent that the peaks in the films which were quenched from the disordered regimes (Fig. 4.4a, b, top row) are positioned at slightly higher q_y values than those in the films quenched from the ordered regimes (Fig. 4.4c, d, top row). Similarly, the peaks for those films quenched from the disordered regimes (Fig. 4.4a, b, bottom row) are generally narrower than those for films quenched from the ordered regimes (Fig. 4.4c, d, bottom row).

THE SOLVENT REMOVAL RATE during quench is also a key parameter in SVA, and each of the films presented in Fig. 4.2 was subjected to a different solvent removal (quench) rate. Notwithstanding the different maximum swelling ratio of the two films quenched from the disordered regimes, the resulting GISAXS patterns (Fig. 4.2b, c) and deswelling line integral surfaces (Fig. 4.3a, b) look qualitatively similar irrespective of quench rate. Indeed, the peak locations (Table 4.1 and Fig. 4.4a, b, top row) are also quantitatively similar. However, when the peak widths are analysed, it becomes clear that those associated with the $4.59\,\text{nm}\,\text{s}^{-1}$ maximum quench rate (Fig. 4.4a, bottom row) are slightly smaller than those associated with the $1.07\,\text{nm}\,\text{s}^{-1}$ maximum quench rate (Fig. 4.4b, bottom row). The GISAXS patterns (Fig. 4.2d, e) and deswelling line integral surfaces (Fig. 4.3c, d) corresponding to the two films quenched from the ordered regimes, which were both swollen to the same maximum swelling ratio, are also qualitatively similar irrespective of quench rate, and their peak positions quantitatively similar (Table 4.1 and Fig. 4.3c, d, top row). However, we this time find from an analysis of the peak widths that those associated with the $1.69\,\text{nm}\,\text{s}^{-1}$ maximum quench rate (Fig. 4.4c, bottom row) are broadly similar to those associated with the $0.21\,\text{nm}\,\text{s}^{-1}$ maximum quench rate (Fig. 4.4d, bottom row), with the width of one peak seemingly increasing and the other decreasing. Note that the significant variation in the calculated peak widths for the $0.21\,\text{nm}\,\text{s}^{-1}$ maximum quench rate (Fig. 4.4d, bottom row) complicates this analysis somewhat. Finally, the similarity between the GISAXS patterns in the swollen and dried states

[4]Note that this swelling ratio is slightly lower than it appears in Fig. 4.2(a) due to the larger initial thickness of the corresponding film.

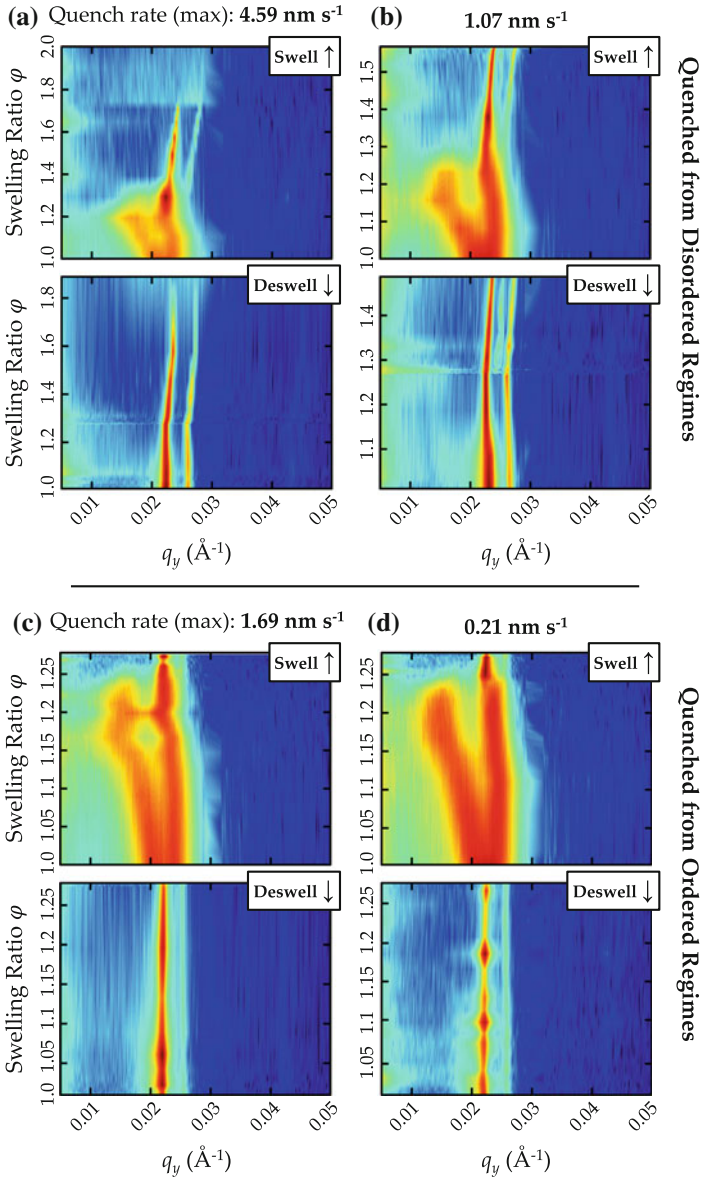

Fig. 4.3 Line integral surfaces of ISO thin films quenched from disordered and ordered regimes at different quench rates. Swelling and deswelling line integral surfaces for ISO thin films which were in **a** and **b** disordered, and **c** and **d** ordered, regimes prior to quenching. Films were annealed in mixed vapours of THF and methanol (80:20). The films quenched from the disordered regimes exhibited a maximum solvent removal (quench) rate of **a** 4.59 nm s^{-1} and **b** 1.07 nm s^{-1}. The films quenched from the order regimes exhibited a maximum quench rate of **c** 0.21 nm s^{-1} and **d** 1.69 nm s^{-1}. The line integral through the GISAXS pattern at $q_z = 0.03$ Å^{-1} is plotted as a function of swelling ratio. Logarithmic colour scales are normalised to the maximum and minimum intensities of the complete set of line integrals

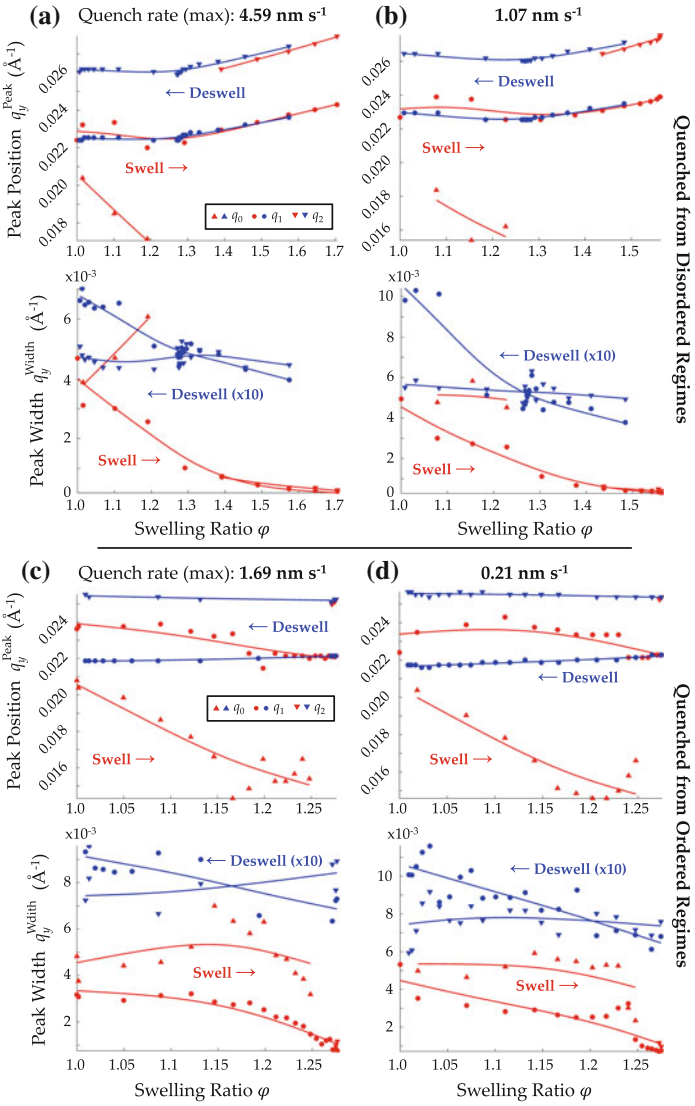

Fig. 4.4 Peak positions and widths during swelling and deswelling of ISO thin films quenched from disordered and ordered regimes at different quench rates. Peak positions and widths during swelling and deswelling in mixed vapours of THF and methanol (80:20) of four ISO thin films. Peak statistics are calculated from the GISAXS line integrals at $q_z = 0.03\,\text{Å}^{-1}$. Peak positions and widths (i.e. full widths at half maximum) of the three peaks at $q_y \lesssim 0.020\,\text{Å}^{-1}$ (q_0; downward triangles), $q_y \approx 0.023\,\text{Å}^{-1}$ (q_1; circles), and $q_y \approx 0.026\,\text{Å}^{-1}$ (q_2; upward triangles) during swelling (red) and deswelling (blue) for films which are quenched from **a** and **b** disordered, and **c** and **d** ordered, regimes. The films quenched from the disordered regimes exhibited a maximum solvent removal (quench) rate of **a** $4.59\,\text{nm}\,\text{s}^{-1}$ and **b** $1.07\,\text{nm}\,\text{s}^{-1}$. The films quenched from the order regimes exhibited a maximum quench rate of **c** $0.21\,\text{nm}\,\text{s}^{-1}$ and **d** $1.69\,\text{nm}\,\text{s}^{-1}$. Peak widths during deswelling (blue) are plotted an order of magnitude larger than calculated. Solid lines are guides to the eye

Table 4.1 Resulting peak statistics (i.e. postions and full widths at half maximum) corresponding to the dried film morphologies for ISO thin films annealed in the mixed vapours of THF and methanol (80:20) and quenched from the disordered and ordered regimes

Quench from:	Disorder		Order	
Quench rate ($\mathrm{nm\,s^{-1}}$):	4.59	1.07	1.69	0.21
$q_{y(1)}^{\mathrm{Peak}}$ ($\mathrm{\AA^{-1}}$)	0.0225	0.0230	0.0219	0.0217
$q_{y(2)}^{\mathrm{Peak}}$ ($\mathrm{\AA^{-1}}$)	0.0261	0.0265	0.0254	0.0256
$q_{y(1)}^{\mathrm{Width}}$ ($\times 10^{-3}\,\mathrm{\AA^{-1}}$)	0.67	1.0	0.92	1.0
$q_{y(2)}^{\mathrm{Width}}$ ($\times 10^{-3}\,\mathrm{\AA^{-1}}$)	0.48	0.56	0.74	0.64

after quenching from the ordered regimes, apart from a pronounced shift to lower q_z values of the Bragg reflections at $q_y \approx \pm 0.023\,\mathrm{\AA^{-1}}$, should also be noted.

4.2.3 Effect of Different Solvent and Mixed Solvent Vapours

As well as maximum swelling ratio and quench rate, another crucial SVA parameter which may affect both the microphase-separated morphology and its long-range order is the selectivity of the solvent vapours. The SVA experiments presented in Sects. 4.2.1 and 4.2.2 were all performed using the mixed solvent vapours of THF and methanol (80:20). However, different solvents are anticipated to exhibit a different selectivity to each of the three blocks of the ISO triblock terpolymer, which may lead to a morphological transition in the terpolymer film. The effect of annealing in different solvent and mixed solvent vapours on the swollen and dried microphase-separated morphologies is therefore investigated in Fig. 4.5.

Figure 4.5a–f show the GISAXS patterns for swollen (top row) and dried (bottom row) ISO thin films annealed in a range of solvent and mixed solvent vapours; the corresponding swelling (top row) and deswelling (bottom row) line integral surfaces are shown in Fig. 4.6. As can be seen in Table 4.2 and Fig. 4.6b–e, each of the GISAXS patterns are the result of an annealing protocol which was quenched from the ordered regime (maximum swelling ratio $\varphi_{\mathrm{max}} \approx 1.24 - 1.37$). The only exception is the film which was annealed in THF (Fig. 4.6a), which was quenched from the disordering regime ($\varphi_{\mathrm{max}} \approx 1.53$). Note that the angle of incidence for the GISAXS measurements was $\alpha_{\mathrm{i}} = 0.18°$ for all films other than that annealed in chloroform (Fig. 4.5f), for which the angle of incidence was 0.14°. Notwithstanding the quench from disorder and the differing angle of incidence for the films annealed in THF and chloroform, respectively, the dried GISAXS patterns for all films look qualitatively similar, with the notable exception of the film annealed in methanol (Fig. 4.5e). This film did not swell sufficiently to plasticise and both the "swollen" and dried GISAXS

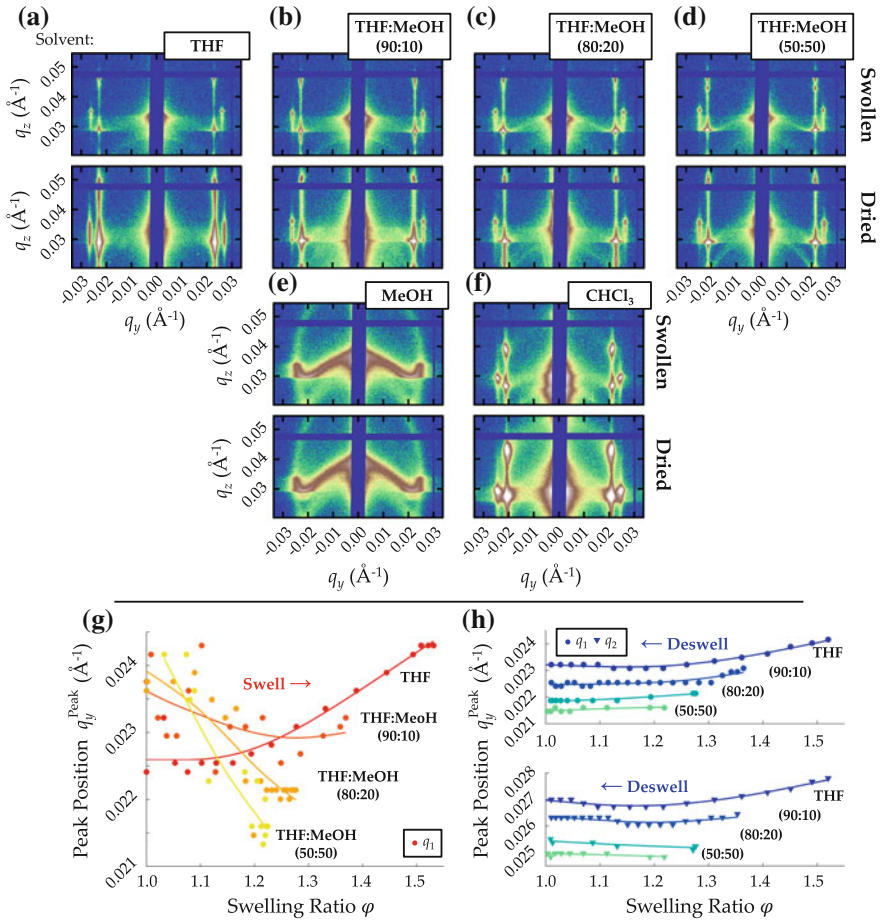

Fig. 4.5 Effect of different solvents on the morphology of swollen and dried ISO thin films. GISAXS patterns investigating the effect of different solvent and mixed solvent vapours on the swollen and dried microphase-separated morphologies of ISO thin films quenched from the **a** disordering and **b**–**d** and **f** ordered regimes (cf. Fig. 4.1); the film annealed in **e** methanol did not plasticise. Solvent and mixed solvent vapours used to anneal the films were **a** THF, **b** a mixture of THF and methanol (THF:MeOH) (90:10), **c** THF:MeOH (80:20), **d** THF:MeOH (50:50), **e** methanol (MeOH), and **f** chloroform ($CHCl_3$). Angles of incidence **a**–**e** $\alpha_i = 0.18°$ and **f** 0.14°. Logarithmic colour scales whereby the colour scale of each patterned is normalised to the maximum and minimum intensities of that pattern. Peak positions q_y^{Peak} during **g** swelling and **h** deswelling of the two peaks at $q_y \approx 0.023\,\text{Å}^{-1}$ (q_1; circles) and $q_y \approx 0.026\,\text{Å}^{-1}$ (q_2; downward triangles) of the ISO thin films annealed in THF and the three THF and methanol mixtures. Peak statistics are calculated from the GISAXS line integrals at $q_z = 0.03\,\text{Å}^{-1}$

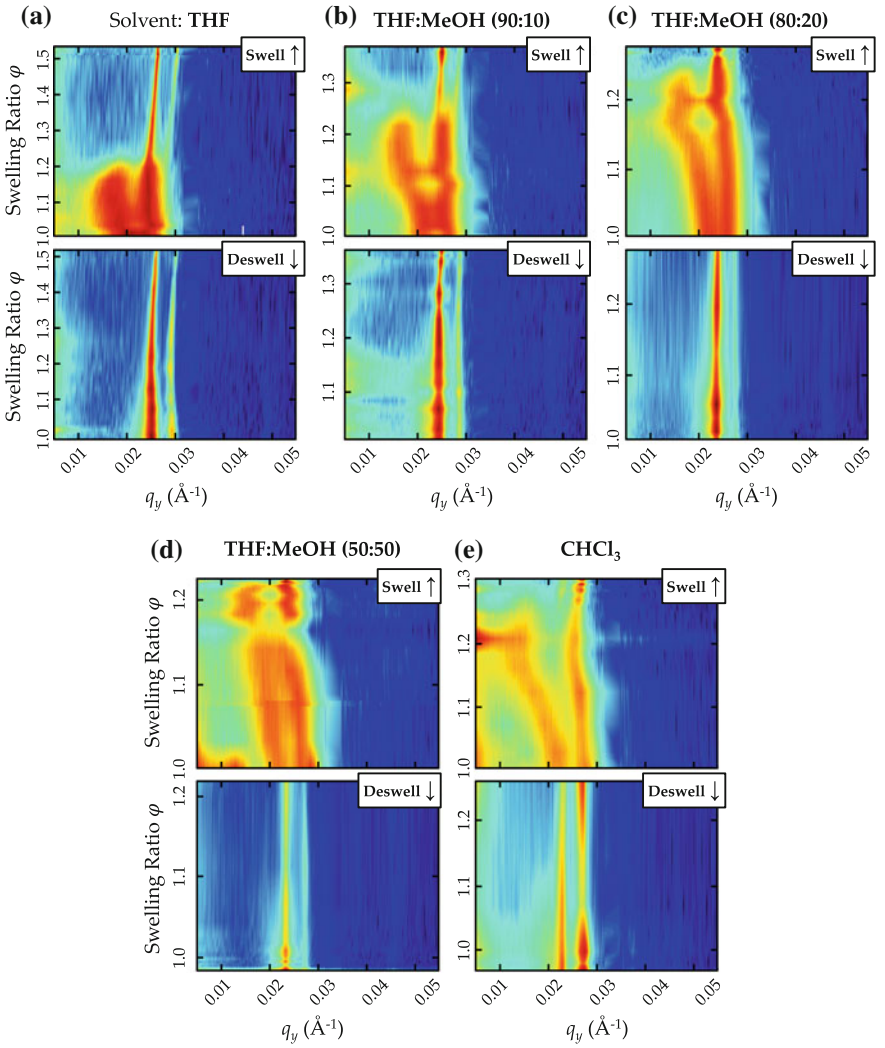

Fig. 4.6 Line integral surfaces of ISO thin films annealed in different solvent and mixed solvent vapours. Swelling and deswelling line integral surfaces for ISO thin films which were annealed in the vapours of **a** THF, **b** a mixture of THF and methanol (THF:MeOH) (90:10), **c** THF:MeOH (80:20), **d** THF:MeOH (50:50), and **e** chloroform ($CHCl_3$). The line integral through the GISAXS pattern at $q_z = 0.03\,\text{Å}^{-1}$ is plotted as a function of swelling ratio. Logarithmic colour scales are normalised to the maximum and minimum intensities of the complete set of line integrals

Table 4.2 Maximum swelling ratio (φ_{max}), approximate swelling ratio of the ordering regime (φ_{iii}), maximum swell rate, and maximum quench rate for the films annealed in THF, three THF and methanol mixtures (THF:MeOH), and chloroform ($CHCl_3$)

Solvent	φ_{max}	φ_{iii}	Swell rate ($nm\,s^{-1}$)	Quench rate ($nm\,s^{-1}$)
THF	1.53	1.28	1.11	0.99
THF:MeOH (90:10)	1.37	1.28	0.75	0.45
THF:MeOH (80:20)	1.28	1.27	0.63	0.69
THF:MeOH (50:50)	1.24	1.22	0.77	1.32
$CHCl_3$	1.32	1.28	0.73	1.71

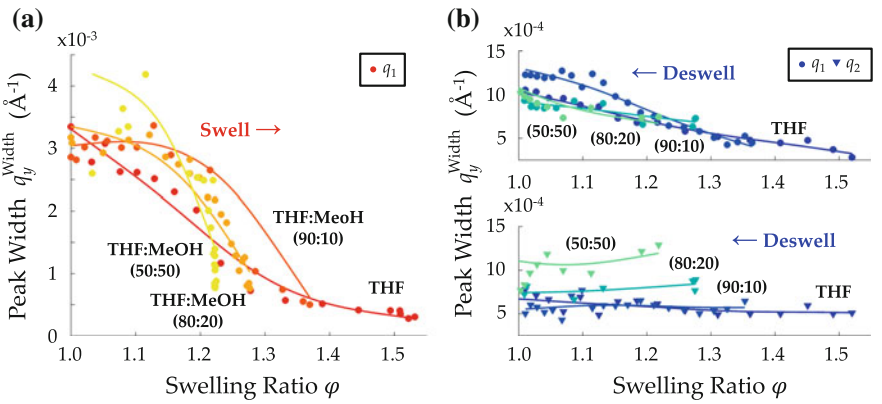

Fig. 4.7 Effect of solvent on the GISAXS peak widths of ISO thin films during swelling and deswelling. Peak widths q_y^{Width} during **a** swelling and **b** deswelling of the two peaks at $q_y \approx 0.023\,Å^{-1}$ (q_1; circles) and $q_y \approx 0.026\,Å^{-1}$ (q_2; downward triangles) of ISO thin films annealed in THF and the three THF and methanol mixtures: THF and methanol (THF:MeOH) (90:10), THF:MeOH (80:20), and THF:MeOH (50:50). Peak statistics are calculated from the GISAXS line integrals at $q_z = 0.03\,Å^{-1}$

patterns are reminiscent of the as-spun regime (cf. Fig. 4.1a). The corresponding line integral surfaces and peak statistics are therefore not shown. Otherwise, all films exhibit the usual Bragg reflections at $q_y \approx \pm 0.0225\,Å^{-1}$ and $\approx \pm 0.0275\,Å^{-1}$ in both the swollen and dried states, although these have broadened into Bragg rods at the same q_y values for the film annealed in THF. Clearly the vapours of THF and chloroform, and the mixed vapours of THF and methanol, unlike the vapours of methanol, are all capable of lowering sufficiently the glass transition temperature T_g of the films to allow them to self-assemble (i.e. order) into their equilibrium microphase-separated morphology.

The lowest swelling ratio (φ_{iii}) at which the peak at $q_y \lesssim 0.020\,\text{Å}^{-1}$ (q_0; cf. Fig. 4.1c) disappears for each of the swelling line integral surfaces in Fig. 4.6 is given in Table 4.2. Based on this approximate metric for the swelling ratio of the ordering regime, it does not appear as if any of the solvent or mixed solvent vapours investigated have a strong effect upon the relationship between swelling ratio and SVA regime. However, a quantitative analysis of the peak positions and widths during swelling and deswelling for the films which ordered does suggest a possible trend (Figs. 4.5g, h and 4.7).

Considering the series THF, THF:MeOH (90:10), THF:MeOH (80:20), and THF:MeOH (50:50), it appears as if the peak positions of both the swollen and dried peaks at $q_y \approx 0.023\,\text{Å}^{-1}$ (q_1) and $\approx 0.026\,\text{Å}^{-1}$ (q_2) decrease in q_y value as the proportion of THF in the mixture of solvent vapours is reduced (Fig. 4.5h). Of course, the maximum swelling ratio of each film in this series also decreases as the proportion of THF in the mixture is reduced, which may contribute to the observed trend (cf. Sect. 4.2.2). However, the potential effect of sample history is minimised by considering the peak positions during swelling from the as-spun regime (Fig. 4.5g). The peak positions now exhibit a clear trend whereby the initial gradient of peak position $q_{y(1)}^{\text{Peak}}$ with respect to swelling ratio (i.e. $\mathrm{d}q_{y(1)}^{\text{Peak}}/\mathrm{d}\varphi$) decreases as the proportion of THF in the mixture of solvent vapours is reduced. Indeed, this gradient is positive for the film annealed in THF (i.e. the peak position increases in q_y value with increasing swelling ratio) and is negative for those annealed films in the mixed vapours of THF and methanol (i.e. the peak position decreases in q_y value). The position of the peak at $q_y \approx 0.026\,\text{Å}^{-1}$ (q_2) is not investigated during swelling as it is not present at low swelling ratios (cf. Fig. 4.1).

A similar trend is also evident in the associated peak widths, whereby the peak at $q_y \approx 0.023\,\text{Å}^{-1}$ (q_1) narrows more rapidly as the swelling ratio is increased for films annealed in mixed solvent vapours with a lower THF content (Fig. 4.7a). Upon deswelling, this trend is no longer clearly evident (Fig. 4.7b, top row). However, it would appear that the peak at $q_y \approx 0.026\,\text{Å}^{-1}$ (q_2) is now wider for films annealed in mixed solvent vapours with a lower THF content. Note that unlike the maximum swelling ratio, the maximum swell rate and quench rate of each of the films do not vary monotonically with the proportion of THF in the mixture of solvent vapours (Table 4.2).

4.3 Discussion

The thermodynamics and kinetics of solvent-annealed $35\,\text{kg}\,\text{mol}^{-1}$ ISO thin films were studied under a variety of conditions.[5] Eight SVA regimes were identified when an ISO thin film was annealed in the mixed vapours of THF and methanol

[5]Note that an $80\,\text{kg}\,\text{mol}^{-1}$ ISO terpolymer with near identical block volume fractions is used in Chaps. 5–7. The lower molecule weight terpolymer was studied here as it provides more distinct GISAXS scattering patterns.

(80:20) (Fig. 4.1). As the solvent concentration increased, the film plasticised and self-assembled towards its equilibrium microphase-separated morphology. During swelling, the peaks in the GISAXS patterns shifted first to lower and then higher q_y values, and narrowed significantly. The ordered morphology was largely maintained upon deswelling. However, the dried peak positions, peak widths, and out-of-plane (q_z) order were significantly affected by the regime (i.e. the maximum swelling ratio) from which the film was quenched and, to a lesser extent, the rate at which the solvent was removed (Fig. 4.2). Finally, the composition of the mixed solvent vapours used to anneal the film was seen to have a pronounced effect on the variation of peak positions and widths as a function of swelling ratio during swelling, although not on the swollen and dried microphase-separated morphologies (Fig. 4.5). Similar variations during deswelling may at least partly be accounted for by differing maximum swelling ratios.

4.3.1 Alternating Gyroid Morphology

Identification of the microphase-separated morphology of the swollen and dried ISO thin films as the alternating gyroid (Q^{214}) allows reinterpretation of the changes undergone by the film during the various SVA regimes in this context (Fig. 4.1). The as-spun film initially exhibits a kinetically-trapped isotropic microphase-separated morphology with only short-range order [10]. Upon plasticisation, the film is able to self-assemble towards the alternating gyroid morphology. Due to the relative strength of the three Flory–Huggins interaction parameters, whereby $\chi_{IO} > \chi_{IS} \approx \chi_{SO}$, ISO forms an alternating gyroid in which the PI and PEO form the two interpenetrating single gyroid networks and the PS forms the continuous matrix separating the PI and PEO (cf. Chap. 2 and Fig. 2.7) [11]. It is therefore the glassy PS matrix which plasticises to allow self-assembly; the PI and PEO are rubbery and semicrystalline at room temperature, respectively [11]. As the solvent concentration in the film increases, the long-range order of the alternating gyroid morphology improves (i.e. the peak widths decrease), both in- and out-of-plane. At the same time, the gyroid unit cell size first increases and subsequently decreases (i.e. the peak positions shift to lower and higher q_y values) as the swelling ratio is increased. This eventual decrease points to an overall reduction in the three Flory-Huggins interaction parameters, χ_{IS}, χ_{SO}, and χ_{IO}, at high swelling ratios, and therefore a reduction in the net segregation strength of the terpolymer.[6] As the solvent concentration is increased further, the order of the alternating gyroid morphology begins to deteriorate in the out-of-plane (q_z) direction; the in-plane order appears to remain. It is unclear whether this apparent disordering in the out-of-plane direction before the loss of in-plane order is perhaps indicative of a potential morphological transition or merely the progress of the disordering solvent front in the film. Upon deswelling, the alternating gyroid morphology reappears and

[6]Of course, we can only speak of the overall reduction in the three Flory-Huggins interaction parameters and cannot identify which of the three individually increase or decrease.

the unit cell size once again increases, and then decreases slightly, until vitrification of the film. Although significantly improved compared to the as-spun film, the long-range order of the dried film is worse than that of the swollen film, both in- and out-of-plane.

The alternating gyroid morphology of the swollen film can be better captured upon solvent removal if quenched from the ordered regime, whereby both the in- and out-of-plane order can be very well preserved (Fig. 4.2). The relatively poor out-of-plane order of the films quenched from the disordered regimes cannot be attributed to the solvent removal (quench) rate: the effect persists irrespective of quench rate (4.59 and $1.07\,\mathrm{nm\,s^{-1}}$) and is not replicated for films quenched from the ordered regimes at an intermediate rate ($1.69\,\mathrm{nm\,s^{-1}}$). Although the unit cell size of the alternating gyroid morphology is smaller for those films quenched from the disordered than the ordered regime, the unit cell size seems similarly insensitive to quench rate when quenching from each of those regimes. Instead, the quench rate would appear to affect the in-plane order of films quenched from the disordered regime, whereby the films quenched more quickly exhibit improved order. However, the differing maximum swelling ratios of the two films quenched from the disordered regimes ($\varphi_{\mathrm{max}} \approx 2.0$ and 1.6 for the films quenched at 4.59 and $1.07\,\mathrm{nm\,s^{-1}}$, respectively) could similarly explain this result. Indeed, that this effect was not also found in the films quenched from the ordered regime, albeit with only relatively modest quench rates (1.69 and $0.21\,\mathrm{nm\,s^{-1}}$), corroborates this conclusion. It is therefore likely, within the range of quench rates explored, that it is the maximum swelling ratio and not the quench rate which primarily determines the degree of in- and out-of-plane order (and indeed unit cell size) of the annealed films.

As mentioned, the improved in-plane order for films quenched from the disordered regimes can be attributed to the monotonic decrease in peak width with increasing solvent concentration in the film. The deterioration in out-of-plane order upon quench for those same films can be attributed to the significant volume change and contraction of the film upon solvent removal. There therefore exists a clear compromise when designing SVA protocols to achieve the desired long-range order: the high swelling ratios required for optimal in-plane order are also those most likely to lead to a deterioration of the out-of-plane order upon quench. Of course, the results presented here cover only a limited range of potential quench rates. An extremely rapid quench may more successfully "lock in" the swollen morphology. Alternatively, an extremely slow quench may allow the film to remain in equilibrium throughout removal of the solvent and therefore provide sufficient time for reorganisation of the film to better accommodate the necessary volume change.

4.3.2 Robust Morphology and Flexible Unit Cell Size

Thin films of ISO were annealed in the vapours of chloroform, THF, methanol, and three mixtures of THF and methanol of varying composition. Whereas the film readily plasticised when annealed in chloroform, THF, and the three THF and methanol

mixtures, it did not plasticise when annealed in methanol alone. As it is the glass transition temperature T_g of the glassy PS matrix which must be lowered to below ambient temperature for the film to plasticise, this observation corroborates the assertion that methanol is not a good solvent for PS. Assuming that sufficient quantity of a good solvent for PS is present in any mixed solvent vapours, it may therefore be possible that a morphological transition is induced by the preferential swelling of one or more blocks of the terpolymer [6]. However, this does not appear to be the case here. Instead, the morphology of both the swollen and dried films can confidently be identified as the alternating gyroid (Q^{214}) irrespective of the solvent or mixed solvent vapours used to successfully anneal the film. It is hypothesised that this is due to the large region of phase space occupied by the alternating gyroid morphology in ABC triblock terpolymers, in sharp contrast to the small and narrow region of phase space occupied by the double gyroid morphology in AB diblock copolymers (cf. Figs. 2.5 and 2.6) [12, 13].

If there is a correlation between the solvent or mixed solvent vapours used and the SVA regimes previously identified, then this is subtle. The lowest swelling ratio at which the peak at $q_y \lesssim 0.020\,\text{Å}^{-1}$ disappears is similar for each of the films swollen in the various solvent and mixed solvent vapours. This is perhaps unsurprising as the film cannot swell appreciably until the majority PS is plasticised and, upon plasticisation, the degree to which the minority PEO is additionally swollen is likely to make only a small contribution to the overall swelling ratio. However, the slightly larger minimum swelling ratio at which the peak at $q_y \lesssim 0.020\,\text{Å}^{-1}$ disappears for films annealed in THF and chloroform ($\varphi \approx 1.28$) compared to films annealed in THF:MeOH (50:50) ($\varphi \approx 1.22$) perhaps also points to the need to sufficiently solvate all blocks of the terpolymer for successful plasticisation.

A more prominent effect of the solvent or mixed solvent vapours used to anneal the ISO triblock terpolymer thin films is the variation in unit cell size and in-plane order (Fig. 4.2). Previously, it was noted that the unit cell size of the alternating gyroid morphology first increased slightly, and then decreased, during swelling in the mixed vapours of THF and methanol (80:20). However, the existence and rate of the initial increase in unit cell size during swelling appears sensitive to solvent selectivity. Unlike those films annealed in the mixed vapours of THF and methanol, the film annealed in THF did not exhibit this initial increase in unit cell size. As the THF content in the mixed vapours of THF and methanol was reduced, there was an increasingly rapid decrease in unit cell size with swelling ratio. This effect cannot be attributed to the swelling rate of the film as, unlike the maximum swelling ratio, these do not vary monotonically with the THF content in the mixed solvent vapours (Table 4.2). Considering also the peak widths during swelling, it appears as if those films annealed in mixed solvent vapours with a lower THF content order more rapidly as a function of swelling ratio. Again, this effect cannot directly be attributed to the swelling rate of the film, although the significant change in peak width at very similar swelling ratios, especially for the film annealed in THF:MeOH (80:20), may indicate some other kinetic factor. It should be noted that there is some spread in peak positions of the films even before swelling ($\varphi = 1.00$) which, given the reproducibility of the spin-coating process, is somewhat unexpected. However,

this spread may be at least partly explained by the occasional unintentional exposure of the films to the solvent vapours in advance of the start of the experiment, despite the author's best efforts to the contrary.

There is a similarly pronounced effect of the solvent or mixed solvent vapours on the peak positions (i.e. unit cell size) during deswelling. As the THF content in the mixed vapours of THF and methanol reduces, the peak positions shift to lower q_y values. This cannot be attributed to quench rate, which does not vary monotonically with the THF content in the mixed vapours. However, the maximum swelling ratio of each of the films does decrease monotonically with the THF content in the mixed vapours, and the unit cell size of the dried film has already been shown to be sensitive to the the maximum swelling ratio. It is therefore likely that the maximum swelling ratio of the swollen film at least partly contributes to the observed change in unit cell size as a function of solvent selectivity during deswelling. Certainly the observed variation in peak widths (i.e. in-plane order) during deswelling is entirely consistent with what might be expected from films swollen to different maximum swelling ratios and cannot readily be decoupled from any potential effect of solvent selectivity.

Collectively, the results point to the simultaneous robustness of the alternating gyroid morphology and the flexibility of its unit cell size during SVA. Irrespective of the type of solvent or mixed solvent vapours used to anneal the films, the morphology remained as the alternating gyroid. Instead, the selectivity of the solvent and maximum swelling ratio could be used to either increase or decrease the unit cell size of the alternating gyroid, and improve the degree of in- and out-of-plane order observed in the resulting dried films.

4.4 Conclusion

In this chapter, we have demonstrated the solvent annealing of a $35\,\mathrm{kg\,mol^{-1}}$ gyroid-forming triblock terpolymer. The SVA regimes of a film annealed in the mixed vapours of THF and methanol (80:20) were identified and the results extended to all solvents and mixed solvent vapours investigated, with the exception of methanol, which did not plasticise the films. The effect of quench regime (i.e. maximum swelling ratio), quench rate, and solvent selectivity were investigated. Whereas the maximum swelling ratio of the swollen film and the solvent selectivity were seen to have a substantial effect on the unit cell size and order (both in- and out-of-plane) of the film, the quench rate was generally observed to have a limited effect, if any, over the range explored.

These results constitute the first step towards rational design of SVA protocols for the successful fabrication of large domains of the alternating gyroid morphology in triblock terpolymers for optical metamaterial applications. The robustness of the alternating gyroid morphology during SVA is of great benefit as it ensures the desired morphology is accessed irrespective of SVA protocol (within the region of parameter space explored above). The selection of the maximum swelling ratio and mixture of solvent vapours also allows fine control over the unit cell size and, therefore,

the optical properties of the resulting optical metamaterials, without the need to synthesise multiple terpolymers of differing molecular weight (cf. Table 2.1). Of course, it remains to be seen whether an appropriate combination of SVA parameters can be found to enable self-assembly of alternating gyroid domains with the required long-range order (i.e. hundreds of micrometres). The results presented in this chapter imply that the desired SVA protocol would have to swell the film to a large maximum swelling ratio and then quench the film extremely slowly to avoid the deterioration of out-of-plane order otherwise associated with quenching from the disordered regimes. However, the forthcoming results on a 80 kg mol^{-1} ISO triblock terpolymer, annealed using a different and less controlled experimental set-up, without the prior benefit of the above knowledge, will indeed show that such protocols are possible, if not yet highly reproducible.

References

1. Gu, X., Gunkel, I., Hexemer, A., Gu, W., & Russell, T. P. (2014). An in situ grazing incidence X-ray scattering study of block copolymer thin films during solvent vapor annealing. *Advanced Materials*, *26*, 273–281.
2. Shelton, C. K., & Epps, T. H. (2016). Block copolymer thin films: Characterizing nanostructure evolution with in situ X-ray and neutron scattering. *Polymer*, *105*, 545–561.
3. Paik, M. Y., Bosworth, J. K., Smilges, D.-M., Schwartz, E. L., Andre, X., & Ober, C. K. (2010). Reversible morphology control in block copolymer films via solvent vapor processing: An in situ GISAXS study. *Macromolecules*, *43*, 4253–4260.
4. Di, Z., Posselt, D., Smilgies, D. M., & Papadakis, C. M. (2010). Structural rearrangements in a lamellar diblock copolymer thin film during treatment with saturated solvent vapor. *Macromolecules*, *43*, 418–427.
5. Di, Z., Posselt, D., Smilgies, D. M., Li, R., Rauscher, M., Potemkin, I. I., et al. (2012). Stepwise swelling of a thin film of lamellae-forming poly(styrene-b-butadiene) in cyclohexane vapor. *Macromolecules*, *45*, 5185–5195.
6. Chavis, M. A., Smilgies, D. M., Wiesner, U. B., & Ober, C. K. (2015). Widely tunable morphologies in block copolymer thin films through solvent vapor annealing using mixtures of selective solvents. *Advanced Functional Materials*, *25*, 3057–3065.
7. Shelton, C. K. (2016). Block copolymer thin films: Characterizing nanostructure evolution with in situ X-ray and neutron scattering. *Polymer*, *105*, 545–561.
8. Bai, W., Yager, K. G., & Ross, C. A. (2015). In situ characterization of the self-assembly of a polystyrene-polydimethylsiloxane block copolymer during solvent vapor annealing. *Macromolecules*, *48*, 8574–8584.
9. Epps, T. H., Chatterjee, J., & Bates, F. S. (2005). Phase transformations involving network phases in ISO triblock copolymer-homopolymer blends. *Macromolecular Rapid Communications*, *38*, 8775–8784.
10. Kim, G., & Libera, M. (1998). Morphological development in solvent-cast polystyrenepolybutadiene- polystyrene (SBS) triblock copolymer thin films. *Macromolecules*, *31*, 2569–2577.
11. Epps, T. H., Cochran, E. W., Bailey, T. S., Waletzko, R. S., Hardy, C. M., & Bates, F. S. (2004). Ordered network phases in linear poly(isoprene-b-styrene-b-ethylene oxide) triblock copolymers. *Macromolecules*, *37*, 8325–8341.
12. Bates, F. S., & Fredrickson, G. H. (1990). Block copolymer thermodynamics: Theory and experiment. *Annual Review of Physical Chemistry*, *41*, 525–557.
13. Bates, F. S., & Fredrickson, G. H. (1999). Block copolymers-designer soft materials. *Physics Today*, *52*, 32.

Chapter 5
Preferentially Aligned Crystallisation Within a Single Gyroid Network of an ISO Triblock Terpolymer

In this chapter, we investigate the preferential alignment of poly(ethylene oxide) PEO crystallites in the alternating gyroid morphology of an amorphous-semicrystalline triblock terpolymer for which the semicrystalline block comprises one of the two interpenetrating single gyroid networks. Thin films of 80 kg mol^{-1} polyisoprene-*b*-polystyrene-*b*-poly(ethylene oxide) (ISO) were annealed in chloroform vapour to create grains of the alternating gyroid morphology exhibiting exceptional long-range order.[1] The resulting crystalline superstructure and microphase-separated morphology were examined by optical and scanning electron microscopy, and grazing-incidence small- and wide-angle X-ray scattering (GISAXS and GIWAXS). Under crossed polarisers, large areas of uniform birefringence were observed and were identified to be the result of preferentially aligned PEO crystallites. The domains of uniform birefringence were found to coincide and coexist with well-ordered grains of the alternating gyroid morphology, suggesting that the PEO crystallite alignment is strongly coupled to the orientation of the surrounding microphase-separated structure.[2]

[1]Note that whereas a 35 kg mol^{-1} ISO terpolymer was used for the in situ GISAXS study of Chap. 4, here an 80 kg mol^{-1} ISO terpolymer is used. The reason is that the resulting templates are intended for optical metamaterial fabrication and the larger unit cell size should lead to more striking dichroism (cf. Table 2.1).

[2]This chapter is based closely on the experimental section of: Dehmel, R.,* Dolan, J. A.,* Gu, Y., Wiesner, U., Wilkinson, T. D., Baumberg, J. J., Steiner, U., Wilts, B. D. & Gunkel, I. (2017). Optical imaging of large gyroid grains in block copolymer templates by confined crystallization. *Macromolecules*, *50*, 6255–6262. *Equal contribution.

© Springer Nature Switzerland AG 2018

J. A. Dolan, *Gyroid Optical Metamaterials*, Springer Theses,
https://doi.org/10.1007/978-3-030-03011-7_5

5.1 Methods

Details of the methods used may be found in Chap. 3. Briefly, differential scanning calorimetry (DSC) of an $80\,\mathrm{kg\,mol^{-1}}$ ISO triblock terpolymer was carried out on bulk samples. Thin films of the terpolymer were spun atop silicon and fluorine-doped tin oxide (FTO)-coated substrates from a 10% (w/w) solution of the terpolymer in anhydrous anisole. Samples were exposed to controlled solvent vapour atmospheres using a custom annealing chamber and experimental set-up. Dry nitrogen gas was bubbled through a chloroform reservoir and mixed with dry nitrogen before entering the annealing chamber. The solvent concentration in the chamber was controlled by varying the mass flow rate of the two lines. To create gold replicas of the polyisoprene (PI) block of the solvent-annealed ISO thin films, the PI block was degraded by exposure to UV light and removed by immersion of the film in ethanol. The voided terpolymer network was replicated into gold by electrodeposition; this could only be performed for samples on FTO-coated substrates. Birefringence and linear dichroism were observed in both reflection and transmission with a standard polarising optical microscope. A programmable hot-stage was used for crystal melting experiments. GISAXS and GIWAXS measurements were performed ex situ at the D1 beamline of the Cornell High Energy Synchrotron Source, Cornell University, New York, USA. The resulting scattering patterns were reduced and the in-plane and azimuthal line integrations were analysed to determine peak locations and widths.[3]

5.2 Results

As the crystallisation behaviour of ISO depends on the glass transition temperature of the amorphous PS block (T_g^{PS}), and the melting and crystallisation temperatures of the semicrystalline PEO block (T_m^{PEO} and T_c^{PEO}, respectively), differential scanning calorimetry (DSC) was performed to determine these key parameters for the $80\,\mathrm{kg\,mol^{-1}}$ ISO used here (Fig. 5.1). The peaks at 55 °C during heating and 30 °C during cooling are consistent with values previously reported for the melting and crystallisation temperatures of PEO, respectively (Fig. 5.1a) [2]. A shallow T_g^{PS} can be seen at $\approx 87\,^{\circ}\mathrm{C}$ (Fig. 5.1b), determined by the 50% heat capacity change during vitrification. The corresponding T_g^{PS} during heating is $\approx 90\,^{\circ}\mathrm{C}$ and thus slightly higher than during cooling.[4] Although $T_g^{PS} > T_c^{PEO}$, suggesting that crystallisation is

[3] Differential scanning calorimetry was performed and analysed by Dr. Ilja Gunkel. Sample fabrication and characterisation were undertaken jointly by Raphael Dehmel and the author. Scattering experiments were performed by the author, Xiaoyuan Sheng, and Dr. Alessandro Sepe. Data reduction and indexing was performed by Dr. Ilja Gunkel.

[4] The higher T_g^{PS} during heating is probably related to its proximity to the PEO melting peak in the heating curves. The "true" liquid base line is expected to be less steep and any error in its identification shifts both the onset and half-step temperatures to higher values (i.e. away from the T_g^{PS} measured during cooling).

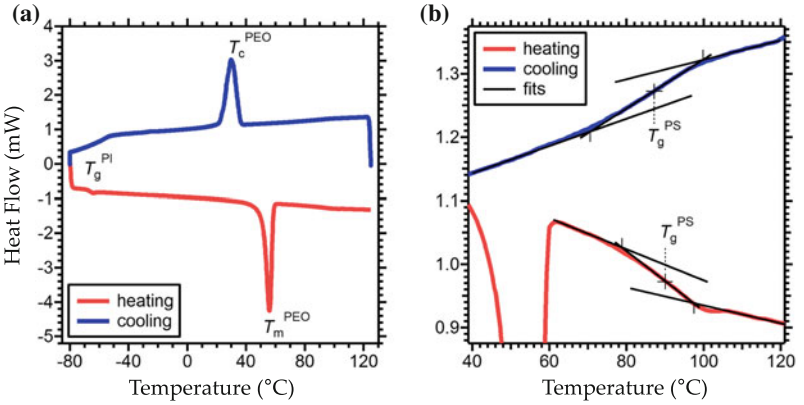

Fig. 5.1 Differential scanning calorimetry (DSC) of 80 kg mol $^{-1}$ ISO triblock terpolymer. **a** The melting and crystallisation peaks are clearly visible at 55 and 30 °C, respectively. **b** A magnification of the region between 40 and 120 °C shows the glass transition of polystyrene at ≈ 87 °C and ≈ 90 °C (half-step temperatures) during cooling and heating, respectively. Reprinted (adapted) from [1] with permission from the American Chemical Society

confined, the glass transition is spread across a wide temperature range (extrapolated onset 71 °C and endpoint 100 °C during cooling). It is therefore possible that the material is not fully vitrified upon crystallisation. The presence and concentration of a solvent will have a strong influence on both crystallisation and vitrification (i.e. both T_g^{PS} and T_c^{PEO} vary with solvent concentration) and these modulated characteristic temperatures ultimately determine the behaviour of the terpolymer during solvent annealing.

5.2.1 Crystalline Superstructure

Thin films of ISO were exposed to controlled amounts of nitrogen gas rich in chloroform and the solvent annealing protocol was optimised to achieve a highly distinct birefringent texture in the dried films. The textures observed in the as-spun and solvent-annealed films, small spherulites and extended domains of uniform birefringence, respectively, are shown in Fig. 5.2. Whereas the former (Fig. 5.2a) were robust, the latter (Fig. 5.2b) were highly sensitive to small variations in annealing parameters (e.g. temperature of the annealing chamber and concentration of the solvent) and the relevant protocols therefore required considerable optimisation. To the author's best knowledge, neither spherulites nor birefringent domains have previously been reported for ISO films, and the extended domains of uniform birefringence, especially over such length scales, have never previously been observed for

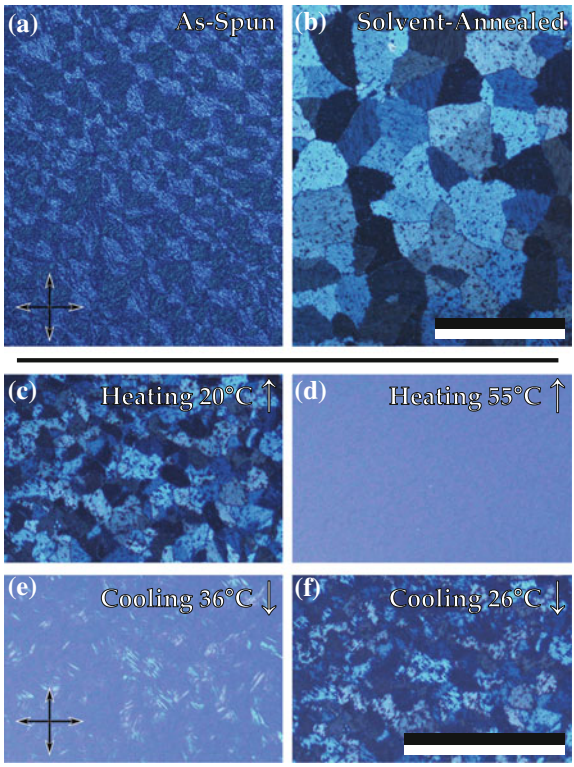

Fig. 5.2 Birefringent textures of as-spun and solvent-annealed ISO thin films and their variation with temperature. Solvent vapour annealing of ISO thin films on silicon substrates yields a distinct birefringent texture in the dried film. Optical micrographs were recorded under crossed polarisers, showing **a** small spherulites in as-spun samples and **b** extended domains of uniform birefringence in solvent-annealed samples. Reprinted (adapted) from [1] with permission from the American Chemical Society. **c** At room temperature, after solvent vapour annealing and before heating, extended domains of uniform birefringence are visible. **d** At 55 °C, the birefringent texture disappears. The residual non-uniformity in the image is caused by the surface roughness of the terpolymer film. **e** The birefringence gradually reappears upon cooling at ≈40 °C. Birefringent features are visible and increase in density upon further cooling to 36 °C. **f** The initial birefringent texture reappears by 26 °C with a nearly identical pattern to **c**. The domains exhibit an increased defect density, which is likely due to incomplete crystallisation. The crossed arrows indicate the orientation of the polarisers. Scale bars: 500 µm. Optical micrographs courtesy of Raphael Dehmel

pure semicrystalline triblock or diblock copolymer melts.

To confirm the crystalline nature of the extended domains of uniform birefringence (i.e. that the birefringence is the result of the semicrystalline PEO and not any underlying form anisotropy), melting experiments were carried out.[5] A heating chamber

[5]Form anisotropy results from the anisotropic arrangement of isotropic constituents (e.g. grains of aligned cylinders in solutions of amorphous diblock copolymers) [3].

with transparent windows allowed the in situ observation of the birefringent textures by polarising optical microscopy. Samples exhibiting extended domains of uniform birefringence (Fig. 5.2c) were heated at a rate of 15 °C min^{-1} and the birefringent texture disappeared at 55 °C (Fig. 5.2d). This temperature is consistent with the melting temperature of PEO as determined by DSC ($T_m^{PEO} \approx 55$ °C). The samples were kept at 55 °C for 1 min, after which the samples were allowed to cool. At a temperature of ≈ 40 °C, the birefringence began to reappear, becoming increasingly clear as the temperature decreased (Fig. 5.2e). Below ≈ 26 °C, no further changes were apparent (Fig. 5.2f). Figure 5.2c, f show nearly identical birefringent textures and patterns. The melting and crystallisation of the birefringent textures shown in Fig. 5.2 therefore clearly corroborate that the birefringence is a result of the semicrystalline nature of the PEO block. Any form anisotropy from an underlying microphase-separated morphology should disappear only upon heating the sample above $T_g^{PS} \approx 90$ °C. The crystalline nature of the birefringence and the impressive uniformity of the birefringent domains must arise from the alignment of the semicrystalline PEO within the domains.

The presence and alignment of semicrystalline PEO in the ISO thin films was studied by grazing-incidence wide-angle X-ray scattering (GIWAXS). Recorded scattering patterns for as-spun samples exhibiting small spherulites (Fig. 5.3a) and solvent-annealed samples exhibiting extended domains of uniform birefringence (Fig. 5.3b) both exhibit strong peaks corresponding to the (120) and (032) reflections of PEO (Fig. 5.3c). Note that the q values of the (120) reflections of the as-spun and solvent-annealed films in Fig. 5.3c are are 3–5% smaller than the values reported for uniaxially-oriented homopolymer PEO after stretching and melt quenching [18]. The slightly larger PEO unit cell sizes are likely due to the complexation of PEO with residual solvent molecules [5]. Indeed, a closer inspection of the (120) reflections reveals a bimodal crystal structure, indicating the coexistence of neat and solvent-complexed PEO crystallites (not shown). The azimuthal distributions of the (120) reflections, measured from the substrate normal, show significant anisotropy (Fig. 5.3d). For the as-spun sample, a peak at 0° is clearly visible, implying that the polymer chains in the semicrystalline PEO (i.e. the crystallite c-axes) are predominantly oriented parallel to the substrate [4]. For the sample exhibiting extended domains of uniform birefringence, the peak at ≈ 40° (40.3 ± 0.1°; FWHM = 14.6°) indicates a different preferential alignment of the semicrystalline PEO with respect to the substrate. The alignment of semicrystalline PEO was observed in all samples exhibiting extended domains of uniform birefringence. The GIWAXS results further corroborate the hypothesis that solvent-annealed samples exhibit macroscopically aligned semicrystalline PEO.

5.2.2 Microphase-Separated Morphology

If the PI phase of the microphase-separated morphology is continuous and makes contact with the conductive substrate, it may be selectively removed and replicated

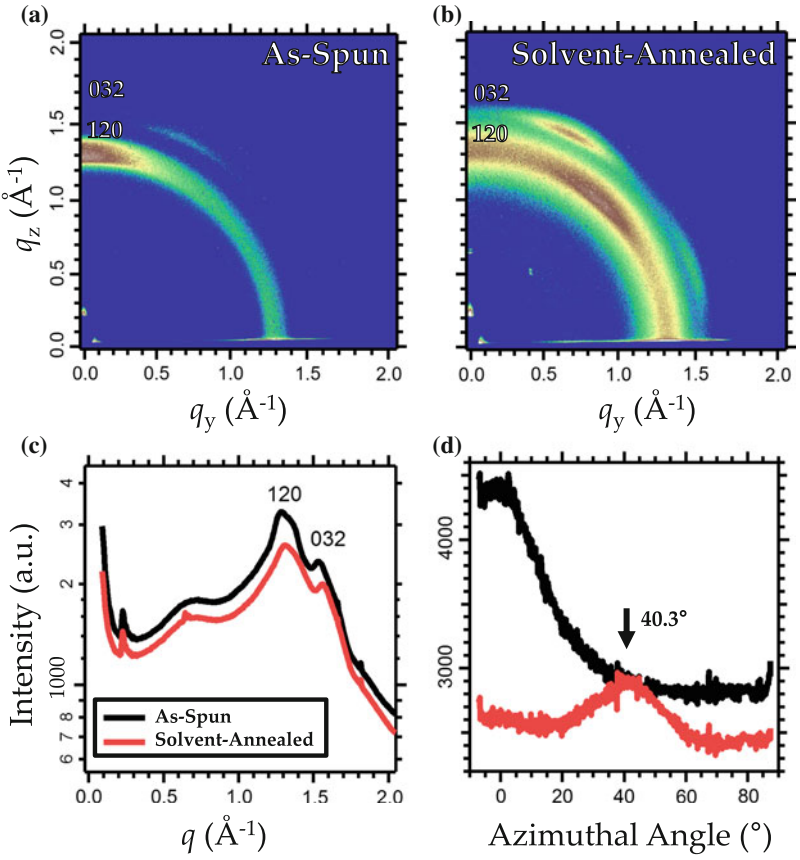

Fig. 5.3 Grazing-incidence wide-angle X-ray scattering (GIWAXS) of as-spun and solvent-annealed ISO thin films. Scattering patterns for **a** an as-spun film exhibiting small spherulites and **b** a solvent-annealed film exhibiting extended domains of uniform birefringence. **c** The characteristic (120) and (032) PEO reflection peaks are clearly visible in the azimuthally-averaged data for both as-spun (black) and solvent-annealed (red) samples. **d** The intensity distribution of the (120) signal as a function of azimuthal angle implies an anisotropic alignment of the semicrystalline PEO [4]

into metal by electrodeposition [6, 7, 19]. This allows the identification of the microphase-separated morphology by scanning electron microscopy (SEM). The microphase-separated morphologies of both as-spun and solvent-annealed samples on FTO-coated glass substrates were investigated by SEM after replication of the PI phase into gold and removal of the remaining PS and PEO (Fig. 5.4). For the as-spun sample exhibiting small spherulites, a disordered continuous structure is visible (Fig. 5.4a). For the solvent-annealed sample exhibiting extended domains of

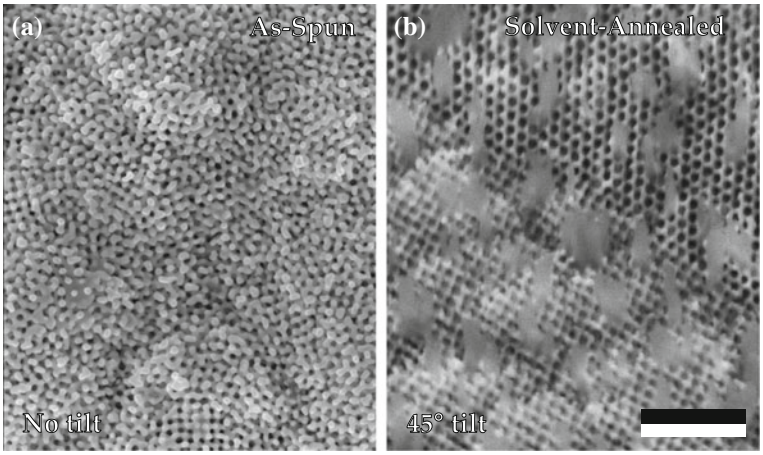

Fig. 5.4 Scanning electron microscope (SEM) micrographs of the replicated PI networks of as-spun and solvent-annealed samples. **a** The replicated gold network of an as-spun sample exhibits a disordered continuous structure. **b** Imaged under an angle of $\approx 45°$, the gold network of a solvent-annealed sample exhibits a regular and highly uniform array of pore sizes. Two domains with different appearances are visible. The six-fold and four-fold pore symmetries observed in the top right and the bottom left are consistent with the $\langle 111 \rangle$ and $\langle 100 \rangle$ directions of a single gyroid, respectively. The flakes on the film surface are residues from the electrodeposition procedure. Scale bar: 500 nm. Reprinted (adapted) from [1] with permission from the American Chemical Society. Electron micrograph **b** courtesy of Raphael Dehmel

uniform birefringence, two differently oriented continuous domains are visible when the sample is viewed under an inclination of 45° (Fig. 5.4b). In a previous study it was shown that a $53\,\mathrm{kg\,mol^{-1}}$ ISO with similar block volume fractions formed an oriented alternating gyroid phase with the $\langle 110 \rangle$ direction perpendicular to the substrate [8]. The $\langle 111 \rangle$ and $\langle 100 \rangle$ directions were therefore inclined by 35 and 45° with respect to the substrate normal, respectively. The highly uniform six-fold (top right) and four-fold (bottom left) pore symmetries in Fig. 5.4b are consistent with a single gyroid network, similarly oriented with the $\langle 110 \rangle$ direction perpendicular to the substrate, viewed along the $\langle 111 \rangle$ and $\langle 100 \rangle$ directions, respectively (cf. Fig. 2.2).

The microphase-separated morphologies were also characterised using grazing-incidence small-angle X-ray scattering (GISAXS) for a range of angles of incidence (Fig. 5.5). The scattering patterns for as-spun samples exhibiting small spherulites and solvent-annealed samples exhibiting extended domains of uniform birefringence are shown in Fig. 5.5a–h, respectively. As the angle of incidence is increased from $\alpha_\mathrm{i} = 0.10°$, below the critical angle of the terpolymer film (Fig. 5.5a), to 0.19°, above the critical angle of the film (Fig. 5.5d), the measured GISAXS patterns of the as-spun sample change significantly. At low α_i, the pattern exhibits diffuse Bragg rods at $q_y \approx 0.012\,\mathrm{Å^{-1}}$ with relatively little intensity along the remainder of the diffuse Debye-Scherrer ring (DDSR) towards $q_y = 0\,\mathrm{Å^{-1}}$ (Fig. 5.5a). Close to the critical angle of the terpolymer but below that of the substrate (evidenced by the enhanced intensity

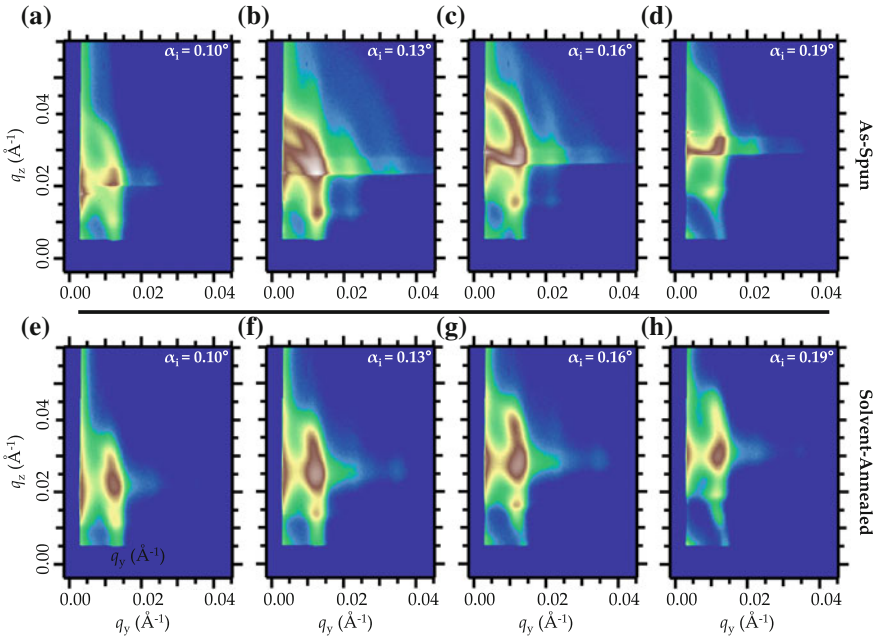

Fig. 5.5 Grazing-incidence small-angle X-ray scattering (GISAXS) of as-spun and solvent-annealed samples at four angles of incidence. GISAXS scattering patterns for **a**–**d** an as-spun sample exhibiting small spherulites and **e**–**h** a solvent-annealed sample exhibiting extended domains of uniform birefringence. The depth of the film probed by the incident X-rays increases with increasing α_i

around the Yoneda band at $q_z \approx 0.023\,\text{Å}^{-1}$), the scattering patterns show significant intensity along the entirety of the DDSR (Fig. 5.5b, c). At angles of incidence above the critical angle of the terpolymer film, the scattering pattern again exhibits diffuse and significantly curved Bragg rods with less intensity along the DDSR (Fig. 5.5d). As the depth of the film probed by the incident X-rays increases with increasing α_i, the observed variation in the GISAXS scattering patterns with angle of incidence implies a variation in microphase-separated morphology across the thickness of the sample. Whereas the as-spun films exhibit anisotropic short-range order at both interfaces, the microphase-separared morphology is nearly isotropic inside the film.

In contrast, the GISAXS scattering patterns for solvent-annealed films exhibit diffuse Bragg rods at $q_y \approx 0.012\,\text{Å}^{-1}$ for all values of α_i probed (Fig. 5.5e–h). The solvent-annealed samples therefore exhibit a microphase-separated morphology with long-range order across the entire thickness of the film. Noting that the SEM micrographs for solvent-annealed samples are consistent with a single gyroid morphology, the observed peaks in the line integrations of the scattering patterns (Fig. 5.6) may tentatively be assigned to the $I4_132$ (i.e. the alternating gyroid) symmetry.

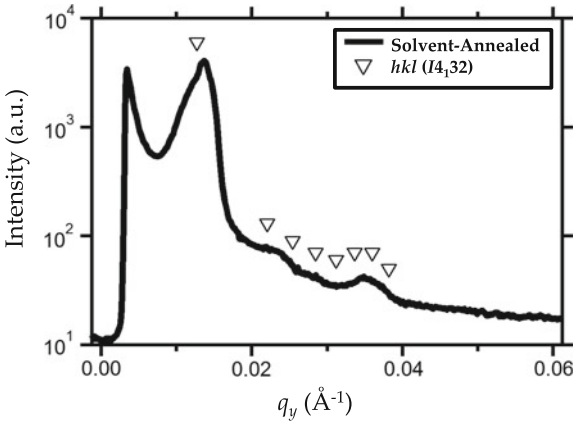

Fig. 5.6 Grazing-incidence small-angle X-ray scattering (GISAXS) of a solvent-annealed film. Line integral at $q_z = 0.026 \pm 0.001\,\text{Å}^{-1}$ of the GISAXS scattering pattern of a solvent-annealed film indexed with the $I4_132$ single gyroid symmetry

5.2.3 *Correlation of Crystalline Superstructure with Microphase-Separated Morphology*

The replication of single-domain alternating gyroid morphologies into gold gives rise to a linear dichroism of the sample (cf. Chap. 2 Sect. 2.6 and Chap. 7) [6, 7]. The comparison of optical micrographs taken before and after gold replication of solvent-annealed samples reveals nearly identical domain patterns (Fig. 5.7). While similar in appearance, the birefringence (terpolymer) and linear dichroism (gold replica) of the domains of the two samples have very different physical origins. In the case of the terpolymer (Fig. 5.7a), the birefringence arises from the preferential alignment of the semicrystalline PEO; in the gold replica (Fig. 5.7b), the linear dichroism arises from a shift of the material's effective plasma frequency with relative orientation of the polarisation axis of light and the replicated gyroid domain [6].[6] To confirm that the dichroism of the gold samples is indeed a plasmonic effect and not the result of residual semicrystalline PEO, the heating experiments of Fig. 5.2 were repeated, and no change in dichroism was detected at elevated temperatures up to 120 °C. Gold replicas were also examined with GIWAXS and no features associated with semicrystalline PEO were observed, confirming the lack of semicrystalline PEO in the gold samples. The optical microscopy results before and after gold replication of solvent-annealed samples imply that the extended domains of uniform birefringence coincide precisely with individual grains of the alternating gyroid morphology.

[6]The physical original of the linear dichroism of single-domain gyroid optical metamaterials is revisited in Chap. 7.

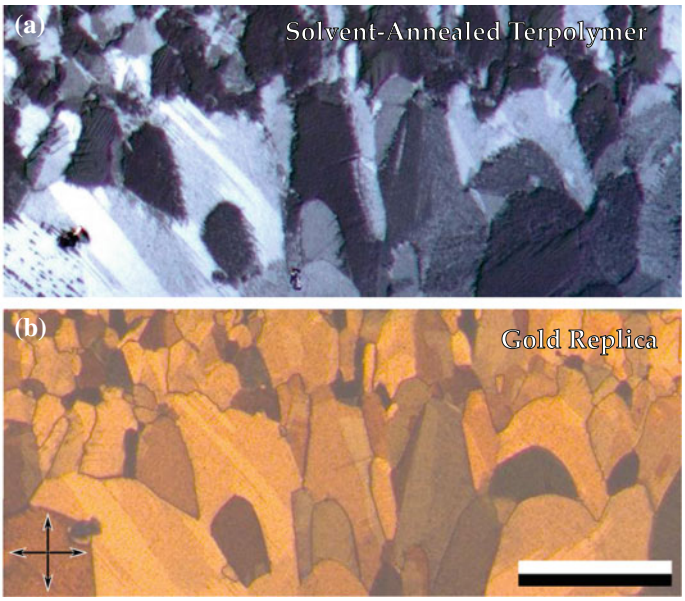

Fig. 5.7 Birefringence and linear dichroism in a solvent-annealed ISO thin film and its gold replica. Optical micrographs of **a** a solvent-annealed ISO film with extended domains of uniform birefringence and **b** the gold replica of the PI network of this film, both under crossed polarisers. Nearly identical domain patterns are observed in the two samples, indicating a correlation between the crystalline superstructure and the microphase-separated terpolymer morphology. Scale bar: 200 µm. Reprinted (adapted) from [1] with permission from the American Chemical Society. Optical micrographs courtesy of Raphael Dehmel

5.3 Discussion

The width of the reflections in the scattering patterns does not enable the unique identification of the microphase-separated morphologies based on GISAXS alone. Using all observations combined, however, the microphase-separated morphologies of the as-spun and solvent-annealed samples can be confidently determined. Solvent-annealed ISO films with extended domains of uniform birefringence possess an alternating gyroid microphase-separated structure, whereas as-spun ISO films exhibiting small spherulites possess a disordered continuous microphase-separated structure. Together with the optical microscopy results, these observations point to a striking correlation between the crystalline superstructure (extended domains of uniform birefringence formed by preferentially aligned semicrystalline PEO) and the underlying microphase-separated morphology (the alternating gyroid) in solvent-annealed samples.

5.3.1 Confined Crystallisation

The elucidation of PEO crystallite alignment in extended domains of uniform birefringence requires the identification of the likely crystallisation mechanism within the solvent-annealed ISO (e.g. breakout, templated, or confined). Although the DSC data imply that the PEO should undergo confined crystallisation ($T_g^{PS} > T_c^{PEO}$), the width of the glass transition and presence of significant chloroform content during annealing complicates this analysis. Despite this, there is significant evidence to support the conclusion that the PEO indeed undergoes confined crystallisation during the solvent annealing protocols used here. SEM (Fig. 5.4b) provides strong evidence for the single gyroid morphology of the replicated PI network, and the GISAXS results (Figs. 5.5e–h and 5.6) are also consistent with the gyroid morphology. In contrast, templated or breakout crystallisation are expected to favour a lamellar morphology.

5.3.2 Multiple Individually Aligned Crystallites

Semicrystalline polymers are typically positively birefringent with the extraordinary optic axis parallel to the stretched chains (i.e. parallel to the crystallite *c*-axes). They are therefore only visible under crossed polarisers when the crystallite *c*-axes have a non-zero projection onto the image plane (e.g. when the polymer chains are parallel or tilted with respect to the substrate). A birefringent texture consisting of extended domains of uniform birefringence implies such an alignment of the PEO crystallites within the large microphase-separated grains (tens to hundreds of micrometres). In an amorphous-semicrystalline block copolymer, the crystallite dimensions are, however, limited by the neighbouring amorphous phase of the microphase-separated morphology (tens to hundreds of nanometres). Extended domains of uniform birefringence must therefore consist of large numbers of similarly aligned PEO crystallites rather than a single macroscopic crystal.

Figure 5.2e provides evidence for this crystal structure. Upon cooling from the melt, individual extended crystalline assemblies are discernible, which have the same alignment within each extended domain. Progressive crystallisation causes these crystallites to coalesce and form the homogeneous birefringent texture (Fig. 5.2f). Since the initial (Fig. 5.2c) and final (Fig. 5.2f) textures are nearly identical, and since the boundaries of the extended domains of uniform birefringence coincide with the grain boundaries, this indicates that the crystallisation process is influenced (or indeed templated) by the microphase-separated morphology.

5.3.3 Crystallite Orientation Perpendicular to the Long Axis of the Gyroid Channels

In an amorphous-semicrystalline block copolymer, any crystallite alignment mechanism within a self-assembled morphology must take into account the likely orientation of the PEO crystallites with respect to the interface between the semicrystalline and amorphous blocks. Despite the remarkable long-range order of the gyroid grains presented here, they are still not sufficiently large to accurately probe a single grain by GISAXS and GIWAXS, and therefore directly and uniquely correlate the orientation of the microphase-separated morphology with that of the PEO crystallites.

Instead, comparisons may be made to the crystallite orientations for PEO confined to other microphase-separated morphologies and how these change with crystallisation conditions. The variation of PEO crystallite orientation with crystallisation temperature is qualitatively similar for lamellae [4], cylinders [9, 10], and hexagonally perforated lamellae [11, 12] of minority PEO surrounded by a majority PS matrix. It is thus reasonable to assume that this variation is similar for a minority PEO single gyroid surrounded by a majority PS matrix. Consider therefore minority PEO cylindrical microdomains of a PS-*b*-PEO diblock copolymer (8.8 kg mol^{-1} PEO and 24.5 kg mol^{-1} PS; $f_{\mathrm{PEO}} = 26\%$). For this copolymer and morphology, the PEO *c*-axes orient perpendicular to the long axis of the cylindrical PS inclusions for a crystallisation temperature $T_{\mathrm{C}}^{\mathrm{PEO}} > 0\,^{\circ}\mathrm{C}$ (i.e. a large crystallisation temperature or small degree of supercooling) [10]. This crystallisation temperature is significantly less than that imposed here ($T_{\mathrm{C}}^{\mathrm{PEO}} \approx 21\,^{\circ}\mathrm{C}$). It is therefore expected that the PEO crystallites within a single gyroid network orient with their *c*-axes perpendicular to the "long axis" of the gyroid channels, the direction of which varies periodically in three dimensions.

The GIWAXS scattering pattern resulting from an as-spun sample exhibiting small spherulites possesses a peak at 0° azimuthal angle (Fig. 5.2a, d). This is consistent with the substrate-parallel *c*-axis orientation reported for spherulites in thin (100 nm–1 μm) films of semicrystalline homopolymers [13, 14]. In this case of "edge-on" lamellar crystals, it has been shown using a simple thermodynamic model that the confinement perpendicular to the substrate results in a significantly lower critical nucleation energy for substrate-parallel crystallite nuclei (so long as the surface energy of the interface between the crystallite and substrate is smaller than that of the interface between the melt and substrate). These lamellar crystals then grow in such a way as to avoid creating additional interfaces [15]. We do not speculate further on the crystallisation mechanism within the as-spun samples as they do not possess a recognisable equilibrium microphase-separated morphology around which a plausible mechanism may be derived.

5.3.4 *Preferentially Aligned Crystallisation Along the* ⟨111⟩ *and* ⟨100⟩ *Directions*

Figure 5.8 outlines the mechanism by which we suggest PEO crystallites are preferentially aligned within a single gyroid microphase-separated morphology. It is anticipated that the PEO crystallites grow preferentially along the ⟨111⟩ and ⟨100⟩ directions of the gyroid (Fig. 5.8a). These directions correspond to the two "straightest paths" across a gyroid network previously identified for isotropic electrochemical growth of platinum within a double gyroid block copolymer template [16]. In that work, the mesoscopic morphology of platinum deposits grown within the gyroid template was analysed by a labyrinth theory and linked to the variation in path-length along different lattice directions within the gyroid. The shape of the electrodeposited platinum clusters was determined by the "straightest"(i.e. least convoluted) pathways across the gyroid network: the ⟨111⟩ and ⟨100⟩ directions. Projections along these two directions, which contain the eponymous gyroidal spirals, can be seen in the electron micrograph in Fig. 5.4b, and the spirals are depicted schematically in Fig. 5.8b, c. The straightness of the gyroidal pathways along these directions depends on the volume fill fraction of the gyroid: the larger the fill fraction the straighter the pathway. For gyroids with a fill fraction of $\approx 17\%$, the volume fill fraction of the PEO block here, the ⟨111⟩ direction contains the straightest paths (Fig. 5.8b); the paths along the ⟨100⟩ directions are 7.5% longer (Fig. 5.8c).

Since PEO crystallisation involves the stacking of extended polymer chains, individual crystallites within semicrystalline PEO are arranged linearly and any change in the crystallisation direction involves the energetically unfavourable incorporation of a defect into the crystallite. In a gyroid network, PEO crystallisation is therefore energetically favoured along the straightest, least convoluted pathways across the lattice, i.e. the ⟨111⟩ and ⟨100⟩ directions. Note that the chemical potential differences driving crystallisation are large. They lie, for example, at the origin of breakout crystallisation, whereby fast crystal growth along particular "lamellae-like" directions destroys and reorganises the existing microphase-separated morphology [20, 21]. In the present case, the availability of nearly straight pathways across the gyroid microphase-separated morphology allows for PEO crystallisation without the destruction of that morphology, resulting in a confined crystallisation that also imposes a distinct preferential alignment for the PEO crystallite growth.

5.3.5 *Distribution of Local Crystallite Orientations About the* ⟨111⟩ *and* ⟨100⟩ *Directions*

However, the path traversed through a gyroid network by the PEO crystallisation growth front is still convoluted: both the ⟨111⟩ and ⟨100⟩ directions form helical paths which spiral or "gyrate" at a constant radius, intersecting with neighbouring paths every 120 and 90°, respectively (Fig. 5.8b, c). The gyroid morphology will

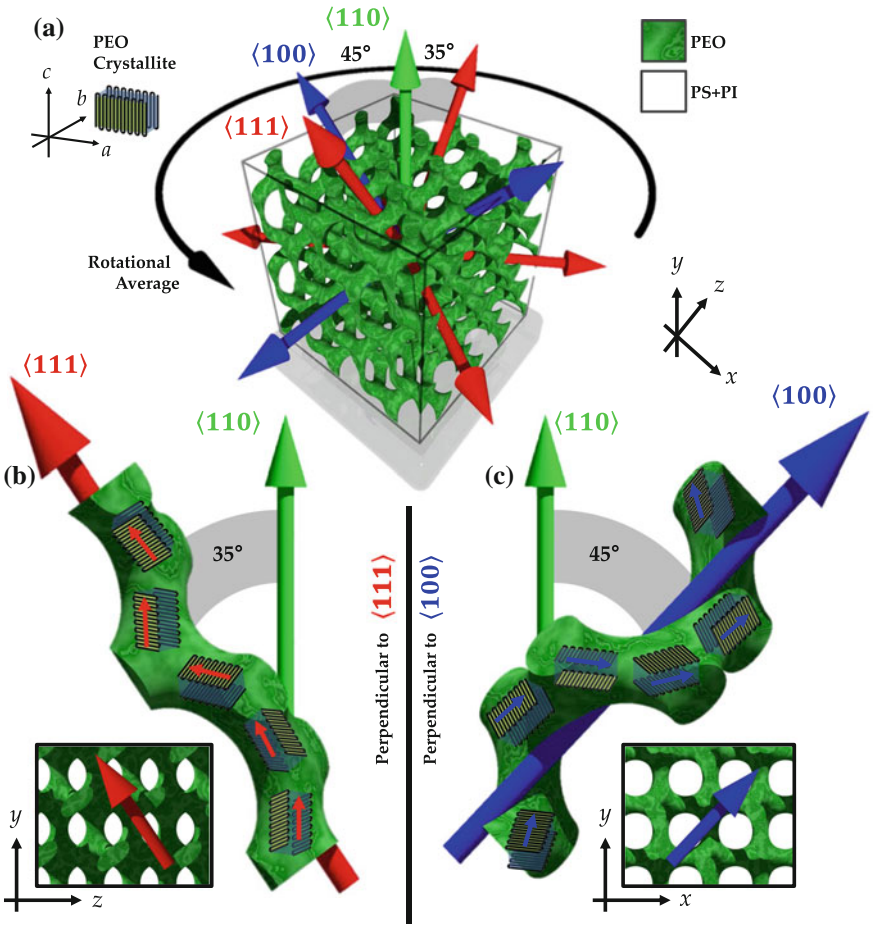

Fig. 5.8 Proposed alignment mechanism of PEO crystallites in a single gyroid network. **a** It is hypothesised that PEO crystallites (top left) are preferentially aligned along the ⟨111⟩ (red arrow) and ⟨100⟩ (blue arrow) directions of the single gyroid. The solvent-annealed ISO gyroids exhibit an orientation whereby the ⟨110⟩ (green arrow) direction is perpendicular to the substrate; the grains are randomly oriented in-plane. Measured GIWAXS and GISAXS scattering patterns therefore correspond to a rotational average about the ⟨110⟩ direction due to measurement over multiple grains. **b** and **c** Details of the gyroid channels in the ⟨111⟩ and ⟨100⟩ directions (large red and blue arrows), respectively. The small red and blue arrows, which indicate the orientation perpendicular to the local PEO crystallite *c*-axes, follow the "long axis" (i.e. the helical path) of the gyroid channels. It is assumed that there is no preferred orientation of the *a*- and *b*-axes relative to the long axis of the gyroid channel and the PEO crystallites depicted are therefore randomly rotated about the small red and blue arrows. The insets indicate the projection of the complete gyroid network from which the details are taken. Reprinted (adapted) from [1] with permission from the American Chemical Society

therefore subject the PEO crystallites, which are anticipated to orient with their *c*-axes perpendicular to the long axis (i.e. the helical path) of the gyroid channels, to continuously varying boundary conditions. This leads to competition between the energetically favourable linear stacking of the PEO crystallites and the requirement that the crystallites follow the path of the gyroid channels to which they are confined. This competition is resolved by the introduction of stacking faults to ensure the local linear arrangement of the PEO crystallites within the gyroid channels. It is therefore necessary for there to be significant deviation of the local PEO crystallite *c*-axis about the plane perpendicular to the ⟨111⟩ and ⟨100⟩ directions. Note that in the case of PEO cylinders there was no preferred orientation of the *a*- and *b*-axes, and we here therefore also assume no preferred orientation of these axes relative to the long axis of the gyroid channel.

As the ISO gyroid grains with long-range order exhibit an orientation whereby the ⟨110⟩ direction is perpendicular to the substrate, the ⟨100⟩ and ⟨111⟩ directions are either in the plane of the substrate or angled 45 and 35° with respect to the substrate normal (Fig. 5.8a) [8]. Given that the growth rates along the ⟨111⟩ and ⟨100⟩ directions are approximately equal, equal populations of PEO crystallites preferentially aligned (on average) at 35 and 45° azimuthal angles would be expected, along with two associated peaks in the corresponding GIWAXS scattering pattern. Instead, only a single peak at $\approx 40°$ ($40.3 \pm 0.1°$) is observed (Fig. 5.3d). However, as already mentioned, the distribution of local PEO crystallite orientations about these two directions (the small red and blue arrows in Fig. 5.8b, c, respectively) is anticipated to be broad. The two peaks at 35 and 45° would therefore likely appear as a single broad peak at their arithmetic mean, 40°, as observed. The preferential growth of PEO crystallites along the ⟨111⟩ and ⟨100⟩ directions is therefore consistent with the measured GIWAXS data.

Individual PEO crystallites are positively birefringent and posses an extraordinary optic axes oriented along the crystallite *c*-axes (i.e. perpendicular to the small red and blue arrows in Fig. 5.8b, c, respectively). The random orientation of positively birefringent crystallite *c*-axes within planes perpendicular to the local helical path of the gyroid channel is optically equivalent to negatively birefringent crystallites with their *c*-axes aligned along the same helical path. The local orientation of these optically equivalent crystallite *c*-axes will vary about the ⟨111⟩ and ⟨100⟩ directions. However, when averaged over a period of the gyroidal spirals, any radial components of the oscillating optic axes will sum to zero. The resulting (effective) optic axis of the crystalline superstructure will therefore be aligned along the net tangential orientation of the optically equivalent crystallite *c*-axes, i.e. along the ⟨111⟩ and ⟨100⟩ directions. Such samples, with a negatively birefringent effective optic axes aligned along either the ⟨111⟩ or ⟨100⟩ directions, would indeed exhibit large domains of uniform birefringence consistent with the optical microscopy results (Fig. 5.2b).

5.4 Conclusion

We have demonstrated the preferential alignment of PEO crystallites confined within a single gyroid network. It is hypothesised that large grains of the alternating gyroid morphology (within which the PEO block of an amorphous-semicrystalline ISO triblock terpolymer forms a single gyroid network) preferentially align the PEO crystallites along the ⟨111⟩ and ⟨100⟩ directions. These directions are those which allow fastest growth of the PEO crystallites (i.e. those in which the path length required to traverse the gyroid network is minimised). The resulting crystalline superstructure appears as extended domains of uniform birefringence under crossed polarisers. This birefringence is purely crystalline in nature (i.e. is not the result of any underlying form anisotropy from the microphase-separated morphology) and may therefore be extinguished upon heating the sample to a temperature which coincides with the melting temperature of the PEO. This temperature is significantly lower than the glass transition temperature of the glassy PS. The associated GIWAXS scattering pattern exhibits significant anisotropy with a peak at an azimuthal angle corresponding to that expected from PEO crystallites aligned along the ⟨111⟩ and ⟨100⟩ directions. The alternating gyroid microphase-separated morphology of the terpolymer films may be confirmed using a combination of techniques including GISAXS, and electron and optical microscopy. In particular, the observed dichroism of gold single gyroids templated by the terpolymer films highlights the strong correlation of the crystalline superstructure with the microphase-separated grains.

Although not the focus of the above study, the exceptional long-range order of the ISO triblock terpolymer templates should be noted. It is from these templates that the single-domain gyroid optical metamaterials, characterised in Chap. 7, are fabricated. However, the ISO terpolymer used here has a greater molecular weight ($80\,\mathrm{kg\,mol^{-1}}$) than that used for the in situ GISAXS study ($35\,\mathrm{kg\,mol^{-1}}$) of Chap. 4. Furthermore, although presented latterly, the ex situ solvent vapour annealing experiments presented here were performed prior to the equivalent in situ studies and could therefore not be informed by their results. Together, the results of both studies corroborate that it is indeed possible to fabricate ISO triblock terpolymer templates with exceptional long-range order which may be used for subsequent gyroid optical metamaterial fabrication (Part II).

References

1. Dehmel, R., Dolan, J. A., Gu, Y., Wiesner, U., Wilkinson, T. D., & Baumberg, J. J. (2017). Optical imaging of large gyroid grains in block copolymer templates by confined crystallization. *Macromolecules*, *50*, 6255–6262.
2. Zhu, L., Cheng, S. Z. D., Calhoun, B. H., Ge, Q., Quirk, R. P., & Thomas, E. L. (2001). Phase structures and morphologies determined by self-organization, vitrification, and crystallization: confined crystallization in an ordered lamellar phase of PEO-b-PS diblock copolymer. *Polymer*, *42*, 5829–5839.

3. Chastek, T. Q., & Lodge, T. P. (2003). Measurement of gyroid single grain growth rates in block copolymer solutions. *Macromolecules*, *36*, 7672–7680.
4. Zhu, L., Cheng, S. Z. D., Calhoun, B. H., Ge, Q., Quirk, R. P., & Thomas, E. L. (2000). Crystallization temperature-dependent crystal orientations within nanoscale confined lamellae of a self-assembled crystallineamorphous diblock copolymer. *Journal of the American Chemical Society*, *122*, 5957–5967.
5. Paternostre, L., Damman, P., & Dosiere, M. (1999). Morphology and crystal structure of the poly(ethylene oxide)-hydroquinone molecular complex. *Journal of Polymer Science Part B: Polymer Physics*, *37*, 1197–1208.
6. Vignolini, S., Yufa, N. A., Cunha, P. S., Guldin, S., Rushkin, I., Stefik, M., et al. (2012). A 3D optical metamaterial made by self-assembly. *Advanced Materials*, *24*, OP23–OP27.
7. Salvatore, S., Demetriadou, A., Vignolini, S., Oh, S. S., Wuestner, S., & Yufa, N. A. (2013). Tunable 3D extended self-assembled gold metamaterials with enhanced light transmission. *Advanced Materials*, *25*, 2713–2716.
8. Stefik, M., Wang, S., Hovden, R., Sai, H., Tate, M. W., Muller, D. A., et al. (2012). Networked and chiral nanocomposites from ABC triblock terpolymer coassembly with transition metal oxide nanoparticles. *Journal of Materials Chemistry*, *22*, 1078–1087.
9. Huang, P., Zhu, L., Cheng, S. Z. D., Ge, Q., Quirk, R. P., & Thomas, E. L. (2001). Crystal orientation changes in two-dimensionally confined nanocylinders in a poly(ethylene oxide)-b-polystyrene/polystyrene blend. *Macromolecules*, *34*, 6649–6657.
10. Huang, P., Guo, Y., Quirk, R. P., Ruan, J., Lotz, B., & Thomas, E. L. (2006). Comparison of poly(ethylene oxide) crystal orientations and crystallization behaviors in nano-confined cylinders constructed by a poly(ethylene oxide)-b-polystyrene diblock copolymer and a blend of poly(ethylene oxide)-b-polystyrene and polystyrene. *Polymer*, *47*, 5457–5466.
11. Zhu, B. L., Cheng, S. Z. D., Huang, P., Ge, Q., Quirk, R. P., & Thomas, E. L. (2002). Nanoconfined polymer crystallization in the hexagonally perforated layers of a self-assembled PS-b-PEO diblock copolymer. *Advanced Materials*, *14*, 31–34.
12. Zhu, L., Huang, P., Chen, W. Y., Ge, Q., Quirk, R. P., & Cheng, S. Z. D. (2002). Nanotailored crystalline morphology in hexagonally perforated layers of a self-assembled PS-b-PEO diblock copolymer. *Macromolecules*, *35*, 3553–3562.
13. Michell, R. M., & Muller, A. J. (2016). Confined crystallization of polymeric materials. *Progress in Polymer Science*, *54–55*, 183–213.
14. Liu, Y.-X., & Chen, E.-Q. (2010). Polymer crystallization of ultrathin films on solid substrates. *Coordination Chemistry Reviews*, *254*, 1011–1037.
15. Wang, Y., Ge, S., Rafailovich, M., Sokolov, J., Zou, Y., Ade, H., et al. (2004). Crystallization in the thin and ultrathin films of poly(ethylene-vinyl acetate) and linear low-density polyethylene. *Macromolecules*, *37*, 3319.
16. Scherer, M. R. J., Cunha, P. M. S., & Steiner, U. (2014). Labyrinth-induced faceted electrochemical growth. *Advanced Materials*, *26*, 2403–2407.
17. Xu, J. T., Turner, S. C., Fairclough, J. P. A., Mai, S. M., Ryan, A. J., & Chaibundit, C. (2002). Morphological confinement on crystallization in blends of poly(oxyethylene-block-oxybutylene) and poly(oxybutylene). *Macromolecules*, *35*, 3614–3621.
18. Takahashi, Y., & Tadokoro, H. (1973). Structural studies of polyethers, (-(CH2)m-O-)n. X. Crystal structure of poly(ethylene oxide). *Macromolecules*, *6*, 672–675.
19. Salvatore, S. (2014). *Optical metamaterials by block copolymer self-assembly (Springer theses)*. Berlin: Springer. ISBN: 3319053310.
20. Xu, J. T., Turner, S. C., Fairclough, J. P. A., Mai, S. M., Ryan, A. J., Chaibundit, C., et al. (2002). Morphological confinement on crystallization in blends of poly(oxyethylene-block-oxybutylene) and poly(oxybutylene). *Macromolecules*, *35*, 3614–3621.
21. Fairclough, J. P. A., Mai, S.-M., Matsen, M. W., Bras, W., Messe, L., Turner, S. C., et al. (2001). Crystallization in block copolymer melts: Small soft structures that template larger hard structures. *The Journal of Chemical Physics*, *114*, 5425.

Part II
Optical Anisotropy in Gyroid Optical Metamaterials

Gold gyroid optical metamaterials are known to possess a reduced plasma frequency and linear dichroism imparted by their intricate sub-wavelength single gyroid morphology. The anisotropic optical properties are, however, only evident when a large individual gyroid domain is investigated. Multi-domain gyroid metamaterials, fabricated by thermal annealing from a polyisoprene-*b*-polystyrene-*b*-poly(ethylene oxide) (ISO) triblock terpolymer and consisting of multiple small gyroid domains with random orientation and handedness, instead exhibit isotropic optical properties (Chap. 6). Comparing three effective medium models, we show in this part that the specular reflectance spectra of such multi-domain gyroid optical metamaterials can be accurately modelled over a broad range of incident angles by a Bruggeman effective medium consisting of a random wire array. That a Bruggeman effective medium can accurately model the experimental reflectance spectra implies that multi-domain gold gyroid optical metamaterials behave both qualitatively and quantitatively as an amorphous composite of gold and air (i.e. nanoporous gold), and that coherent electromagnetic contributions arising from the sub-wavelength gyroid symmetry are not dominant.

Single-domain gyroid metamaterials, fabricated by solvent vapour annealing from the same ISO triblock terpolymer, exhibit the previously observed linear dichroism. However, this dichroism is thoroughly unexpected (and indeed unexplained) given the cubic symmetry of the gyroid morphology. By comparing measured and simulated reflectance and transmittance spectra as a function of azimuthal angle and termination of the single gyroid morphology, we additionally show that it is the anisotropic protrusions resulting from the terminations of the metamaterial which are the physical mechanism underlying the observed linear dichroism (Chap. 7). These protrusions may be modelled by the introduction of a thin anisotropic effective medium layer atop the bulk gyroid optical metamaterial. The significant and unexpected effects of the terminations, which break the effective symmetry of the otherwise isotropic cubic metamaterial, have far-reaching consequences for the use of optical metamaterials fabricated via self-assembly.

Chapter 6
Multi-Domain Gyroid Optical Metamaterials

In this chapter, we investigate the optical properties of multi-domain gold gyroid optical metamaterials fabricated from the alternating gyroid phase of a 80 kg mol^{-1} polyisoprene-*b*-polystyrene-*b*-poly(ethylene oxide) (ISO) triblock terpolymer.[1] The specular reflection of the isotropic metamaterial is measured under a range of angles of incidence of light and the resulting reflectance spectra are compared to those predicted by three of the simplest (and therefore most common) analytical effective medium theories applicable to amorphous composites of spherical or ellipsoidal inclusions of one material in a host matrix of another. We show that a Bruggeman model with ellipsoidal inclusions is the only model considered which can reproduce the features present in the measured reflectance spectra of the investigated multi-domain gold gyroid optical metamaterials, and that such optical metamaterials therefore behave similarly to nanoporous gold.[2]

6.1 Methods

Details of the methods used may be found in Chap. 3. Briefly, thin films of an 80 kg mol^{-1} ISO triblock terpolymer were spun atop fluorine-doped tin oxide (FTO)-coated substrates from a 10% (w/w) solution of the terpolymer in anhydrous anisole. Samples were thermally annealed under vacuum at 180 °C for 30 min then allowed

[1] Unlike those samples previously considered, the triblock terpolymer templates used to fabricate multi-domain gyroid optical metamaterials were thermally, rather than solvent, annealed.

[2] This chapter is based closely on: Dolan, J. A., Saba, M., Dehmel, R., Gunkel, I., Gu, Y., Wiesner, U., Hess, O., Wilkinson, T. D., Baumberg, J. J., Steiner, U. & Wilts, B. D. (2016). Gyroid optical metamaterials: calculating the effective permittivity of multidomain samples. *ACS Photonics 3*, 1888–1896.

© Springer Nature Switzerland AG 2018

J. A. Dolan, *Gyroid Optical Metamaterials*, Springer Theses,
https://doi.org/10.1007/978-3-030-03011-7_6

to cool over approximately 12 h. Gyroid optical metamaterials were created from the terpolymer thin films by degradation of the polyisoprene (PI) block by exposure to UV light and its subsequent removal by immersion of the film in ethanol. The voided terpolymer network was replicated into gold by electrodeposition. Gold is grown both within and atop the polymer template, and the layer of excess bulk gold is cleaved at the interface between the nanostructured and bulk gold, to ensure a smooth top surface, before removal of the remaining terpolymer by exposure to oxygen plasma. Optical characterisation was performed using an automated reflection goniometer with fixed illumination optics and moveable detection optics. The sample and detection arm were arranged to measure the specular reflection. Spectra were recorded at angles of incidence between 15 and 65° in steps of 1°. Linear polarisers were placed at the output of the illumination optics and at the input of the detection optics, aligned to produce transverse electric (TE) or transverse magnetic (TM) polarisations of light with respect to the sample. Reflectance spectra were normalised with respect to the reflectance of a silver mirror at each polar angle.

6.2 Effective Medium Theories

For a material which is homogenous at a particular length scale, its physical properties may be described by a reduced set of effective material parameters [1]. Effective medium theories are approximate analytical means to ascribe a homogeneous (although potentially anisotropic) material parameter, in this case $\varepsilon_{\text{eff}}(\omega)$, to a heterogeneous mixture of two or more components [2]. Such theories are anticipated to hold when the inhomogeneity length scale of the material and the local variation in the electric field are both significantly smaller than the wavelength of interest [3]. Although numerous approaches of varying complexity exist, the two considered in this chapter are arguably the most prevalent: the Maxwell-Garnett theory for spherical inclusions and the Bruggeman theory [2, 3].

6.2.1 Maxwell-Garnett Theory: Spherical Inclusions

The simplest form of the Maxwell-Garnett effective medium theory considers spherical inclusions of one material in a host matrix of another (Fig. 6.1a). The effective permittivity is found by solving the implicit equation [2]

$$\frac{(\varepsilon_1(\omega)-\varepsilon_2(\omega))f_1}{\varepsilon_2(\omega)+(\varepsilon_1(\omega)-\varepsilon_2(\omega))A}+\frac{\varepsilon_2(\omega)-\varepsilon_{\text{eff}}(\omega)}{\varepsilon_2(\omega)+(\varepsilon_{\text{eff}}(\omega)-\varepsilon_2(\omega))A}=0, \tag{6.1}$$

where $\varepsilon_{\text{eff}}(\omega)$ is the (isotropic) effective permittivity of the composite, $\varepsilon_1(\omega)$ is the permittivity of the first component (the inclusion), $\varepsilon_2(\omega)$ is the permittivity of the second component (the host), f_1 is the volume fraction of the first component, A

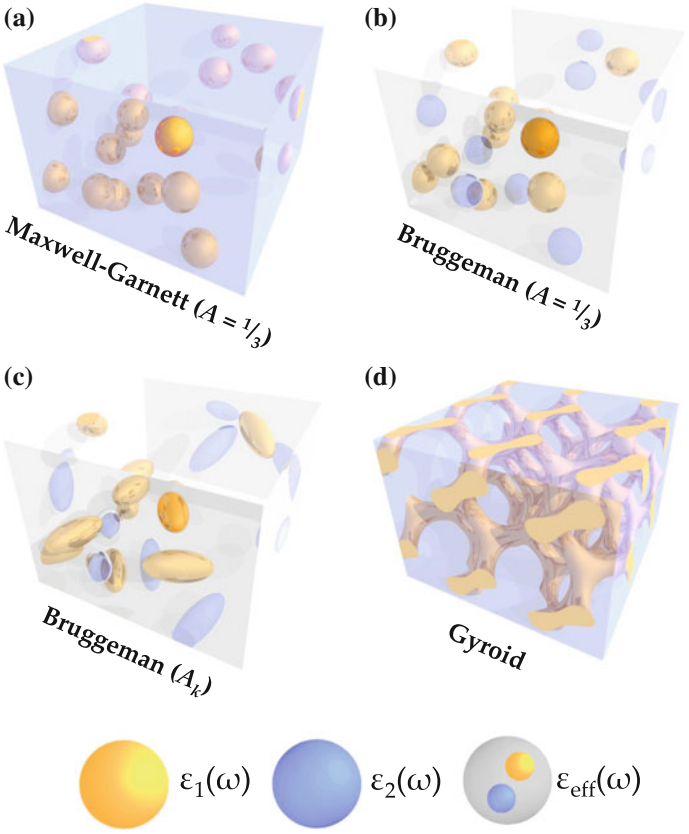

Fig. 6.1 Sketches of the mathematical representations of various effective medium theories. **a** Maxwell-Garnett, Eq. (6.1), where the effective permittivity ($\varepsilon_{\text{eff}}(\omega)$) is derived by considering spherical inclusions ($A = 1/3$) of one material ($\varepsilon_1(\omega)$) in a host matrix of another ($\varepsilon_2(\omega)$). **b** Bruggeman ($A = 1/3$), Eq. (6.2), where the effective permittivity ($\varepsilon_{\text{eff}}(\omega)$) is derived by averaging over single inclusions ($\varepsilon_1(\omega)$ and $\varepsilon_2(\omega)$) individually embedded in an effective medium consisting of all other inclusions ($\varepsilon_{\text{eff}}(\omega)$). **c** Bruggeman ($A_k$), Eq. (6.4), where the effective permittivity ($\varepsilon_{\text{eff}}(\omega)$) is derived analogously to the case where $A = 1/3$ except that all individual spherical inclusions are replaced by randomly oriented ellipsoids. **d** The single gyroid morphology for which an effective medium theory is sought. Note that a single domain is shown but the samples considered here consist of numerous randomly oriented multi-domains. Reprinted (adapted) from [4] with permission from the American Chemical Society

is the depolarisation factor (1/3 for spherical inclusions), and ω is the frequency.[3] The above theory is strictly valid only when the volume fill fraction of the inclusions is small. As a result, the above equation is not invariant under the transformation $\varepsilon_1(\omega) \leftrightarrow \varepsilon_2(\omega)$ and $f_1 \rightarrow f_2$. Asymmetric formulations such as this are only valid

[3]The depolarisation factor relates the dipole moment of a dielectric ellipsoid to the applied external electric field and varies from 0 (disks) to 1 (wires).

for low volume fractions of the polar phase [5]. Nonetheless, the Maxwell-Garnett effective medium theory should be considered due to its widespread usage and having previously been employed to justify the differing behaviour of gold gyroid optical metamaterials from an amorphous composite (cf. Chap. 2 Sect. 2.6) [6].

6.2.2 Bruggeman Theory: Spherical Inclusions

We adopt here a version of the Bruggeman effective medium theory in which all constituents of the composite are treated symmetrically. If the inclusions are again assumed to be spherical (Fig. 6.1b), the effective permittivity is found by solving the implicit equation [5]

$$\frac{(\varepsilon_1(\omega) - \varepsilon_{\text{eff}}(\omega))\, f_1}{\varepsilon_{\text{eff}}(\omega) + (\varepsilon_1(\omega) - \varepsilon_{\text{eff}}(\omega))\, A} + \frac{(\varepsilon_2(\omega) - \varepsilon_{\text{eff}}(\omega))\, f_2}{\varepsilon_{\text{eff}}(\omega) + (\varepsilon_2(\omega) - \varepsilon_{\text{eff}}(\omega))\, A} = 0, \tag{6.2}$$

where $\varepsilon_{\text{eff}}(\omega)$, $\varepsilon_1(\omega)$, $\varepsilon_2(\omega)$, f_1, A, and ω are defined as above, and $f_2 = 1 - f_1$ is the volume fill fraction of the second component. Note that the above equation is now invariant under the transformation $\varepsilon_1 \leftrightarrow \varepsilon_2$ and $f_1 \leftrightarrow f_2$, indicating that the Bruggeman effective medium theory is applicable for any given volume fill fraction. It is therefore anticipated that this simplest form of the Bruggeman theory may more accurately model the behaviour of 30% fill fraction gyroid optical metamaterials, such as those considered here.

6.2.3 Bruggeman Theory: Ellipsoidal Inclusions

Although the Bruggeman effective medium theory is insensitive to the absolute size of the sub-wavelength inclusions of a composite, it is possible to extend the theory to take anisotropy of the inclusions into account. This is done by modelling such inclusions as aligned ellipsoids with semi-axes a_k. In such a case the depolarisation factor A in Eq. (6.2) is replaced by [5]

$$A_k = \frac{a_1 a_2 a_3}{2} \int_0^\infty \frac{\mathrm{d}u}{(a_k^2 + u)\sqrt{(a_1^2 + u)(a_2^2 + u)(a_3^2 + u)}}, \tag{6.3}$$

where A_k is the depolarisation factor for light linearly polarised along the k^{th} axis of an aligned ellipsoidal inclusion. Note that the derived effective permittivity is hence only valid for that same relative orientation of linearly polarised light and the effective permittivity of the material is anisotropic (i.e. when all ellipsoidal inclusions are assumed to be aligned). However, it is also possible to define a macroscopically isotropic effective permittivity whilst allowing for microscopic anisotropy if the ellip-

soidal inclusions are assumed to be randomly oriented in the composite (Fig. 6.1c). In such a case, the effective permittivity is derived by solving the implicit equation [5]

$$\sum_{k=1}^{3} \frac{(\varepsilon_1(\omega) - \varepsilon_{\text{eff}}(\omega))\, f_1}{\varepsilon_{\text{eff}}(\omega) + (\varepsilon_1(\omega) - \varepsilon_{\text{eff}}(\omega))\, A_k} + \frac{(\varepsilon_2(\omega) - \varepsilon_{\text{eff}}(\omega))\, f_2}{\varepsilon_{\text{eff}}(\omega) + (\varepsilon_2(\omega) - \varepsilon_{\text{eff}}(\omega))\, A_k} = 0, \quad (6.4)$$

where $\varepsilon_{\text{eff}}(\omega)$, $\varepsilon_1(\omega)$, $\varepsilon_2(\omega)$, f_1, f_2, and ω are as defined above, and A_k are the three depolarisation factors corresponding to the geometry of the ellipsoidal inclusions ($A_1 + A_2 + A_3 = 1$). Note that this equation is identical for both a polycrystalline sample consisting of numerous randomly oriented *anisotropic* domains, and a composite sample consisting of equal amounts of three *isotropic* constituents of differing permittivities or depolarisation factors [1]. Note also that the Maxwell-Garnett theory may similarly be extended to take into account microscopic anisotropy (discussed below).

6.2.4 Model Fitting

Where an effective medium model requires fitting, the MATLAB optimisation toolbox was used to minimise the cost function

$$f(\mathbf{A}) = \frac{1}{N \times M} \sum_{i=1}^{N} \sum_{j=1}^{M} \left(\log_{10} R_{\text{exp}}(\lambda_i, \theta_j^{\text{in}}) - \log_{10} R_{\text{model}}(\lambda_i, \theta_j^{\text{in}}, \mathbf{A}) \right)^2, \quad (6.5)$$

such that

$$A_1 + A_2 + A_3 = 1, \quad (6.6)$$

where $\mathbf{A} = [A_1, A_2, A_3]$, A_k is the k^{th} depolarisation factor, λ_i is the i^{th} wavelength, θ_j^{in} is the j^{th} angle of incidence, N is the total number of wavelengths, M is the total number of angles of incidence, and $R_{\text{exp}}(\lambda_i, \theta_j^{\text{in}})$ and $R_{\text{model}}(\lambda_i, \theta_j^{\text{in}}, \mathbf{A})$ are the experimental and modelled reflectance spectra, respectively. The modelled reflectance spectra are in turn calculated from the Fresnel equations for reflection from a semi-infinite non-magnetic homogeneous medium for TE

$$R_{\text{model}}^{\text{TE}}(\lambda_i, \theta_j^{\text{in}}, \mathbf{A}) = \left| \frac{n_{\text{air}} \cos(\theta_j^{\text{in}}) - n_{\text{eff}}(\lambda_i, \mathbf{A}) \cos(\theta_j^{\text{tr}})}{n_{\text{air}} \cos(\theta_j^{\text{in}}) + n_{\text{eff}}(\lambda_i, \mathbf{A}) \cos(\theta_j^{\text{tr}})} \right|^2, \quad (6.7)$$

and TM

$$R_{\text{model}}^{\text{TM}}(\lambda_i, \theta_j^{\text{in}}, \mathbf{A}) = \left| \frac{n_{\text{eff}}(\lambda_i, \mathbf{A}) \cos(\theta_j^{\text{in}}) - n_{\text{air}} \cos(\theta_j^{\text{tr}})}{n_{\text{eff}}(\lambda_i, \mathbf{A}) \cos(\theta_j^{\text{in}}) + n_{\text{air}} \cos(\theta_j^{\text{tr}})} \right|^2, \quad (6.8)$$

polarised light, where n_{air} and $n_{\text{eff}}(\lambda_i, \mathbf{A})$ are the refractive indices of air and the effective medium, respectively, and θ_j^{tr} is the j^{th} (complex) transmitted angle calculated by Snell's law, i.e.

$$n_{\text{air}} \sin(\theta_j^{\text{in}}) = n_{\text{eff}}(\lambda_i, \mathbf{A}) \sin(\theta_j^{\text{tr}}). \tag{6.9}$$

The assumption that the gold gyroid optical metamaterial appears semi-infinite (and that the derived effective permittivity is insensitive to film thickness) is based upon the thickness of the film ($\approx 1\,\mu\text{m}$), the unit cell size ($\approx 60\,\text{nm}$), and previous studies of film thickness effects in gold gyroid optical metamaterials which indicate that the reflectance spectra do not change beyond a threshold sample thickness [7]. The effective medium models from which $n_{\text{eff}}(\lambda_i, \mathbf{A})$ is derived require as an input the permittivity of bulk gold $\varepsilon_{\text{Au}}(\omega)$, which is here taken as that measured by Olmon et al. [8] Optimised depolarisation factors are calculated for each polarisation state of light.

6.3 Results

The most appropriate analytical effective medium theory to describe the optical response of multi-domain gold gyroid optical metamaterials is determined by comparing experimental and predicted reflectance spectra over a range of angles of incidence.

6.3.1 Multi-Domain Gyroid Optical Metamaterials

An optical and electron micrograph of the multi-domain gyroid optical metamaterial, the geometry of the experiment, and the resulting reflectance spectra for transverse magnetic (TM) and transverse electric (TE) polarisations of incident light are shown in Fig. 6.2. The optical micrograph captured under linearly polarised light (Fig. 6.2a) highlights the light orange colour of the metamaterial and the the electron micrograph of an individual domain (Fig. 6.2b) is consistent with the gyroid nanostructure previously observed for this terpolymer [6, 7, 9]. Both TM (Fig. 6.2d) and TE (Fig. 6.2e) reflectance spectra are qualitatively similar to those of bulk gold (Fig. 6.3a, b), insofar as they exhibit low reflectance at shorter wavelengths and increased reflectance at longer wavelengths, across all angles of incidence. In bulk gold, these features are attributable to interband transitions and the plasma frequency, respectively.[4] However, the measured spectra differ quantitatively from those of bulk gold due both to

[4]Recall that the permittivity of a metal may be given by $\varepsilon(\omega) = \varepsilon_{\text{ib}}(\omega) + 1 - \omega_{\text{p}}^2/(\omega^2 + i\Gamma\omega)$, where $\varepsilon_{\text{ib}}(\omega)$ represents the contribution from the interband transitions, ω_{p} is the plasma frequency, and Γ is the damping constant [2].

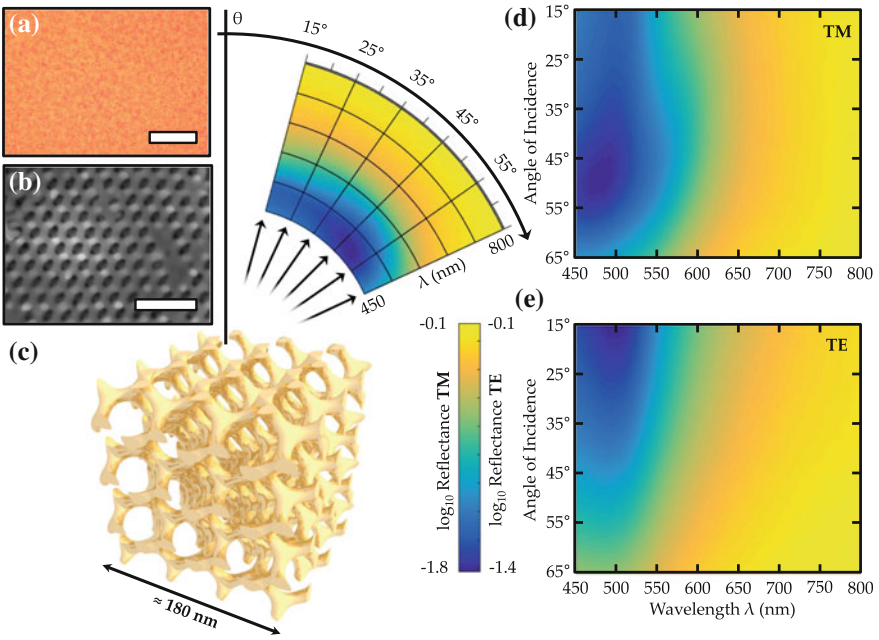

Fig. 6.2 Multi-domain gyroid optical metamaterials: optical and electron micrographs, experiment geometry, and measured reflectance spectra. **a** Optical micrograph of multi-domain gold gyroid optical metamaterial under linearly polarised light. Scale bar: 100 µm. **b** Electron micrograph of an individual domain of the sample. Scale bar: 200 nm. **c** Specular reflectance spectra of the gyroid optical metamaterial are measured as a function of angle of incidence between 15–65°, and 450–800 nm. Although a single gyroid domain is shown for clarity, the measurement spot size in fact encompasses a large number of randomly oriented multi-domains. **d** The reflectance spectra as a function of angle of incidence for transverse magnetic (TM) polarised light. Logarithmic colour scale extends from −1.8 to −0.1. **e** The same for transverse electric (TE) polarised light. Logarithmic colour scale extends from −1.4 to −0.1. Reprinted (adapted) from [4] with permission from the American Chemical Society

a lowered effective plasma frequency and their variation with angle of incidence. Otherwise, the spectra exhibit the general decrease (increase) in reflectance for TM (TE) polarised light with increasing angle of incidence, with an effective Brewster's angle of $\approx 50°$.[5]

6.3.2 *Effective Medium Models*

A comparison between the measured and modelled reflectance spectra across all wavelengths and angles of incidence for TM polarised light is shown in Fig. 6.4; the

[5]For a pure dielectric, Brewster's angle is the angle at which the TM specular reflection reduces to zero.

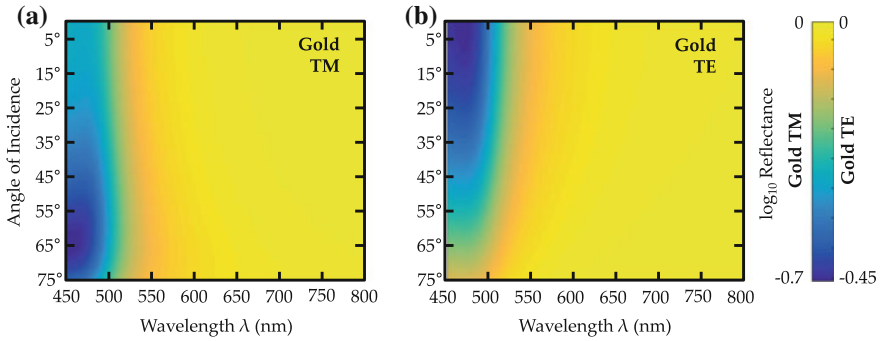

Fig. 6.3 Reflectance spectra of pure gold. **a** The reflectance spectra of pure gold as a function of angle of incidence calculated from $\varepsilon_{\text{Au}}(\omega)$ for transverse magnetic (TM) polarised light. Logarithmic colour scale extends from -0.7 to 0. **b** The same for transverse electric (TE) polarised light. Logarithmic colour scale extends from -0.4 to 0. Tabulated data for the permittivity of bulk gold is that found in Olmon et al. [8] Reprinted (adapted) from [4] with permission from the American Chemical Society

same for TE polarised light is shown in Fig. 6.5. The effective permittivity $\varepsilon_{\text{eff}}(\omega)$ used to generate the modelled spectra in Fig. 6.4b was calculated using the Maxwell-Garnett theory by setting $\varepsilon_1(\omega) = \varepsilon_{\text{Au}}(\omega)$, $\varepsilon_2(\omega) = 1$, $f_1 = 0.3$, and $A = 1/3$ (i.e. spherical inclusions) in Eq. (6.1). Clearly the Maxwell-Garnett effective medium theory is a poor model for the effective permittivity of the gyroid optical metamaterial as it predicts a striking dip in reflectance at an effective Brewster's angle of $\approx 60°$, which is entirely absent in the measured data. Despite also assuming spherical inclusions, the effective permittivity calculated using the Bruggeman theory, by again setting $\varepsilon_1(\omega)$, $\varepsilon_2(\omega)$, f_1, and A as above in Eq. (6.2), results in a far better qualitative match between the measured and modelled reflectance spectra (Fig. 6.4c). The global reflectance minimum at $\approx 50°$ between 450 and 500 nm is reproduced well. However, the spectra still exhibit a decrease in reflectance at long wavelengths and high angles of incidence which is not present in the experimental data. This decrease in reflectance is absent in the reflectance spectra of Fig. 6.4d, which uses our microscopically anisotropic Bruggeman theory. These spectra were modelled by setting $\varepsilon_1(\omega)$, $\varepsilon_2(\omega)$, and f_1 as above, and $A_1 = 0.66$, $A_2 = 0.34$, and $A_3 = 0$ in Eq. (6.4). These depolarisation factors were found by performing a constrained optimisation to fit the TM reflectance spectra generated by the model to the measured data.

A quantitative comparison of the goodness of fit of each model is presented in Table 6.1. Cost functions $f(\mathbf{A})$ are tabulated not only for TM but also TE polarisation using the depolarisation factors derived from the TM measurements. Note that the cost function evaluated for TE polarisation using the depolarisation factors derived from the TM measurements ($A_1 = 0.66$, $A_2 = 0.34$, and $A_3 = 0$) is only 0.66% larger than the same cost function evaluated for TE polarisation using the depolarisation factors derived from the TE measurements ($A_1 = 0.70$, $A_2 = 0.30$, and $A_3 = 0$). This would not in general be the case (e.g. for an anisotropic sample).

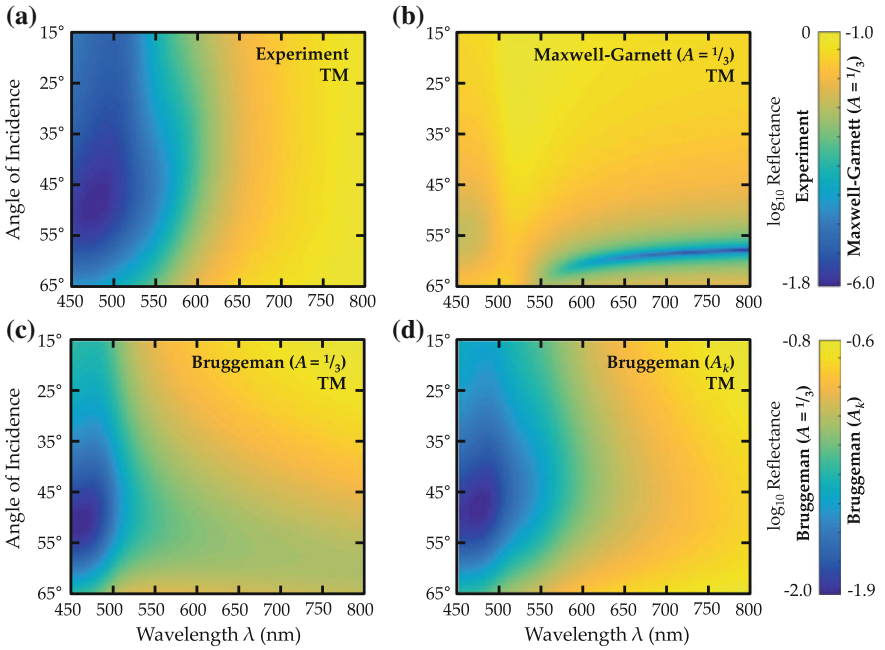

Fig. 6.4 Comparison of measured and modelled TM reflectance spectra as a function of angle of incidence using three effective medium theories. **a** The measured reflectance spectra of multi-domain gyroid optical metamaterials for transverse magnetic (TM) polarised light repeated from Fig. 6.2d. Logarithmic colour scale extends from -1.8 to 0. **b** The reflectance spectra generated using the Maxwell-Garnett theory. Logarithmic colour scale extends from -6.0 to -1.0. **c** The same generated using the Bruggeman theory and $A = 1/3$, i.e. spherical inclusions. Logarithmic colour scale extends from -2.0 to -0.8. **d** The same generated using the Bruggeman theory and $A_1 = 0.66$, $A_2 = 0.34$, and $A_3 = 0$, i.e. ellipsoidal inclusions. Logarithmic colour scales extends from -1.9 to -0.6. Reprinted (adapted) from [4] with permission from the American Chemical Society

Table 6.1 Table of cost functions $f(\mathbf{A})$ associated with the various effective medium theories, equations, polarisations, and vector of depolarisation factors ($\mathbf{A}$). A lower value of cost function indicates a better fit

Model (Equation)	Polarisation	$\mathbf{A}$	$f(\mathbf{A})$
Maxwell-Garnett (6.1)	TM	1/3	2.02
Bruggeman (6.2)		1/3	0.28
Bruggeman (6.4)		[0.66, 0.34, 0]	0.12
Maxwell-Garnett (6.1)	TE	1/3	0.34
Bruggeman (6.2)		1/3	0.08
Bruggeman (6.4)		[0.66, 0.34, 0]	0.04

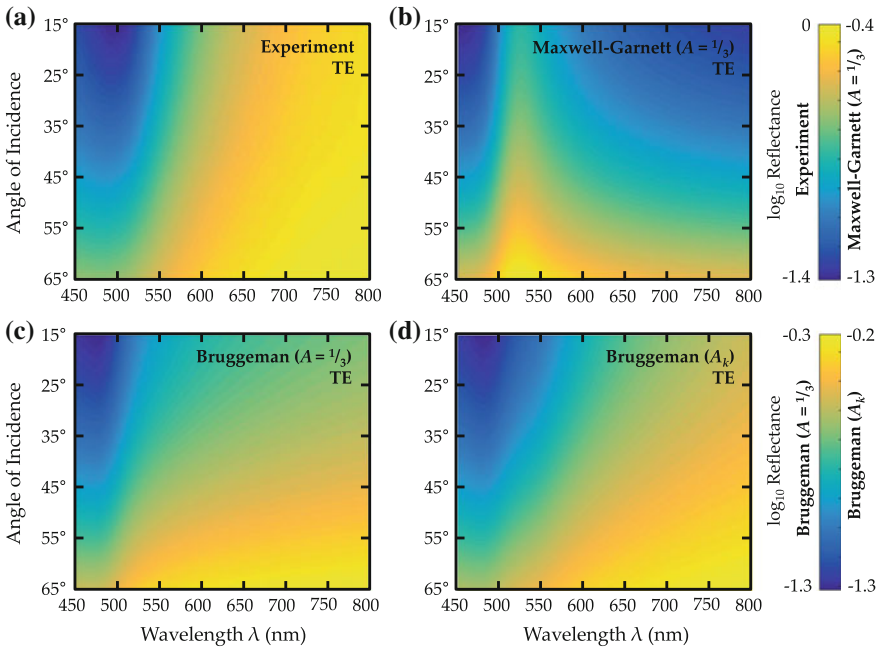

Fig. 6.5 Comparison of measured and modelled TE reflectance spectra as a function of angle of incidence using three effective medium theories. **a** The measured reflectance spectra of multi-domain gyroid optical metamaterials for transverse electric (TE) polarised light. Logarithmic colour scale extends from -1.4 to 0. **b** The reflectance spectra generated using the Maxwell-Garnett theory. Logarithmic colour scale extends from -1.3 to -0.45. **c** The same generated using the Bruggeman theory and $A = 1/3$, i.e. spherical inclusions. Logarithmic colour scale extends from -1.3 to -0.3. **d** The same generated using the Bruggeman theory and $A_1 = 0.66$, $A_2 = 0.34$, and $A_3 = 0$, i.e. ellipsoidal inclusions. Logarithmic colour scale extends from -1.3 to -0.2. Reprinted (adapted) from [4] with permission from the American Chemical Society

Both fits yield $A_3 = 0$, which thus selects a wire (i.e. a uniaxially infinitely extended ellipsoid) with, as $A_1 \neq A_2$, an elliptical cross-section. It is therefore clear that the microscopically anisotropic Bruggeman model consisting of randomly oriented wire inclusions is the best of the three effective medium models considered, and that only a single set of depolarisation factors, $A_1 = 0.66$, $A_2 = 0.34$, and $A_3 = 0$, is necessary to model both TM and TE measurements.

6.3.3 Host Refractive Index and Volume Fill Fraction

A good model for the effective permittivity of the gyroid optical metamaterial should be capable not only of reproducing the measured reflectance spectra presented in this chapter, but also the previously reported behaviours as a function of refractive index of

the host and volume fill fraction of gold (cf. Chap. 2 Sect. 2.6 and Table 2.1). Figure 6.6 compares measurements performed by Salvatore et al. on 30% fill fraction gold gyroids infiltrated with various refractive index media with the optimised Bruggeman model [9]. Following the convention in that work, each normal incidence spectrum is characterised by its plasma edge, the wavelength of the point of inflection of the reflectance spectrum. In the simplest Drude model of the permittivity of metals, the plasma wavelength is the wavelength at which the permittivity changes from positive to negative, and is characteristic of the density and effective mass of the free electrons in the metal.[6] The plasma edge is not the plasma wavelength but behaves similarly and may be more readily and systematically identified from experimental data [9]. Figure 6.6a reproduces the reflectance spectra measured by Salvatore et al. upon infiltration of the gyroid optical metamaterial with media of refractive indices $n_{\text{fill}} = 1.0, 1.33, 1.5$, and 1.7, and indicates the plasma edge in each case (the labelled vertical lines). Note how the plasma edge is red-shifted with increasing host refractive index. Figure 6.6b plots equivalent normal incidence reflectance spectra derived using the optimised Bruggeman model with $\varepsilon_2(\omega)$ of Eq. (6.4) set to n_{fill}^2, respectively. Again the plasma edge is red-shifted with increasing host permittivity. Although the measured and modelled plasma edges do not perfectly coincide, it is clear from Fig. 6.6c that the modelled plasma edges are within experimental error for each refractive index. Therefore, despite the dissimilarity between the measured and modelled normal incidence reflectance spectra, the model successfully predicts the plasma edge of the gold gyroid optical metamaterial. Furthermore, the optimised Bruggeman model performs better in this respect than the tri-helical metamaterial (THM) analytical model, also reproduced from Salvatore et al. and shown in Fig. 6.6c [9].

The results of the optimised Bruggeman model may also be compared to previously measured data where the volume fill fraction of gold is varied. Figure 6.7a shows normal incidence reflectance spectra from Salvatore et al. as the volume fill fraction of the gold gyroid is increased from 30 to 90%. Only four of the five plasma edges are shown, since those for the 75 and 90% fill fraction gyroids are within 2 nm of one another. Whereas the plasma edge is red-shifted with increasing refractive index of the host, it is blue-shifted as the fill fraction increases and the reflectance of the gyroid optical metamaterial tends towards that of bulk gold. Figure 6.7b plots equivalent normal incidence reflectance spectra calculated from the optimised Bruggeman model. Here only two of the five plasma edges are shown as all of those corresponding to fill fractions above 30% are extremely close (within 2 nm). Again the plasma edge is blue-shifted with increased fill fraction, as it was in the measured spectra. However, as can be seen in Fig. 6.7c, there is significant deviation between the measured and predicted plasma edges for intermediate fill fractions between about 40 and 70%. Outside of this region (i.e. at low and high fill fractions) the optimised Bruggeman model performs well and is comparable to the THM model.

[6] The simplest Drude model describes the (lossless) permittivity of a metal as $\varepsilon(\omega) = 1 - \omega_{\text{p}}^2/\omega^2$, where ω_{p} is the plasma frequency. The plasma wavelength is given by $\lambda_{\text{p}} = 2\pi c/\omega_{\text{p}}$, where c is the speed of light in free space [2].

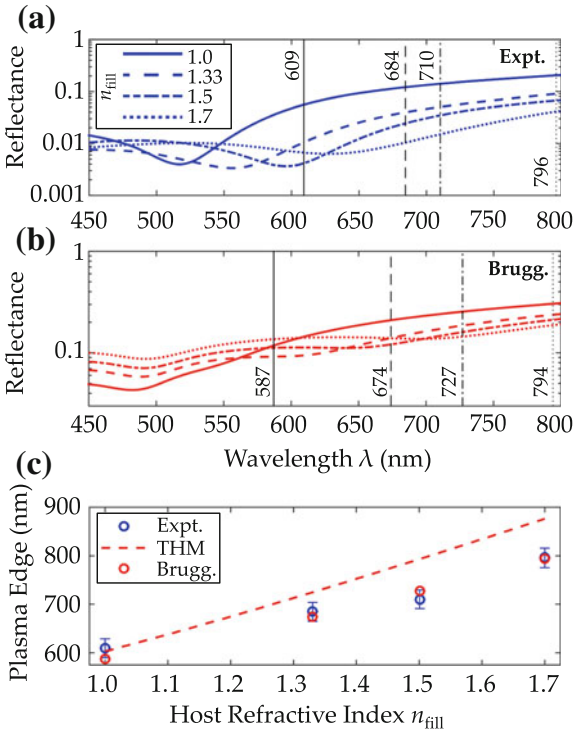

Fig. 6.6 Variation in normal incidence reflectance spectra and plasma edge as a function of host refractive index. **a** Measured reflectance spectra at normal incidence for 30% fill fraction gold gyroid optical metamaterials infiltrated with media of refractive indices $n_{\text{fill}} = 1.0$ (solid line), 1.33 (dashed line), 1.5 (dotted-dashed line), and 1.7 (dotted line). Data reproduced from Salvatore et al. [9] **b** Modelled normal incidence reflectance spectra using the optimised Bruggeman model where $\varepsilon_2(\omega)$ of Eq. (6.4) is set to $n_{\text{fill}} = 1.0^2$ (solid line), 1.33^2 (dashed line), 1.5^2 (dotted-dashed line), and 1.7^2 (dotted line). The associated plasma edge of each spectrum in nanometres is shown by a labelled vertical line of the same style. **c** Plasma edge against refractive index of host for measured (Expt.) and modelled (Brugg.) spectra, and the relationship predicted by the tri-helical metamaterial (THM) model, reproduced from Salvatore et al. [9] Reprinted (adapted) from [4] with permission from the American Chemical Society

6.4 Discussion

Three effective medium models have been compared for their ability to accurately reproduce the specular reflectance spectra of multi-domain gyroid optical metamaterials across a broad range of incident angles. The optimal model was determined to be a Bruggeman effective medium consisting of a random wire array. This model additionally reproduced previously published results tracking the variation in normal incidence reflectance spectra of gold gyroid optical metamaterials as a function of host refractive index and volume fill fraction.

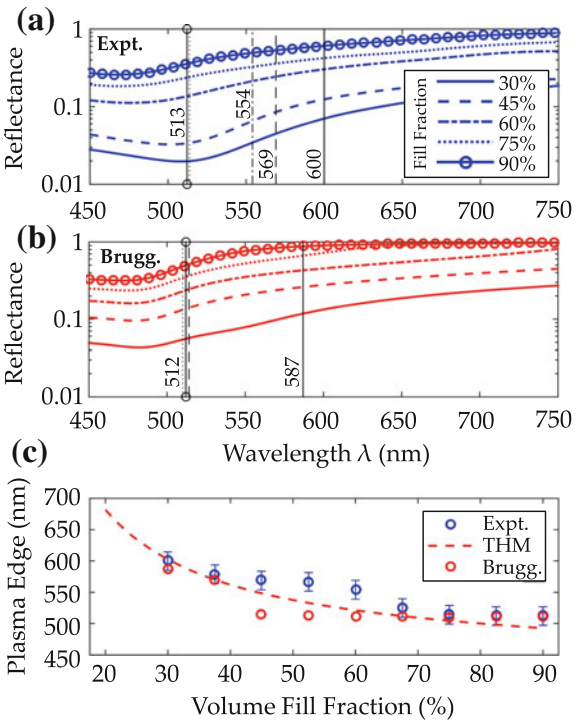

Fig. 6.7 Variation in normal incidence reflectance spectra and plasma edge as a function of gold volume fill fraction. **a** Measured normal incidence reflectance spectra of gold gyroid optical metamaterials with volume fill fractions of 30% (solid line), 45% (dashed line), 60% (dotted-dashed line), 75% (dotted line), and 90% (solid line with circles). Data reproduced from Salvatore et al. [9] **b** Modelled normal incidence reflectance spectra using the optimised Bruggeman model where f_1 of Eq. (6.4) is set to 0.30 (solid line), 0.45 (dashed line), 0.60 (dotted-dashed line), 0.75 (dotted line), and 0.90 (solid line with circles). The associated plasma edge of each spectrum in nanometres is shown by a labelled vertical line of the same style. **c** Plasma edge against volume fill fraction of gold for measured (Expt.) and modelled (Brugg.) spectra, and the relationship predicted by the tri-helical metamaterial (THM) model, reproduced from Salvatore et al. [9] Reprinted (adapted) from [4] with permission from the American Chemical Society

6.4.1 Bruggeman Random Wire Array

The failure of the Maxwell-Garnett theory to describe multi-domain gyroid samples is perhaps not surprising, since its validity is limited to low volume fractions of spherical inclusions that are spatially separated. The gyroid samples considered here consist of an interconnected, percolating network of gold struts. The better description of the experimental system by the Bruggeman model with spherical inclusions arises primarily from the fact that this model retains it validity for a high density of scatterers, expressed in the model by the fill fraction. The results of Fig. 6.4 indi-

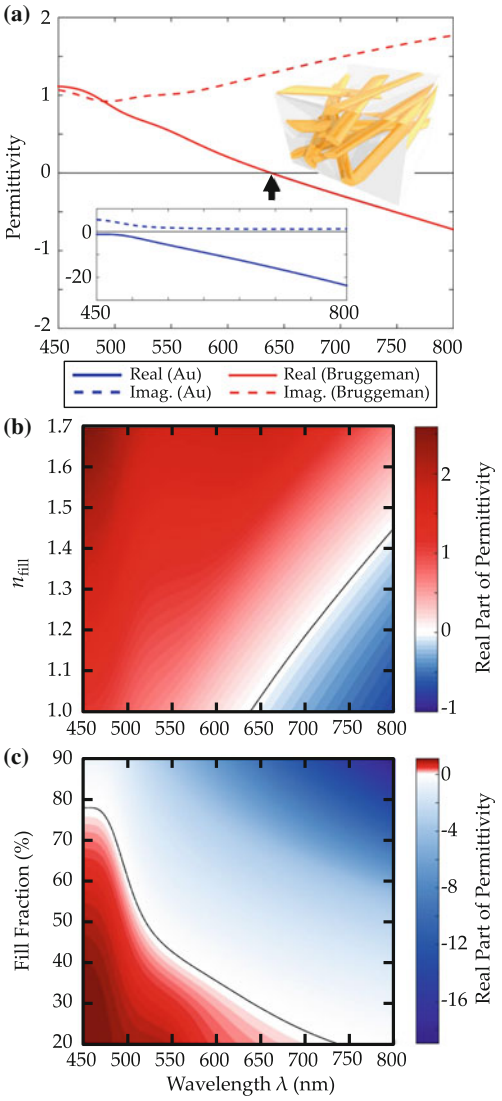

Fig. 6.8 Effective permittivity of multi-domain gyroid optical metamaterials derived from the Bruggeman effective medium theory. **a** Real (solid line) and imaginary (dashed line) parts of the effective permittivity $\varepsilon_{\text{eff}}(\omega)$ calculated using the Bruggeman theory by setting $\varepsilon_1(\omega) = \varepsilon_{\text{Au}}(\omega)$, $\varepsilon_2(\omega) = 1$, $f_1 = 0.3$, $A_1 = 0.66$, $A_2 = 0.34$, and $A_3 = 0$ in Eq. (6.4). The insets are a sketch of the equivalent structure corresponding to the optimised Bruggeman model (top), and the real (solid line) and imaginary (dashed lines) part of the permittivity of bulk gold $\varepsilon_{\text{Au}}(\omega)$ (bottom). **b** Variation of the real part of the effective permittivity $\Re\{\varepsilon_{\text{eff}}(\omega)\}$ with refractive index of the host medium. **c** Variation of the same with volume fill fraction of gold. Reprinted (adapted) from [4] with permission from the American Chemical Society

cate that a model based on an effective medium approach is able to approximate the random multi-domain gyroid network, despite the morphological dissimilarity.

While a model with a larger number of free parameters (i.e. the three depolarisation factors) is expected to improve the level of agreement with the data, it is revealing that fits of both reflected TE and TM polarised light result always in zero values for one of the depolarisation factors A_k. Since $A_k < 1/3$ corresponds to a prolate ellipse, with a divergence for $A_k \to 0$, the optimisation of the Bruggeman model with free A_k values results in an effective medium consisting of randomly oriented wires of elliptical cross section (see Fig. 6.8, top inset). While a random wire assembly is a better description than isolated individual scatterers for an interconnected gyroid network, the good agreement between fit and data is nevertheless surprising given that the Bruggeman theory does not model well percolating networks [10]. Although allowing for microscopic anisotropy within the Maxwell-Garnett model (i.e. ellipsoidal inclusions) might similarly improve upon the results of the equivalent model with spherical inclusions, this variant of the Maxwell-Garnett model would still suffer from a limited validity because of the high volume fill fractions of our samples and was therefore not considered.

6.4.2 *Effective Permittivity and Nanoporous Gold*

Like the classical wire-grid metamaterial, the gold gyroid optical metamaterial is shown to exhibit a strongly red-shifted plasma edge [11]. The effective permittivity $\varepsilon_{\text{eff}}(\omega)$ derived from the Bruggeman theory with optimised depolarisation factors, shown in Fig. 6.8a, has a crossover of the real part of the permittivity just below 650 nm (arrow). In contrast, the real part of the permittivity of the constituent gold does not cross the zero axis at any wavelength in the visible (bottom inset). Notwithstanding the effect of losses associated with the imaginary part of the permittivity, the gold gyroid optical metamaterial therefore behaves as both a dielectric ($\lambda \lesssim 650\,\text{nm}$) and metal ($\lambda \gtrsim 650\,\text{nm}$) in the visible. In the simple Drude model of the permittivity of a metal, this crossover is associated with the plasma frequency (plasma wavelength), an association which is hard to isolate in more complicated models (e.g. Drude–Lorentz) or experimentally measured permittivities. The previously introduced plasma edge is thus useful to characterise the optical response of the gyroid optical metamaterial, despite the lack of a direct correlation with prominent features in the permittivity plots. The variation of the predicted real part of the permittivity with refractive index of the host and fill fraction of gold is shown in Fig. 6.8b, c, respectively. Although quantitatively distinct, it is clear that the general behaviour of both the plasma edge (Figs. 6.6c, 6.7c) and the crossover wavelength (Fig. 6.8b, c) are broadly similar. Based on this and the good fit of the Bruggeman model to the specular reflectance spectra, we conclude that gyroid optical metamaterials averaged over many randomly oriented domains behave similarly to amorphous composites of air and gold (i.e. dilute metals), and therefore possess a similar response to nanoporous gold fabricated, for example, by dealloying [12–19].

6.4.3 Gyroid Surface and Morphology Effects

Although the optimised Bruggeman model is successful in predicting the optical properties of multi-domain gold gyroid optical metamaterials, it is by no means perfect and various dissimilarities exist between the measured and predicted spectra. Surprisingly, the measured reflectance spectra are generally higher than those predicted. This is most likely caused by the details of the gyroid surface.[7] For example, surface reconstruction (i.e. local reorientation) of the triblock terpolymer during thermal annealing can alter the in-coupling of light into the replicated gold gyroid network. Alternatively, the details of the gyroid fabrication process might affect the surface roughness and the volume fill fraction of gold near the top surface, accounting for the differences in the reflectivity.[8]

The relative decrease in the long wavelength reflectance at high angles of incidence predicted by the Bruggeman model, more prominent when spherical inclusions are assumed and not present in the data, may similarly be a result of the gyroid optical metamaterial having a somewhat larger volume fill fraction of gold at its surface compared to a planar cut across the gyroid morphology. An incorrect assumption of the fill fraction during optimisation of the depolarisation factors may also help to explain the relative inaccuracy of the model at intermediate fill fractions (i.e. between about 40 and 70%) compared to the relative accuracy of the same model with respect to increasing refractive index of the host. However, it is worthy of mention that the fabrication of gyroid optical metamaterials with increased fill fraction, and the accurate measurement of the fill fraction, are difficult compared to infiltration of the metamaterial with varying refractive index media [9]. Results of the former experiments should therefore be treated with some caution.

Finally, whereas all of the effective medium models considered are insensitive to the absolute size of the sub-wavelength inclusions, it is known that the optical properties of gold gyroid optical metamaterials vary with unit cell size (cf. Chap. 2 Sect. 2.6 and Table 2.1) [9]. The results presented here are therefore limited to gold gyroids with a similar unit cell size (i.e. ≈ 60 nm), although the methodology can of course easily be extended to gold gyroids of other unit cell sizes. Despite the potential shortcomings of the relatively simple analytical models employed here, the application of more complicated analytical models would not alter the current conclusion: that multi-domain gold gyroid optical metamaterials behave substantially as if they were nanoporous gold.

[7] Although distinct, this argument anticipates some of the results presented in Chap. 7, which highlight the striking effect of the surface of the gyroid morphology on its optics.

[8] The surface roughness of the gyroid optical metamaterial is not taken into account here, unlike in Chap. 7, although the fabrication method reduces it greatly (Chap. 3).

6.5 Conclusion

In this chapter, the effective permittivity of multi-domain gold gyroid optical metamaterials was estimated by comparing the results of three effective medium theories to measured specular reflectance spectra over a range of angles of incidence. We show that a microscopically anisotropic Bruggeman theory with wire inclusions provides the best fit to the data, and that the optimised depolarisation factors imply a composite of randomly oriented gold wires of elliptical cross-section. That the averaged optical properties of multi-domain gyroid optical metamaterials are well described by an effective medium theory, including their variation with refractive index of the host and volume fill fraction of gold, contradicts previous assertions that the sub-wavelength structure alone necessarily distinguishes gold gyroid optical metamaterials from amorphous nanoporous gold [6].

This result is surprising given the experimental results obtained for large individual gyroid domains, which are revisited in Chap. 7 [6]. In particular, the gyrotropic transmission along one of the chiral gyroid axes that was attributed to the self-inductance of plasmonic modes is not captured by the effective medium model. If symmetry-related effects of the intricate gyroid structure do indeed contribute to the optical properties of a macroscopic sample consisting of numerous randomly oriented domains, it seems that this contribution is averaged out through the random alignment of the multi-domain gyroid assembly, as also appears to be the case for gyroid photonic crystals [20, 21]. This result therefore highlights the absolute necessity of using techniques such as solvent vapour annealing to create triblock terpolymer templates with sufficient long-range order if any effects unique to the particular sub-wavelength structure are to be observed.

References

1. Bergman, D. J., & Stroud, D. (1992). Physical properties of macroscopically inhomogenous media. *Solid State Physics*, *46*, 147–269.
2. Cai, W., & Shalaev, V. (2010). *Optical Metamaterials*. Berlin: Springer. ISBN 978-1-4419-1151-3.
3. Gaponenko, S. V. (2010). *Introduction to Nanophotonics*. Cambridge: Cambridge University Press. ISBN 978-0-521-76375-2.
4. Dolan, J. A., Saba, M., Dehmel, R., Gunkel, I., Gu, Y., Wiesner, U., et al. (2016). Gyroid optical metamaterials: Calculating the effective permittivity of multidomain samples. *ACS Photonics*, *3*, 1888–1896.
5. Bánhegyi, G. (1986). Comparison of electrical mixture rules for composites. *Colloid Polymer Science*, *264*, 1030–1050.
6. Vignolini, S., Yufa, N. A., Cunha, P. S., Guldin, S., Rushkin, I., Stefik, M. et al. (2012). A 3D optical metamaterial made by self-assembly. *Advanced Materials24*, OP23–OP27.
7. Salvatore, S. (2014). *Optical Metamaterials by Block Copolymer Self-Assembly (Springer Theses)*. Berlin: Springer. ISBN 3319053310.
8. Olmon, R. L., Slovick, B., Johnson, T. W., Shelton, D., Oh, S.-H., Boreman, G. D., et al. (2012). Optical dielectric function of gold. *Physical Review B*, *86*, 235147.

9. Salvatore, S., Demetriadou, A., Vignolini, S., Oh, S. S., Wuestner, S., Yufa, N. A., et al. (2013). Tunable 3D extended self-assembled gold metamaterials with enhanced light transmission. *Advanced Materials*, *25*, 2713–2716.
10. Kirkpatrick, S. (1973). Percolation and conduction. *Reviews of Modern Physics*, *45*, 574.
11. Pendry, J. B., Holden, A. J., Stewart, W. J., & Youngs, I. (1996). Extremely low frequency plasmons in metallic mesostructures. *Physical Review Letters*, *76*, 4773–4776.
12. Yu, F., Ahl, S., Caminade, A.-M., Majoral, J.-P., Knoll, W., & Erlebacher, J. (2006). Simultaneous excitation of propagating and localized surface plasmon resonance in nanoporous gold membranes. *Analytical Chemistry*, *78*, 7346–50.
13. Dixon, M. C., Daniel, T. A., Hieda, M., Smilgies, D. M., Chan, M. H. W., & Allara, D. L. (2007). Preparation, structure, and optical properties of nanoporous gold thin films. *Langmuir*, *23*, 2414–22.
14. Maaroof, A. I., Gentle, A., Smith, G. B., & Cortie, M. B. (2007). Bulk and surface plasmons in highly nanoporous gold films. *Journal of Physics D: Applied Physics*, *40*, 5675–5682.
15. Biener, J., Nyce, G. W., Hodge, A. M., Biener, M. M., Hamza, A. V., & Maier, S. A. (2008). Nanoporous plasmonic metamaterials. *Advanced Materials*, *20*, 1211–1217.
16. Sardana, N., Birr, T., Schlenker, S., Reinhardt, C. & Schilling, J. (2014). Surface plasmons on ordered and bi-continuous spongy nanoporous gold. *New Journaol of Physics16* .
17. Sardana, N., Heyroth, F., & Schilling, J. (2012). Propagating surface plasmons on nanoporous gold. *Journal of the Optical Society of America B*, *29*, 1778.
18. Lang, X., Qian, L., Guan, P., Zi, J., & Chen, M. (2011). Localized surface plasmon resonance of nanoporous gold. *Applied Physics Letters*, *98*, 2009–2012.
19. Maaroof, A. I., Cortie, M. B., & Smith, G. B. (2005). Optical properties of mesoporous gold films. *Journal of Optics A: Pure and Applied Optics*, *7*, 1464–4258.
20. Hyde, S. T., & Schröder-Turk, G. E. (2012). Geometry of interfaces: topological complexity in biology and materials. *Interface Focus*, *2*, 529–538.
21. Michielsen, K., De Raedt, H., & Stavenga, D. G. (2010). Reflectivity of the gyroid biophotonic crystals in the ventral wing scales of the Green Hairstreak butterfly, Callophrys rubi. *Journal of The Royal Society Interface*, *7*, 765–771.

Chapter 7
Single-Domain Gyroid Optical Metamaterials

In this chapter, we demonstrate that the observed linear dichroism in single-domain gyroid optical metamaterials fabricated using an 80 kg mol^{-1} polyisoprene-*b*-polystyrene-*b*-poly(ethylene oxide) (ISO) triblock terpolymer is a result of the termination of the single gyroid morphology at the surface of the metamaterial.[1] The surface termination breaks the cubic symmetry of the bulk gyroid geometry, and the effect of a particular termination may be modelled by the introduction of an anisotropic effective medium layer atop the isotropic bulk metamaterial. The results have far-reaching consequences for the use of optical metamaterials fabricated via self-assembly as the surface termination, unlike the bulk morphology, is exceptionally hard to control. Its striking effect upon the resulting optical properties is, however, interesting, enabling a wider range of metamaterial parameters than afforded by the bulk morphology alone.[2]

7.1 Methods

Details of the methods used may be found in Chap. 3. Briefly, thin films of an 80 kg mol^{-1} ISO triblock terpolymer were spun atop fluorine-doped tin oxide (FTO)-coated substrates from a 10% (w/w) solution of the terpolymer in anhydrous anisole. Samples were exposed to controlled solvent vapour atmospheres using a custom annealing chamber and experimental set-up. Dry nitrogen gas was bubbled through a chloroform reservoir and mixed with dry nitrogen before entering the annealing

[1] The single-domain gyroid optical metamaterial samples used here are replicated from the triblock terpolymer templates presented in Chap. 5.

[2] This chapter is based closely on the experimental section of: Dolan, J. A.,* Dehmel, R.,* Saba, M., Demetriadou, A., Gunkel, I., Gu, Y., Wiesner, U., Wilkinson, T. D., Hess, O., Baumberg, J. J., Steiner, U. & Wilts, B. D. *Metasurfaces atop metamaterials: surface morphology induces linear dichroism in gyroid optical metamaterials* (in press). *Equal contribution.

© Springer Nature Switzerland AG 2018

J. A. Dolan, *Gyroid Optical Metamaterials*, Springer Theses,
https://doi.org/10.1007/978-3-030-03011-7_7

chamber. The solvent concentration in the chamber was controlled by varying the mass flow rate of the two lines. Gyroid optical metamaterials were created from the terpolymer thin films by degradation of the polyisoprene (PI) block by exposure to UV light and its subsequent removal by immersion of the film in ethanol. The voided terpolymer network was replicated into gold by electrodeposition and the remaining terpolymer removed by exposure to oxygen plasma. Optical characterisation was performed using an automated reflection goniometer with fixed illumination optics and moveable detection optics. The illumination optics focused the light to a spot approximately 100 µm in diameter situated within a single domain of the gyroid optical metamaterial, about which the sample was rotated. Specular reflections were recorded at 2° intervals for azimuthal angles between 0 and 180°. Linear polarisers were placed at the output of the illumination optics and at the input of the detection optics. Reflectance spectra were normalised with respect to the reflectance of a silver mirror. Further characterisation was also performed using a custom-built automated transmission goniometer attached to an optical microscope. This allowed the sample to be rotated about the azimuthal axis whilst continuing to collect light from within the same domain. Transmission spectra were normalised with respect to the transmission of the FTO-coated glass substrate without the presence of the gyroid optical metamaterial. Linear polarisers were placed both before and after the sample. Simulations of the gyroid optical metamaterial were performed using a commercial-grade simulator based on the finite-difference time-domain (FDTD) method.[3]

7.2 Results

The physical mechanism underlying the observation of linear dichroism in cubic gyroid optical metamaterials is determined by measurement of the reflectance and transmittance spectra and comparison to both full 3D optical simulations and a simple analytical model.

7.2.1 Fabricated Morphology and Terminations

To confirm the successful fabrication of the gyroid optical metamaterial and to investigate the resulting surface morphology, we employ optical and scanning electron microscopy (Fig. 7.1). The scanning electron micrograph of a single domain (Fig. 7.1a) confirms the gyroid morphology and highlights the long range order of the solvent-annealed triblock terpolymer template used to fabricate the metamaterial (cf. Chap. 5). The arrangement and symmetry of the pores in Fig. 7.1a is consistent with a ⟨110⟩ inclination (direction) of the gyroid being oriented normal to the

[3] Sample fabrication was performed by the author and Raphael Dehmel. Optical simulations and analytical modelling were performed by Dr. Matthias Saba.

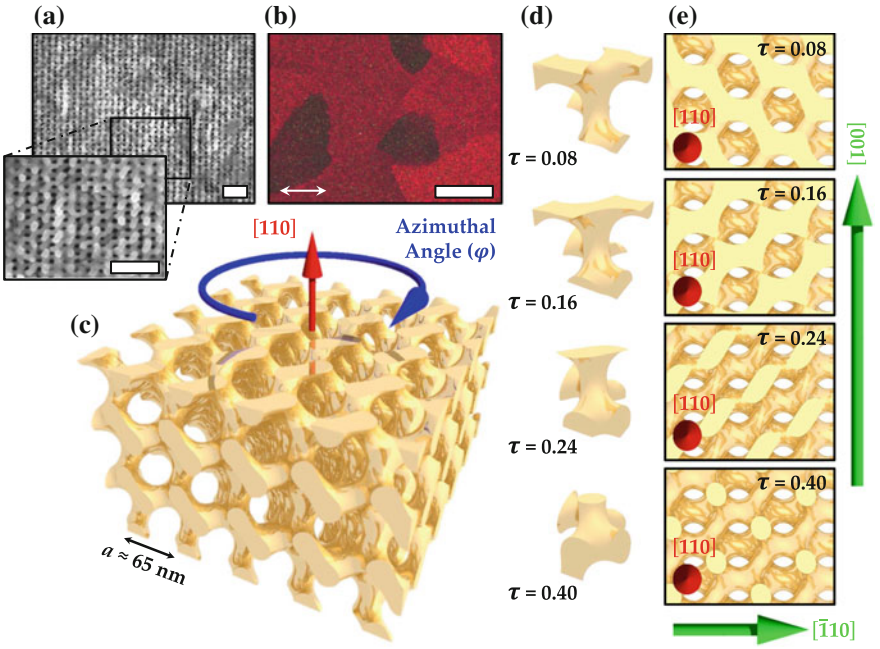

Fig. 7.1 Single-domain gyroid optical metamaterials and example terminations. **a** Scanning electron micrographs of a single domain of the gold gyroid optical metamaterial. Scale bars: 200 nm. **b** Optical micrograph of multiple domains (randomly oriented in-plane) of the gold gyroid optical metamaterial seen in reflection. The arrow shows the parallel orientation of the polariser and analyser. Scale bar: 50 µm. **c** Schematic of the single gyroid morphology, highlighting the [110] direction oriented normal to the substrate, and the definition of azimuthal angle (φ) used throughout. **d** Details of four example terminations of the single gyroid morphology, $\tau = 0.08$, 0.16, 0.24, and 0.40, where τ is the fractional distance of the terminating plane from the crystallographic origin in units of repeat distance in the negative [110] direction (i.e. $\sqrt{2}a$). **e** Surfaces of the single gyroid morphology viewed along the [110] direction for the same four possible terminations of the single gyroid morphology

plane of the substrate (cf. Fig. 2.2). This orientation has been observed previously in gyroid-forming ISO triblock terpolymers on occasions when the long-range order of the domains has been sufficiently large [1, 3–5]. The domain visible in Fig. 7.1a is very much larger than the field of view of the scanning electron microscope. Indeed, the full extent of these exceptionally large domains can only be observed using optical microscopy under linearly polarised light (Fig. 7.1b). As previously determined by Vignolini et al., the differently coloured regions in the optical micrograph correspond to different domains of the gyroid optical metamaterial [1]. These are randomly oriented in-plane, and the observed dichroism manifests as a shift in the effective plasma frequency (and reflectance) as a function of the relative orientation between the gyroid morphology in each domain and the polarisation of the light

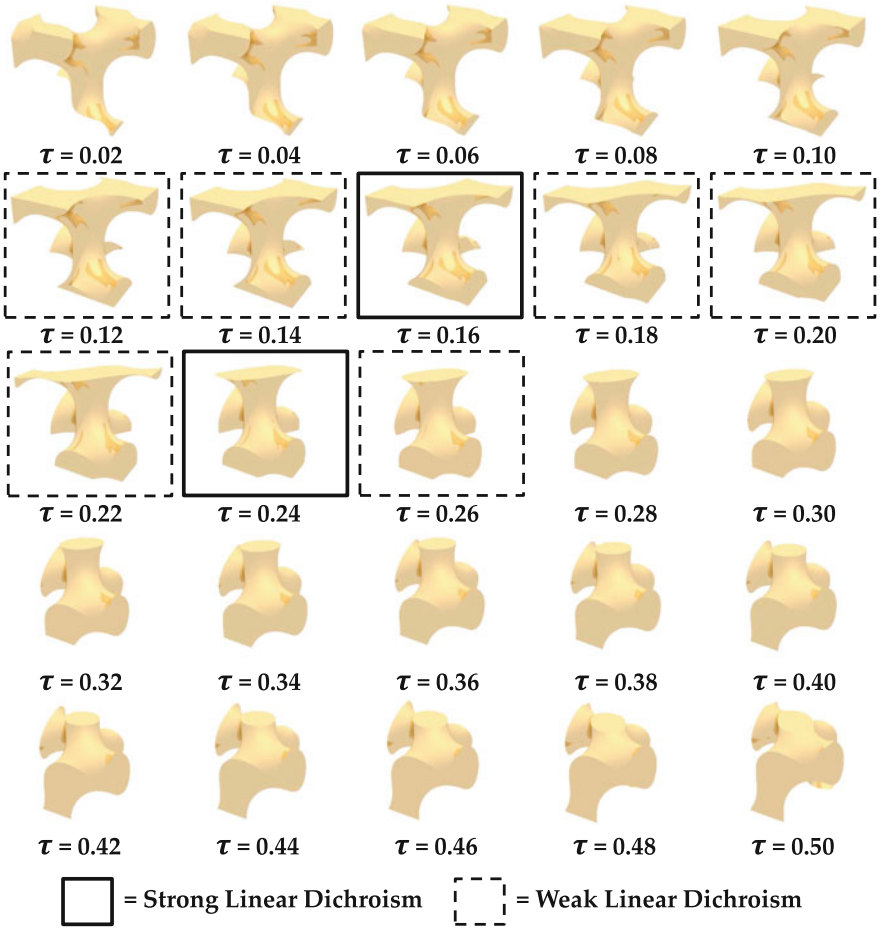

Fig. 7.2 Possible terminations of the single gyroid morphology. Possible terminations of the single gyroid morphology parameterised by τ, the fractional distance from the crystallographic origin to the terminating surface in units of repeat distance in the negative [110] direction. Termination planes separated by $\Delta\tau = 0.5$ are equivalent apart from a shift of the two-dimensional cross-section of the gyroid morphology in the [001] direction. Terminations with a strong (solid box; $\tau = 0.16$ and 0.24) and weak (dashed box; $\tau = 0.12$–0.14, 0.18–0.22, and 0.26) linear dichroism are highlighted (cf. Fig. 7.4e)

(Chap. 2 Sect. 2.6). Lighter and darker domains exhibit blue- and red-shifted plasma edges, respectively.

Unlike the single gyroid depicted in Fig. 7.1c, the fabricated gyroid optical metamaterial is not uniformly terminated (i.e. the top surface of the metamaterial is not a uniform cut through the single gyroid morphology). This is particularly clear in the inset of Fig. 7.1a, where the surface roughness and non-uniform termination of the metamaterial are evident. Example terminations of the single gyroid morphology

and their appearance when viewed along the [110] direction can be seen in Fig. 7.1d and e, respectively. The full range of possible terminations can be seen in Fig. 7.2. Terminations are characterised by the parameter τ, which describes the fractional distance of the terminating plane from the crystallographic origin in units of repeat distance in the negative [110] direction (i.e. $\sqrt{2}a$, where a is the unit cell size).[4] This origin is the same as that in Eq. (3.3) and that of the $I4_132$ space group (No. 214) [6]. Termination planes separated by $\Delta\tau = 0.5$ are equivalent apart from a shift of the two-dimensional cross-section of the gyroid morphology in the [001] direction. Of course, Fig. 7.1d and e depict uniform (although different) terminations, whereas the scanning electron micrograph in Fig. 7.1a reveals a highly non-uniform termination varying substantially between adjacent unit cells. Despite this, the termination visible in 7.1(a) may indeed be understood with reference to the uniform terminations in Fig. 7.1d and e, as will be explored below.

The physical origin of the surface roughness is the non-uniformity of the electrodeposition growth front during fabrication (Chap. 3 Sect. 3.6). The electrodeposited gold is anticipated to grow spherically outward from nuclei on the FTO-coated glass substrate before merging with similar growth fronts from neighbouring nuclei. Until this point, and for some time thereafter, the overall electrodeposition growth front is not at all uniform. This is therefore reflected in the non-uniformity of the termination at the point in time when the electrodeposition is stopped and the remaining terpolymer template is removed.

7.2.2 Experimental Dichroism

Linear dichroism is observed in the gyroid optical metamaterial through measurement of the reflectance and transmittance spectra at normal incidence under linearly polarised light (Fig. 7.3). The reflectance spectra of the gyroid optical metamaterial at four azimuthal angles, $\varphi = 0°$, 45°, 90°, and 135°, clearly demonstrate the linear dichroism previously visible in the optical micrographs (Fig. 7.3b).[5] The azimuthal angles are defined relative to the dichroism axis (i.e. the direction of maximum reflection). For the simulated spectra, the dichroism axis ($\varphi = 0°$) lies along the $[\bar{1}10]$ direction of the single gyroid morphology (see below; cf. Fig. 7.1e); for the measured spectra, it lies along the [001] direction (Fig. 7.3). The dichroism axes of the simulated and measured spectra are therefore misaligned by 90°, a discrepancy which will be discussed later. Unless otherwise stated, all figures show the azimuthal angle relative to the dichroism axis of the simulated gyroid.

As the azimuthal angle is increased from 0°, the reflectance of the metamaterial first decreases and then increases, reaching a minimum at 90° and a maximum (the

[4] Note that the termination parameter τ is only well defined for a specific ⟨110⟩ direction due to the non-symmorphic nature of the $I4_132$ (single gyroid) space group.

[5] It must be stressed that the linear dichroism observed here is entirely different to the birefringence observed in the associated triblock terpolymer templates in Chap. 5.

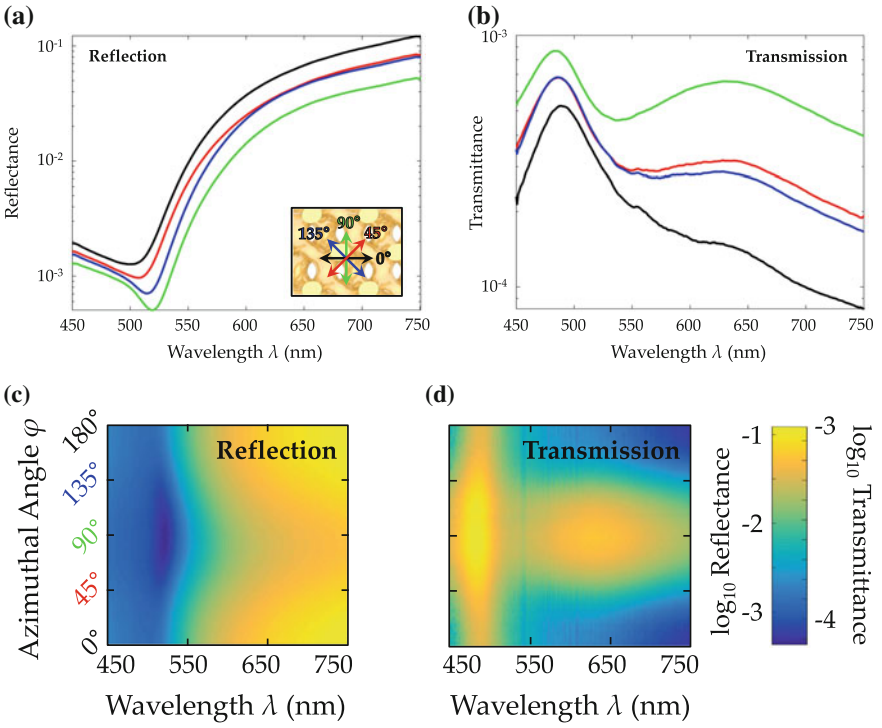

Fig. 7.3 Experimental reflectance and transmittance spectra. Normal incidence **a** reflectance and **b** transmittance spectra of the gold gyroid optical metamaterial under linearly polarised light at four selected azimuthal angles, $\varphi = 0°$ (black), 45° (red), 90° (green), and 135° (blue). Equivalent **c** reflectance and **d** transmittance spectra as a function of azimuthal angle. As shown in the inset, the azimuthal angles are defined with respect to the single gyroid morphology such that $\varphi = 0°$ lies along the measured dichroism axis, the [001] direction of the gyroid (cf. Fig. 7.1). The line plots are smoothed using a moving average filter with a span of 25 data points. Logarithmic colour scales

dichroism axis) at 180° (Fig. 7.3). By symmetry this is, of course, also 0°. The behaviour of the reflectance spectra at intermediate azimuthal angles can be seen in Fig. 7.3c. The general decrease and subsequent increase of the reflectance of the metamaterial, qualitatively symmetric about $\varphi = 90°$ and more pronounced at longer wavelengths, is evident. So too is the pronounced extinction peak at ≈ 525 nm, which becomes increasingly prominent at azimuthal angles between about 45 and 135°. This extinction peak is also seen to shift in wavelength, from ≈ 500 nm ($\varphi = 0°$) to ≈ 525 nm ($\varphi = 90°$).

Equivalent transmittance data at the same four azimuthal angles highlights a complementary trend: the transmittance first increases and then decreases as the azimuthal angle is increased from $\varphi = 0°$ (Fig. 7.3b and d). However, whereas the reflectance spectra exhibit only a single turning point, the transmittance data exhibit two clear peaks, one at low wavelength (≈ 475 nm) and the other at intermediate wavelength

(≈ 625 nm). Unlike the extinction peak in the reflectance spectra, the peaks in the transmittance data appear not to shift substantially. The narrow vertical feature which can be seen at ≈ 540 nm in Fig. 7.3d, which persists across all azimuthal angles, is a measurement artefact related to the ambient lighting conditions and the referencing procedure (Chap. 3 Sect. 3.7.3).

7.2.3 Uniform Terminations

Simulations were performed to corroborate the existence of the observed linear dichroism and to investigate the underlying mechanism. Simulated normal incidence reflectance spectra for the gold gyroid optical metamaterial under linearly polarised light are shown in Fig. 7.4. For each of the selected azimuthal angles, $\varphi = 0°$, 45°, 90°, and 135°, the reflectance spectra is simulated across the full range of possible terminations (cf. Fig. 7.2). It is apparent that for an azimuthal angle $\varphi = 0°$ (Fig. 7.4a), the simulated reflectance spectra are relatively insensitive to possible termination. This is not the case at higher azimuthal angles, for which the reflectance spectra are seen to vary considerably with termination (Fig. 7.4b–d). However, this effect appears confined to terminations $\tau \lesssim 0.3$. Given that the variation in reflectance spectra as a function of termination differs for each azimuthal angle, the simulations confirm theoretically the existence of a linear dichroism for uniformly terminated gyroid optical metamaterials.

The relationship between the termination of the simulated gyroid optical metamaterial and the observed dichroism becomes clearer when the reflectance at a single wavelength (650 nm) is plotted as a function of termination (Fig. 7.4e). The shift in reflectance with azimuthal angle (i.e. polarisation state of light) is one possible measure of the dichroism of the simulated gyroid metamaterial. The principal axis of the dichroism (the dichroism axis) is defined along the direction of greatest reflectance. The azimuthal angle associated with the simulated spectra exhibiting the greatest reflectance (i.e. $\varphi = 0°$, 45°, 90° or 135°) therefore corresponds very approximately to the true principal axis of the dichroism (discussed in greater detail below).

There is very little dichroism for terminations $\tau \gtrsim 0.3$. This behaviour can be understood as follows: the terminations in the range $\tau \approx 0.3$–0.4 are characterised by isolated protrusions approximately perpendicular to the surface of the metamaterial and approximately circular in cross-section (cf. Figs. 7.1d and 7.2). These terminations therefore behave as an effective medium layer atop the bulk which, as a result of the geometry and fill fraction of the protrusions, introduces no additional plasmonic resonance. The opposite is the case for the terminations $\tau \approx 0.22$–0.26: while still isolated, the protrusions are clearly anisotropic in cross-section, behaving therefore as an effective medium layer possessing an anisotropic plasmonic response (cf. Figs. 7.1d and 7.2). The reflectance spectra associated with the polarisations of light which strongly excite the longitudinal resonance of the protrusions (i.e. $\varphi = 0°$, 45°, and 90°) are thus depressed due to enhanced absorption. It is apparent that the prin-

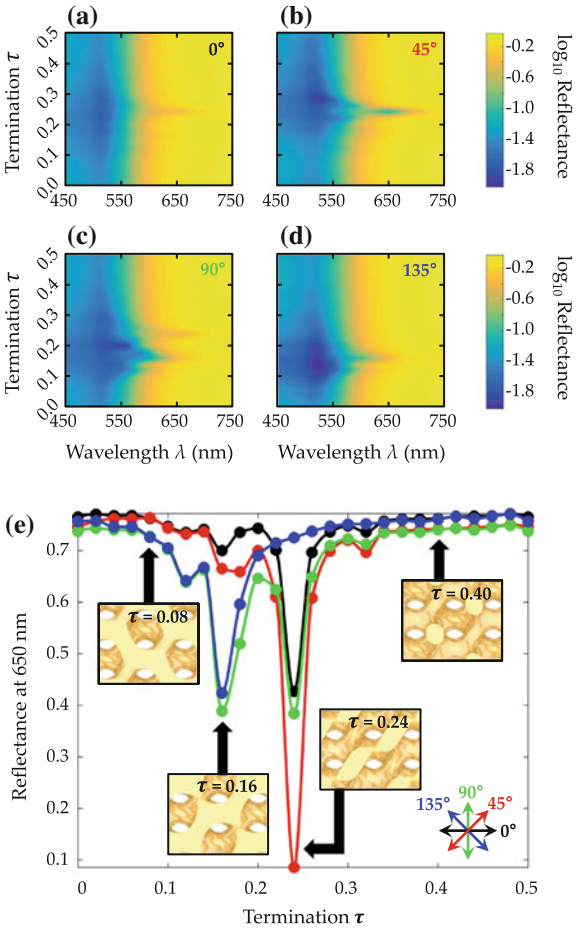

Fig. 7.4 Simulated reflectance spectra and linear dichroism as a function of termination. Simulated normal incidence reflectance spectra as a function of termination τ at azimuthal angles $\varphi =$ **a** 0°, **b** 45°, **c** 90°, and **d** 135°. Logarithmic colour scales. **e** Reflectance at 650 nm as a function of termination τ for the above four azimuthal angles, $\varphi = 0°$ (black), 45° (red), 90° (green), and 135° (blue). The azimuthal angles are defined with respect to the single gyroid morphology such that $\varphi = 0°$ lies along the simulated dichroism axis, which is the $[\bar{1}10]$ direction of the gyroid (cf. Fig. 7.1)

cipal axis of the dichroism for terminations $\tau \approx 0.22$–0.26 is thus close to azimuthal angle $\varphi = 135°$ (Fig. 7.4e).

For terminations $\tau \lesssim 0.2$ and $\gtrsim 0.4$, the protrusions are no longer fully isolated but form continuous current pathways (Figs. 7.1d and 7.2). These current pathways are either oriented along azimuthal angles $\varphi \approx 0°$ and $\approx 55°$ ($\tau = 0.16$) or $\approx 0°$ and $\approx 145°$ ($\tau = 0.08$). Despite their apparent similarity when viewed along the [110] direction, only one of these terminations, $\tau = 0.16$, results in a strong linear

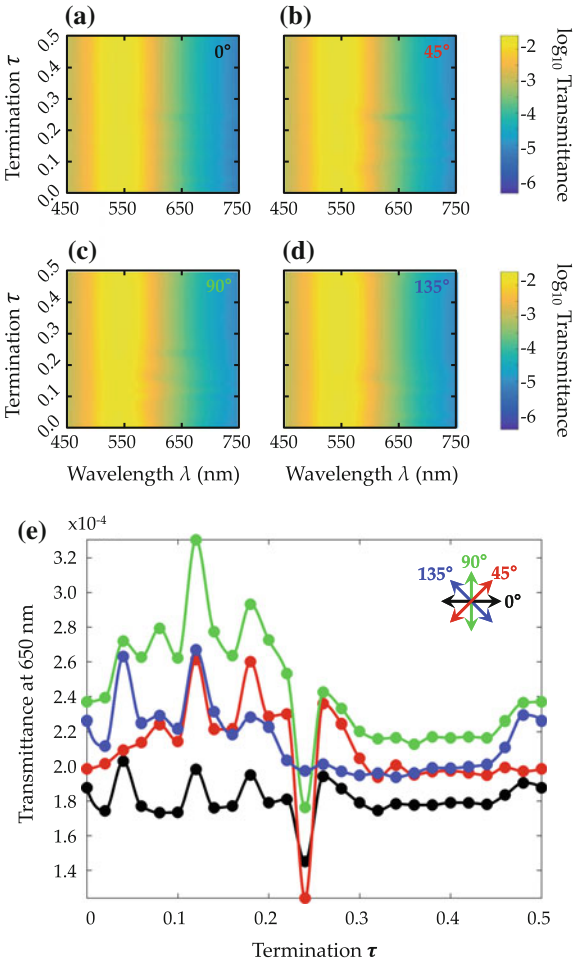

Fig. 7.5 Simulated transmittance spectra and linear dichroism as a function of termination. Simulated normal incidence transmittance spectra as a function of termination τ at azimuthal angles $\varphi =$ **a** 0°, **b** 45°, **c** 90°, and **d** 135°. Logarithmic colour scales. **e** Transmittance at 650 nm as a function of termination τ for the above four azimuthal angles, $\varphi = 0°$ (black), 45° (red), 90° (green), and 135° (blue)

dichroism, with a principal axis close to azimuthal angle $\varphi = 0°$ (Fig. 7.4e). Whereas the current pathways for the termination $\tau = 0.16$ are isolated in the orthogonal directions (i.e. along $\varphi \approx 0°$ and $\approx 145°$), this is not the case for the termination $\tau = 0.08$, which possesses additional current pathways in the orthogonal directions just below the surface. The nature of the linear dichroism (or absence thereof) for terminations $\tau \lesssim 0.2$ and $\gtrsim 0.4$ is discussed below.

The linear dichroism of simulated gyroid optical metamaterials is also evident in transmission (Fig. 7.5). However, whereas the simulated reflectance spectra exhib-

ited pronounced variations with termination, the same is not true of the simulated transmittance spectra (Fig. 7.5a–d). Instead, their more subtle variation with termination may be seen by investigating the transmittance at a single wavelength (650 nm; Fig. 7.5e). Unlike the equivalent metric in reflection (Fig. 7.4e), there is no termination which exhibits a noticeably stronger dichroism, although the termination $\tau = 0.24$ does exhibit a marked change of principal axis of the dichroism similar to that observed in reflection. It is unclear why there is an absence of a clear linear dichroism signal in the simulated transmittance spectra. Unlike the reflectance spectra, the transmittance spectra are affected by the termination at both the top and bottom interfaces of the simulated metamaterial slab. These two terminations are coupled by the fixed thickness of the slab, which may act to "cancel out" the observed dichroism. Irrespective, due to this result, only reflectance spectra are considered further.

7.2.4 Anisotropic Effective Medium Layer

The hypothesis that the surface of the gyroid optical metamaterial may behave as an effective medium for particular terminations may be explored using a simple analytical model. A subset of the simulated reflectance spectra corresponding to a particular termination for which the linear dichroism is especially strong ($\tau = 0.24$), and the results of the corresponding analytical model, are plotted in Fig. 7.6a. The analytical model is informed by the observation that at this particular termination, the gyroid optical metamaterial presents isolated anisotropic protrusions to the incident light (Fig. 7.1d and e). The analytical model therefore consists of a thin anisotropic Maxwell-Garnett effective medium layer atop an isotropic semi-infinite homogeneous medium.[6] The anisotropic effective medium layer is considered to consist of isolated ellipsoidal scatterers, whereby the orientation and ratio of the axes of the ellipsoids are based on the geometry of the protrusions of the gyroid. The effective permittivity along each of the principal axes of the ellipsoidal inclusions is given by [7][7]

$$\varepsilon^{i}_{\text{eff}}(\omega) = \varepsilon_2(\omega)\frac{\varepsilon_2(\omega)(1-f_1)(1-A_i) + \varepsilon_1(\omega)(f_1 + A_i(1-f_1))}{\varepsilon_2(\omega) + A_i(1-f_1)(\varepsilon_1(\omega) - \varepsilon_2(\omega))}, \tag{7.1}$$

where $\varepsilon^{i}_{\text{eff}}(\omega)$ is the effective permittivity of the i^{th} principal axis of the effective medium, $\varepsilon_1(\omega)$ is the permittivity of the inclusion, $\varepsilon_2(\omega)$ is the permittivity of the host, f_1 is the volume fraction of the inclusion, A_i is the depolarisation factor corresponding to the i^{th} principal axis of the composite, and ω is the frequency. The depolarisation factors A_i are given by [7]

[6] Previously, a multi-domain gyroid optical metamaterial was modelled using a Bruggeman effective medium model (Chap. 6). However, a Maxwell-Garnett model is used here as it better describes the dissimilarity between the morphology of the inclusions and the matrix in the thin anisotropic layer.

[7] This is the explicit (and anisotropic) form of Eq. 6.1.

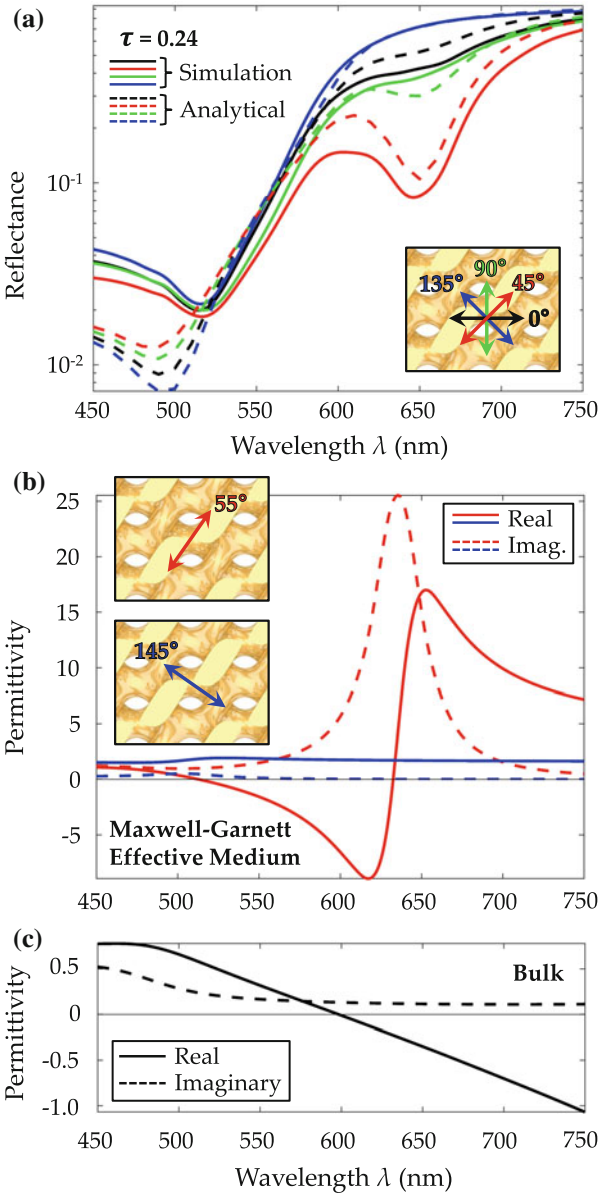

Fig. 7.6 Simulated and analytical reflectance spectra and the calculated permittivities of the Maxwell-Garnett effective medium layer and bulk srs-net gyroid. **a** Simulated (solid lines) and analytical (dashed lines) reflectance spectra at azimuthal angles $\varphi = 0°$ (black), 45° (red), 90° (green), and 135° (blue). **b** Real (solid lines) and imaginary (dashed lines) parts of the permittivities of the Maxwell-Garnett effective medium layer parallel ($\varphi = 55°$; red) or perpendicular ($\varphi = 145°$; blue) to the long axes of the effective medium ellipsoidal inclusions. **c** Real (sold line) and imaginary (dashed line) parts of the bulk permittivity of the srs-net gyroid

$$A_i = \frac{\prod_{k=1}^{3} a_k}{2} \int_0^\infty \frac{\mathrm{d}x}{\left(a_i^2 + x\right)\sqrt{\prod_{k=1}^{3}\left(a_k^2 + x\right)}}, \tag{7.2}$$

where a_k are the principal axes of the ellipsoid. When the short axes of the ellipsoid are equal (i.e. $a_1 = a_2$), the integrals evaluate to the closed form expressions

$$A_1 = A_2 = \frac{1}{2}\left(\frac{r^2}{r^2-1} - \frac{r\cosh^{-1}(r)}{\left(r^2-1\right)^{3/2}}\right) \tag{7.3}$$

and

$$A_3 = 1 - 2A_1 = -\frac{1}{r^2-1} + \frac{r\cosh^{-1}(r)}{\left(r^2-1\right)^{3/2}}, \tag{7.4}$$

where $r = a_3/a_1$ is the aspect ratio of the ellipsoids. The permittivity of the inclusion in the effective medium model is set equal to that of bulk gold as measured by Johnson and Christy [8]. The Maxwell-Garnett effective medium anisotropic layer is $0.12a$ (i.e. $\approx 8\,\mathrm{nm}$) thick with an effective fill fraction of gold $f_1 = 0.2$, calculated by numerically integrating the level set gyroid from $\tau = 0.24$ to 0.32. The constituent ellipsoids (spheroids) have an aspect ratio $r = 3.2$. The effective refractive index of the isotropic bulk was derived via homogenisation from an srs-net model of the single gyroid (cf. Fig. 2.2). Although a different approach to the tri-helical metamaterial (THM) model, which approximated the single gyroid as three disconnected helices, the effective refractive indices derived from both the srs-net and THM models are in this case very similar [3, 9, 10].

The permittivities of the anisotropic effective medium layer and isotropic srs-net bulk gyroid are shown in Fig. 7.6b and c, respectively. Parallel to the long axis of the anisotropic protrusions ($\varphi = 55°$), the effective medium exhibits a resonance at $\approx 630\,\mathrm{nm}$, which suppresses reflectance close to, and particularly above, that wavelength (Fig. 7.6b). In contrast, perpendicular to the long axis of the anisotropic protrusions ($\varphi = 145°$), the effective medium layer behaves as a low refractive index dielectric and is therefore almost transparent at normal incidence. The permittivity of the isotropic homogeneous medium, which models the bulk response of the gyroid optical metamaterial, can be seen in Fig. 7.6c.[8]

The analytical reflectance spectra predict a lower extinction peak ($\approx 500\,\mathrm{nm}$) and lower reflectance at low wavelength ($\lesssim 525\,\mathrm{nm}$) than the simulated reflectance spectra. Also, whereas the low wavelength analytical spectra exhibit a dichroism principal axis close to $\varphi = 45°$, the principal axis of the simulated spectra appears close to 135°. This is the result of a reversal in relative magnitudes of the real part of the parallel and perpendicular permittivities at $\approx 550\,\mathrm{nm}$ (Fig. 7.6b). Despite these issues, the analytical model successfully captures the appearance of a second

[8] Note the broad similarity between the permittivity of the srs-net bulk gyroid optical metamaterial and that derived for multi-domain samples, most particularly in the behaviour of the real part (cf. Fig. 6.8a).

extinction peak at higher wavelength (≈ 650 nm) and the linear dichroism otherwise absent from the bulk analytical model of the gyroid metamaterial. The success of such a simple analytical model based upon the geometry of the protrusions of the gyroid metamaterial at this termination ($\tau = 0.24$) corroborates the hypothesis that the surface of the gyroid optical metamaterial may indeed be considered an effective medium and that the linear dichroism does therefore result from the termination of the gyroid morphology.

7.2.5 Accounting for Non-uniform Terminations

Due to the necessary treatment of the simulated gyroid optical metamaterials as uniformly terminated, obvious dissimilarities exist between the measured and simulated reflectance spectra presented thus far (cf. Fig. 7.3a). Firstly, whereas the experimental spectra exhibit at most a single extinction peak irrespective of azimuthal angle, the simulated spectra can exhibit up to two such peaks. Secondly, the simulated reflectances are far higher than those measured experimentally.

The simulated spectra are therefore averaged over a range of uniform terminations to take into account the non-uniformity of the termination of the fabricated gyroid optical metamaterials (Fig. 7.7). The surface roughness of the metamaterial is also accounted for (Eq. (3.4)). However, the agreement between the simulated and measured spectra is sensitive to the range of terminations over which the spectra are averaged. In particular, of the two terminations which exhibit the strongest linear dichroism ($\tau = 0.16$ and 0.24), one exhibits a principal axis oriented $90°$ ($\tau = 0.14$–0.18; Fig. 7.7a) and the other $45°$ ($\tau = 0.22$–0.26; Fig. 7.7b) from that observed experimentally. Averaging over a broader range of terminations ($\tau = 0.02$–0.50; Fig. 7.7c) may reorient the principal axis or diminish the resulting dichroism.

Using an appropriate range of terminations, both sets of spectra now exhibit only a single extinction peak at ≈ 525 nm, a sizeable linear dichroism, and a similar magnitude of reflectance over the entire wavelength range (Fig. 7.7a). However, whereas the dichroism of the measured reflectance spectra is strong at all wavelengths, the dichroism of the simulated spectra weakens as the wavelength increases and becomes negligible at wavelengths $\gtrsim 650$ nm. Also, there is an apparent reorientation of the dichroism axis at low wavelengths ($\lesssim 550$ nm) for the simulated spectra. Despite these discrepancies between the two sets of spectra, it is clear that by taking into account the surface morphology of the gyroid optical metamaterial (i.e. by averaging over an appropriate range of possible terminations of the single gyroid morphology) the measured reflectance spectra can be adequately modelled.

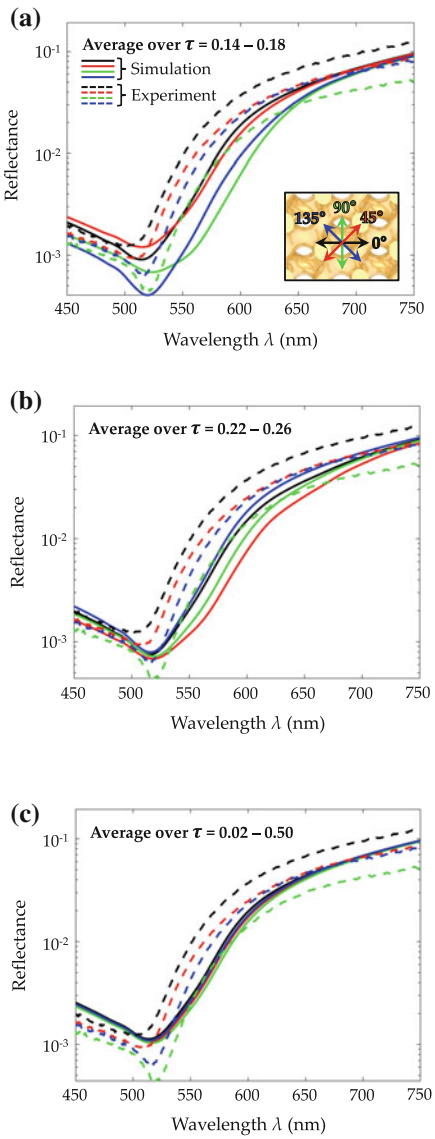

Fig. 7.7 Simulated reflectance spectra averaged over a range of terminations. Simulated (solid lines) and experimental (dash lines) normal incidence reflection spectra averaged over terminations $\tau =$ **a** 0.14–0.18, **b** 0.22–0.26, and **c** 0.02–0.50, and taking into account the surface roughness of the gyroid optical metamaterial, at four azimuthal angles, $\varphi = 0°$ (black), 45° (red), 90° (green), and 135° (blue). The inset shows the definition of azimuthal angle with respect to the dichroism axis of the simulated spectra, the $[\bar{1}10]$ direction of the single gyroid morphology, which differs from that of the measured spectra, the [001] direction

7.3 Discussion

The linear dichroism of gyroid optical metamaterials has been investigated both experimentally and theoretically. Despite the cubic symmetry of the single gyroid morphology, these metamaterials exhibit a clearly measurable linear dichroism in both reflection and transmission. Simulations based upon uniformly terminated

gyroid optical metamaterials imply a striking variation in reflectance with termination of the gyroid. It is therefore hypothesised that the observed linear dichroism arises from anisotropic plasmonic resonances at the surface of the metamaterial associated with a subset of these terminations. The reflectance spectra resulting from the termination exhibiting the strongest dichroism ($\tau = 0.24$) can be adequately reproduced using a model consisting of a thin anisotropic effective medium layer atop the isotropic bulk metamaterial. The parameters of this effective medium layer are based on the geometry of the protrusions at the termination of the gyroid morphology, thereby mimicking the plasmonic resonance and corroborating this hypothesis. Finally, accounting for both the non-uniformity of the termination and the surface roughness of the fabricated gyroid optical metamaterial, the simulated reflectance spectra reproduce the measured spectra. This corroborates the hypothesis that the observed linear dichroism is indeed the result of the surface termination or, more broadly, the surface morphology, of the fabricated gyroid optical metamaterial.

7.3.1 Deep Sub-wavelength Sensitivity

The terminations of the gyroid morphology have been parameterised by τ, the fractional distance from the crystallographic origin to the terminating surface in units of repeat distance in the negative [110] direction (i.e. $\sqrt{2}a$). This disguises the length scale over which striking differences in the simulated reflectance spectra are observed: terminations which exhibit a strong dichroism are separated from those which exhibit almost no dichroism by as little as $\Delta\tau \approx 0.06 \approx 5\,\text{nm}$ (Fig. 7.4e). Not only is this length scale deeply sub-wavelength (i.e. $\Delta\tau \approx \lambda/100$) but it is also substantially smaller than the unit cell size ($\approx 65\,\text{nm}$). The bulk optics of the gyroid optical metamaterial therefore appear sensitive to the existence and morphology of features on the length scale of only a few nanometres. Furthermore, these features, associated with the various terminations of the gyroid morphology, break the cubic symmetry of the gyroid and result in an apparent and unexpected linear dichroism for an otherwise isotropic bulk metamaterial.

7.3.2 Nature of the Linear Dichroism

Only some terminations appear to contribute substantially to the linear dichroism of the metamaterial (e.g. $\tau = 0.16$ and 0.24). The nature of the linear dichroism for the termination $\tau = 0.24$ seems clear: the associated protrusions are isolated and anisotropic in cross-section (Fig. 7.1d; $\tau = 0.24$) and therefore exhibit an anisotropic plasmonic response. We use the term "isolated" despite the fact that all protrusions clearly form part of the continuous gyroid morphology and are therefore electrically connected. Our justification is that such protrusions are only connected to the continuous gyroid morphology perpendicular to the polarisation vector of the incoming

light, and that no currents may therefore be excited within the plane of the protrusions (at least at normal incidence). They are thus similar (if not identical) to truly isolated plasmonic scatterers, evidenced by the success of the analytical effective medium model (Fig. 7.6a).

Further evidence that only terminations which are isolated (i.e. separated vertically from the remainder of the bulk gyroid morphology) support localised plasmonic resonances can be found in the behaviour of the terminations $\tau = 0.0$–0.1, 0.4–0.5, and 0.16. For the termination $\tau = 0.16$, which exhibits a strong linear dichroism, there exist current pathways along azimuthal angles $\varphi \approx 0$ and $\approx 55°$. These current pathways allow current flow excited by light polarised along those same directions and hinder current flow excited by light polarised along the orthogonal directions, in which the pathways are well isolated from one another (i.e. $\varphi \approx 90$ and $\approx 145°$; Figs. 7.1d and 7.2). It is therefore only the latter polarisation states of light which appear to support a localised plasmonic resonance and the associated enhanced absorption (Fig. 7.4e).

For the terminations $\tau = 0.0$–0.1 and 0.4–0.5, despite the existence of similar current pathways along azimuthal angles $\varphi \approx 0$ and $\approx 145°$, the dichroism is almost negligible. This may be explained by noting that the current pathways for these terminations are not well isolated from one another in the orthogonal directions due to additional pathways just below the surface (Figs. 7.1d and 7.2). Together these two sets of current pathways allow current to flow in all directions within the surface. This is a characteristic of the bulk gyroid optical metamaterial and the response of the associated terminations is therefore highly reminiscent of the response of the bulk alone. Put differently, without the isolation between the current pathways and the remainder of the gyroid morphology, the localised plasmonic resonances which lead to a linear dichroism cannot be supported.

It should be stressed that the results presented here are applicable only to gyroid optical metamaterials with a volume fill fraction $\lesssim 30\%$. As the volume fill fraction increases, previously isolated protrusions form increasingly larger "bridges" between neighbours, and the resulting connectivity diminishes the associated linear dichroism. Although not explored in detail here, this changing morphology of the isolated protrusions with volume fill fraction is a compelling mechanism likely underlying the results of Salvatore et al., who demonstrated experimentally the reduction in linear dichroism with increasing fill fraction (cf. Chap. 6) [3].

7.3.3 Distribution of Terminations

The fabricated gyroid optical metamaterial possesses non-uniform terminations. These were taken into account by averaging the simulated reflectance spectra over a small range of terminations (e.g. $\tau = 0.14$–0.18; Fig. 7.7). The resulting linear dichroism of a non-uniformly terminated gyroid optical metamaterial is therefore a function of the distribution of terminations present. That the measured reflectance spectra can only be well modelled by a relatively narrow distribution of terminations

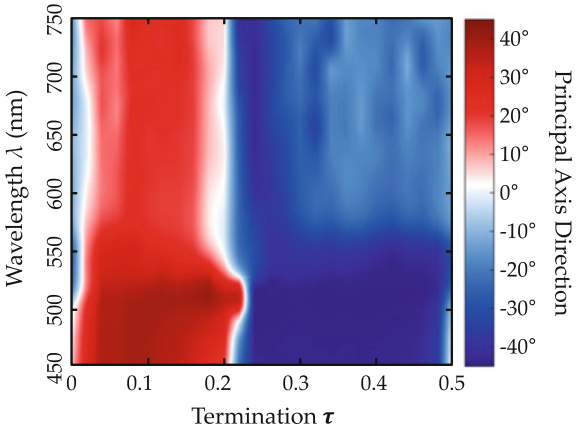

Fig. 7.8 Principal axis of the simulated linear dichroism. Direction of the principal axis as a function of wavelength and termination. Positive values (i.e. $0 \rightarrow 45°$) red; negative values (i.e. $-45 \rightarrow 0°$) blue

in the range $\tau = 0.14$–0.18, rather than, say, a distribution encompassing all possible terminations, implies that not all terminations (and the associated surface morphologies) are equally likely. The mismatch between the length scale of the assumed surface roughness of the metamaterial (90 nm) and the range of terminations implied to be present in the sample ($\Delta\tau = 0.04 \approx 4\,\text{nm}$) might appear a cause for concern. However, the two length scales are not directly comparable: whereas the former indeed describes the relevant surface roughness of the fabricated metamaterial, the latter characterises the morphology of terminations most prevalent in the sample.

The two terminations which exhibit the strongest linear dichroism ($\tau = 0.16$ and 0.24) exhibit different orientations of the principle axis. However, the dichroism axes of the measured and simulated spectra already differ with respect to the underlying single gyroid morphology. Whereas the measured dichroism axis lies along the [001] direction, the simulated dichroism axis lies close to the $[\bar{1}10]$ direction (cf. Fig. 7.1e). The precise direction of the principal axis of the simulated gyroid optical metamaterial, relative to the $[\bar{1}10]$ direction, may be seen in Fig. 7.8. The dichroism axis is calculated from the reflectance value at four azimuthal angles as[9]

$$\varphi_0 = -\frac{1}{2}\tan^{-1}\left(\frac{R_{90°} - R_{0°}}{R_{45°} - R_{135°}}\right), \tag{7.5}$$

where R_φ is the reflectance at azimuthal angle φ. For terminations $\tau \approx 0.0$–0.2, the principal axis is between ≈ 0 and $\approx 45°$; for terminations $\tau \approx 0.2$–0.5, it is between ≈ -45 (i.e. 135) and $\approx 0°$. For no terminations does the simulated principal axis of the dichroism approach the [001] direction (i.e. 90 or $-90°$). Although the most

[9]Note that $\tan^{-1}$ is implemented such that the quadrant of the computed angle is correctly returned depending on the signs of, in this case, the numerator and denominator of the argument.

likely cause of this discrepancy is a systematic error in the labelling of either the simulated or measured spectra, no such error has yet to be found. Interestingly, it appears as if there is also an inevitable reorientation of the principal axis as a function of wavelength for all terminations $\tau \approx 0.0$–0.2 and 0.3–0.5. The choice of terminations over which to average the simulated reflectance spectra can therefore only satisfy the required principal axis condition (and even then only approximately) for a portion of the spectrum ($\gtrsim$525 nm), notwithstanding the greater discrepancy above. Averaging over a different or broader range of terminations would diminish the resulting dichroism or reorient the principal axis at longer wavelengths.

Although a possibility, it is not anticipated that the distribution of terminations observed here would necessarily be observed for other similarly fabricated gyroid optical metamaterials. Indeed, the strength of the dichroism observed by Vignolini et al. (a shift of the extinction peak by $\approx$ 100 nm) [1], Salvatore et al. (a shift of the plasma edge by $\approx$ 15 nm) [3], and here (a shift of the extinction peak by $\approx$ 25 nm) are all significantly different despite only subtle variations in fabrication and sample conditions. So too are the principal axes, which are at 45° [1], 90° [3], and 0° relative to the [100] direction, respectively.[10] It therefore appears as if there is substantial and unexplained variation between the linear dichroism of similarly fabricated gyroid optical metamaterials, most likely caused by the precise termination and surface roughness of each sample. Indeed, this variation points further towards the sensitivity of the bulk optics of the sample to the precise and deeply sub-wavelength morphology of the surface termination.

7.3.4 Termination-Induced Anisotropy

That the linear dichroism of the gyroid optical metamaterial is a result of the termination of the gyroid morphology has a number of implications. Firstly, as the terminations presented by different orientations of the gyroid differ greatly, so too may the strength (or indeed the existence) of the linear dichroism. The results presented above are therefore only applicable to a single chirality of gyroid optical metamaterials for which the [110] direction is oriented perpendicular to the substrate. An enantiomorphic gyroid optical metamaterial, such as may spontaneously be formed during the self-assembly of the triblock terpolymer, would exhibit the same terminations (and therefore the same dichroism) with a reorientation of the principal axes of the dichroism.[11] Gyroid optical metamaterials with the directions ⟨100⟩ and ⟨111⟩ perpendicular to the substrate are highly desirable due to the possible existence of a

[10] It is assumed that the dichroism axis corresponds to the direction of the minimally red-shifted extinction peak identified by Vignolini et al. [1], and that Salvatore et al. [3] present data for the maximum and minimum reflectance spectra as a function of polarisation. However, neither point is explicit.

[11] The chirality of the single gyroid morphology adopted by the polyisoprene block of the triblock terpolymer is assumed to be entirely random in the absence of any molecular chirality.

strong circular dichroism in those directions [1, 2]. It remains to be seen whether a linear dichroism will also exist for those orientations of the gyroid morphology.

Secondly, these results demand a reassessment of the existing literature concerning the linear and circular dichroism of gyroid optical metamaterials. It is now clear that the assertion by Vignolini et al. that the linear dichroism of the gyroid optical metamaterial is a function of the orientation of the gyroid morphology is only partially correct: this is indeed the effect but it is the terminations which provide the underlying physical mechanism [1]. Similarly, it would be interesting to ascertain what effect differing terminations of the gyroid morphology may have on the previously simulated circular dichroism of the gyroid optical metamaterial along the ⟨100⟩ and ⟨111⟩ directions (Chap. 2 Sect. 2.6) [1, 2].

7.4 Conclusion

In this chapter, we have demonstrated that the observed linear dichroism of gyroid optical metamaterials is a result of the termination of the single gyroid morphology present at the surface of the metamaterial. Indeed, the anisotropic optical response of isolated protrusions associated with a subset of the possible terminations of the single gyroid morphology are the underlying physical mechanism for this otherwise anomalous observation in a cubic, and therefore isotropic, bulk metamaterial. The effect of these terminations may be understood (and modelled) as the presence of a thin anisotropic effective medium layer atop the remainder of the bulk metamaterial, whereby the parameters of the effective medium layer are informed by the geometry of the terminations.

This finding has significant consequences for the possible use of optical metamaterials fabricated via self-assembly. Previously, it was anticipated that only the bulk morphology of the self-assembled system would determine the optical properties of the resulting metamaterial, especially as the length scale of any surface morphology was necessarily deeply sub-wavelength. It is now clear that this is not the case and that the effect of the surface morphology may be both highly sensitive and striking (e.g. it may break the underlying symmetry of the bulk morphology). This poses new and particular challenges if attempting to use self-assembly as a means of reliably fabricating optical metamaterials with a desired set of optical properties. However, it also opens the possibility of further exploring interesting physics associated with surface states in three-dimensional optical metamaterials. By comparison, symmetry breaking by the judicious introduction of defects within the bulk of a double gyroid photonic crystal structure has led to the prediction and, latterly, observation of Weyl points and line nodes [11, 12]. There is therefore the tantalising possibility that the effect of terminations or similar “defects” in gyroid-structured optical metamaterials may yet yield similarly fascinating physics.

References

1. Vignolini, S., Yufa, N. A., Cunha, P. S., Guldin, S., Rushkin, I., Stefik, M., et al. (2012). A 3D optical metamaterial made by self-assembly. *Advanced Materials*, *24*, OP23–OP27.
2. Oh, S. S., Demetriadou, A., Wuestner, S., & Hess, O. (2013). On the origin of chirality in nanoplasmonic gyroid metamaterials. *Advanced Materials*, *25*, 612–617.
3. Salvatore, S., Demetriadou, A., Vignolini, S., Oh, S. S., Wuestner, S., Yufa, N. A., et al. (2013). Tunable 3D extended self-assembled gold metamaterials with enhanced light transmission. *Advanced Materials*, *25*, 2713–2716.
4. Stefik, M., Wang, S., Hovden, R., Sai, H., Tate, M. W., Muller, D. A., et al. (2012). Networked and chiral nanocomposites from ABC triblock terpolymer coassembly with transition metal oxide nanoparticles. *Journal of Materials Chemistry*, *22*, 1078–1087.
5. Salvatore, S. (2014). *Optical metamaterials by block copolymer self-assembly (Springer theses)*. Berlin: Springer. ISBN 3319053310.
6. Hahn, T. (2002). *International tables for crystallography*. Dordrecht: Published for the International Union of Crystallography by Kluwer Academic Publishers. ISBN 978-0-7923-6590-7.
7. Bánhegyi, G. (1986). *Comparison of electrical mixture rules for composites*, *264*, 1030–1050.
8. Johnson, P. B., & Christy, R. W. (1972). Optical constants of the noble metals. *Physical Review B*, *6*, 4370–4379.
9. Demetriadou, A., Oh, S. S., Wuestner, S., & Hess, O. (2012). A tri-helical model for nanoplasmonic gyroid metamaterials. *New Journal of Physics*, *14*, 083032.
10. Demetriadou, A., & Hess, O. (2013). Analytic theory of optical nanoplasmonic metamaterials. *Physical Review B*, *87*, 161101.
11. Lu, L., Fu, L., Joannopoulos, J. D., & Soljac, M. (2013). Weyl points and line nodes in gyroid photonic crystals. *Nature Photonics*, *7*, 294–299.
12. Lu, L., Wang, Z., Ye, D., Ran, L., Fu, L., Joannopoulos, J. D., et al. (2015). Experimental observation of Weyl points. *Science*, *349*(622–624), 101.

Chapter 8
Conclusion and Outlook

In this thesis, the fabrication and characterisation of gyroid optical metamaterials has been investigated with the aims of successfully and reliably producing single-domain samples and better understanding their unique optical properties.

8.1 Solvent Vapour Annealing of a Gyroid-Forming Triblock Terpolymer

In Part I, we presented results associated with the fabrication of triblock terpolymer templates by solvent vapour annealing (SVA). We showed in Chap. 4 that, unlike diblock copolymers, gyroid-forming triblock terpolymers were remarkably robust under SVA [9, 20]. Although it is only through the current study that this may be confirmed, it was a result anticipated by Epps et al. in 2006, who wrote, "we can conclude that processing methods leading to materials with triply periodic and multicontinuous network morphologies […] will be remarkably stable" [17]. However, an understanding of the thermodynamics and kinetics of the SVA of gyroid-forming triblock terpolymers is only the first step in the rational design of fabrication protocols for single-domain terpolymer templates for optical metamaterial applications. Indeed, although presented here latterly, the exceptional long-range order of the alternating gyroid domains presented in Chap. 5 (i.e. those exhibiting confined crystallisation) was first achieved through a somewhat tortuous ex situ optimisation procedure without the benefit of the crucial insights later offered by the in situ study. Further work on this and other polymer systems may now proceed with far greater rapidity, thereby minimising the efforts required to achieve single-domain samples of various self-assembled morphologies.

We also demonstrated in Chap. 5 that poly(ethylene oxide) (PEO) crystallites were both confined by, and aligned within, the single gyroid network of the solvent-annealed triblock terpolymer thin films. The result of such a crystallisation mechanism was an anisotropic optical response, highly reminiscent of the linear dichroism

© Springer Nature Switzerland AG 2018

J. A. Dolan, *Gyroid Optical Metamaterials*, Springer Theses,
https://doi.org/10.1007/978-3-030-03011-7_8

of gyroid optical metamaterials but resulting from a completely different physical mechanism. However, in both cases the anomalous optical anisotropy results from order on a length scale far smaller than the unit cell: the molecular anisotropy of aligned PEO crystallites and the form anisotropy of gyroid surface terminations. This therefore opens up the tantalising possibility of utilising complex hierarchical order within network-forming block copolymers to further design or enhance the resulting optical properties. Indeed, beyond amorphous-semicrystalline block copolymers, there are also amorphous-liquid crystalline block copolymers, which may similarly exhibit preferential alignment within accessible multicontinuous network phases. Unlike a semicrystalline block however, a liquid crystalline block would potentially allow for dynamic (e.g. electrically induced) reorientation or reorganisation of the block's constituent molecules and, therefore, any resulting optical properties.

8.2 Optical Anisotropy in Gyroid Optical Metamaterials

In Part II, the optical properties of gyroid optical metamaterials exhibiting both short- and long-range order were investigated. We showed in Chap. 6 that long-range order is indeed crucial for the metamaterial to exhibit anisotropic optical properties. However, thoroughly unexpected was the associated result that the single gyroid morphology appeared not to distinguish multi-domain gyroid optical metamaterials from amorphous nanoporous gold, contrary to previous assertions [14]. Indeed, it appears that unless procedures such as SVA are undertaken to fabricate triblock terpolymer templates with good long-range order, one could readily create optically equivalent materials by more conventional means.

Finally, in Chap. 7, the nature of the linear dichroism of single-domain gyroid optical metamaterials was revealed. Previously it had been assumed that the dichroism was entirely a result of the relative orientation between the polarisation of light and the single gyroid morphology (i.e. that the morphology was intrinsically optically anisotropic). Although phenomenologically correct, this is at odds with the cubic symmetry of the gyroid morphology, which dictates an isotropic optical response. Instead, we show that it is isolated protrusions at the surface termination of the metamaterial which break the effective symmetry of the single gyroid morphology and introduce an anisotropic plasmonic resonance. As anticipated, the bulk remains essentially isotropic. It may therefore be that the gyroid optical metamaterial is better conceived of not as a bulk homogenous metamaterial, but as a "metasurface atop a metamaterial", drawing upon the rich and extensive literature on metasurfaces whilst doing so [19].

8.3 Outlook

Whereas an analogy with metasurfaces may help one to conceptualise the optical properties of gyroid optical metamaterials, one may also think of employing block copolymer self-assembly directly to the efficient fabrication of large area metasurfaces. Indeed, the work presented in this thesis is relatively unusual in that good long-range order is desired in three-dimensional network morphologies. Other applications of network-forming block copolymers tend not to require equivalent long-range order, their efficacy instead deriving from their self-supporting and continuous nature, and their large specific surface area. Significant research has instead been undertaken to achieve excellent long-range order in the one- and two-dimensional morphologies most often required for planar nanolithographic applications. It may therefore be interesting to capitalise on such research and explicitly consider the fabrication of thin (i.e. one or two unit cell) block copolymer films of reduced dimensionality as templates for bottom-up metasurface fabrication. Certainly this would avoid issues associated with the high optical losses upon propagation of light through bulk plasmonic metamaterials, and would exploit the striking (indeed dominant) effect of surface morphology identified here. Such work could draw upon new opportunities to create block copolymer "meshes" (i.e. thin interconnected layered structures) through a mixture of SVA and "directed self-assembly", the combination of top-down and bottom-up fabrication techniques [8]. Indeed, these mesh structures are remarkably similar to classic fishnet metamaterials, which are well known to exhibit a negative refractive index in the near infrared if appropriately designed [4, 18]. There is therefore ample scope to reconsider many existing planar block copolymer systems as potential optical metamaterial templates.

Considering once again the gyroid, directed self-assembly methods may similarly help to realise the fabrication of a single-domain gyroid optical metamaterial of truly macroscopic proportions (e.g. spanning the entire substrate), with chosen in- and out-of-plane orientations. Various techniques to direct the self-assembly of block copolymers have been attempted (e.g. the application of shear and electric fields, or temperature gradients) and have been reviewed previously [13]. Control of the orientation of the gyroid phase has been attempted via the orientation of another phase, from which the gyroid forms through an order-order transition upon removal of the field [1, 2, 6]. Of course, the observed robustness of the alternating gyroid morphology under SVA may make this particular approach a challenge if the effect of any field is similarly insufficient to cause a morphological transition in the terpolymer.

Instead, two related and particularly promising techniques, which have led to the demonstration of both excellent long-range order and orientational control of other block copolymer equilibrium morphologies, should perhaps be considered. These are are grapho- and chemoepitaxy. Both of these directed self-assembly methods seek to combine the accuracy and flexibility of standard top-down lithographic processes (e.g. electron beam lithography) with the small feature sizes and macroscopic coverage achievable through bottom-up self-assembly. Graphoepitaxy is the topographic patterning of a substrate surface with features that are commensurate with the over-

lying copolymer film, to induce order and orientation in the copolymer equilibrium morphology. For example, Bita et al. in 2008 used lithographically defined posts as a template for the spherical minority block of a polysytrene-*b*-polydimethylsiloxane (PS-*b*-PDMS) diblock copolymer [3]. The patterned features need not even necessarily be on the same length scale as the block copolymer equilibrium morphology, which increases the efficiency of the lithographic portion of the overall fabrication procedure [12]. Chemoepitaxy is the chemical patterning of a substrate surface, whereby the ordering and orientation is not induced by physical boundaries but rather by preferential thermodynamic interactions between patterned areas and the overlying block copolymer. For example, Kim et al. in 2003 demonstrated the epitaxial self-assembly and perfect registration of diblock copolymer lamellae on a surface chemically patterned with a self-assembled monolayer [15]. It remains to be seen whether either grapho- or chemoepitaxy can be successfully applied to gyroid-forming block copolymers. However, if so, it would allow for complete access to the full range of optical properties of gyroid optical metamaterials, including the linear and circular dichroism associated with alternative orientations of the morphology not considered here.

Despite the results presented in this thesis, much is still not fully understood about the optical response of gyroid optical metamaterials. Simulations do not yet excellently capture the experimentally measured reflectance and transmittance spectra, a situation which is complicated by the highly non-uniform surface morphology of the fabricated metamaterials. Indeed, although the data exist for the reflectance and transmittance spectra of single-domain gyroid optical metamaterials at oblique angles of incidence, corresponding simulations have proven particularly challenging. There may therefore still be much which can be learnt from this data, especially regarding the behaviour and effect of the anticipated longitudinal mode, which is not excited at normal incidence [16]. Similarly, the effect of surface termination on the previously identified circular dichroism could be fully explored in light of the findings made here. Every effort should thus be made to improve our ability to model these more complicated optical scenarios, and to guide these efforts with an increasing number of high quality measurements across numerous samples.

Experiment and theory may better agree if the surface termination of the fabricated gyroid optical metamaterials could be controlled. Although a potential method was used to create a (relatively) flat top surface for the multi-domain sample, this method arguably controls only the surface roughness and not the termination of the metamaterial. Given that the optical response of the metamaterial seems to vary strikingly for small variations in termination, it is likely that some form of top-down method will be required to control the termination to the tolerance required (i.e. a few nanometres). This may involve some form of chemical-mechanical planarisation similar to that practised in the semiconductor industry, or a more controlled means of back-filling the terpolymer template with metal. However, it is unclear whether the block copolymer itself would exhibit the required order. There is not yet any data on the local fluctuations of the alternating gyroid phase, and such fluctuations may affect our ability to accurately select a particular termination over a macroscopic area. Should we wish to exploit the surface termination of gyroid optical metama-

terials as an additional design parameter, then each of the above potential solutions will require further exploration.

Even if all existing fabrication challenges were overcome, it remains unclear whether a gyroid optical metamaterial would exhibit negative refraction, not least due to the losses associated with the gold from which it is fabricated [16]. Certainly the theoretical predictions do not appear favourable. However, as has already been discussed, the successful simulation of gyroid optical metamaterials remains a challenge and it would therefore perhaps be premature to discount the possibility of negative refraction entirely. Indeed, although the losses associated with plasmonic systems, including optical metamaterials, are a significant hurdle to their more widespread adoption, various research has demonstrated the potential to successfully mitigate such losses using gain media [5, 10, 11]. Although undoubtedly a challenge, the observation of negative refraction in gyroid optical metamaterials through their combination with gain media remains an exciting prospect.

Finally, it must be noted that, so far, only the single gyroid has received particular attention as a "self-assembled" optical metamaterial. Although there are excellent reasons for having chosen the single gyroid as an initial target morphology, it should be recognised that there exists a vast library of self-assembled morphologies which have yet to be explored as candidate optical metamaterials. Two obvious potential candidates for further study are the double gyroid morphology (achiral but nonetheless predicted to be negatively refracting if losses can be minimised) and the helical morphology found in some block copolymers possessing molecular chirality (which would undoubtedly exhibit a strong chiro-optic effect if correctly oriented) [7, 21]. It is only with ready and frequent exploration of this library, and the associated optical properties therein, that self-assembled optical metamaterials will find increasing application and that the true benefits of the bottom-up approach will finally be realised.

References

1. Dair, B. J., Avgeropoulos, A., Hadjichristidis, N., & Thomas, E. L. (2000). Mechanical properties of the double gyroid phase in oriented thermoplastic elastomers. *Journal of Materials Science*, *35*, 5207–5213.
2. Wang, C.-Y., & Lodge, T. P. (2002). Kinetics and mechanisms for the cylinder-to-gyroid transition in a block copolymer solution. *Macromolecules*, *35*, 6997–7006.
3. Bita, I., Yang, J. K. W., Jung, Y. S., Ross, C. A., Thomas, E. L., & Berggren, K. K. (2008). Graphoepitaxy of self-assembled block copolymers on two-dimensional periodic patterned templates. *Science*, *321*, 939–43.
4. Valentine, J., Zhang, S., Zentgraf, T., Ulin-Avila, E., Genov, D. A., Bartal, G., et al. (2008). Three-dimensional optical metamaterial with a negative refractive index. *Nature*, *455*, 376–379.
5. Khurgin, J. B., & Sun, G. (2012). Practicality of compensating the loss in the plasmonic waveguides using semiconductor gain medium. *Applied Physics Letters*, *100*, 011105.
6. Fairclough, J. P. A., Mai, S.-M., Matsen, M. W., Bras, W., Messe, L., Turner, S. C., et al. (2001). Crystallization in block copolymer melts: small soft structures that template larger hard structures. *The Journal of Chemical Physics*, *114*, 5425.

7. Hur, K., Francescato, Y., Giannini, V., Maier, S. A., Hennig, R. G., & Wiesner, U. (2011). Three-dimensionally isotropic negative refractive index materials from block copolymer self-assembled chiral gyroid networks. *Angewandte Chemie International Edition*, *50*, 11985–9.
8. Tavakkoli, K. G., Nicaise, A., Gadelrab, S. M., Alexander-Katz, K. R., Ross, A., & Berggren, K. K. (2016). Multilayer block copolymer meshes by orthogonal selfassembly. *Nature Communications*, *7*, 1–10.
9. She, M.-S., Lo, T.-Y., & Ho, R.-M. (2014). Controlled ordering of block copolymer gyroid thin films by solvent annealing. *Macromolecules*, *47*, 175–182.
10. Hess, O., Pendry, J. B., Maier, S. A., Oulton, R. F., Hamm, J. M., & Tsakmakidis, K. L. (2012). Active nanoplasmonic metamaterials. *Nature Materials*, *11*, 573–584.
11. Hess, O., & Tsakmakidis, K. L. (2013). Metamaterials with quantum gain. *Science*, *339*, 654–5.
12. Segalman, R. A., Yokoyama, H., & Kramer, E. J. (2001). Graphoepitaxy of spherical domain block copolymer films. *Advanced Materials*, *13*, 1152–1155.
13. Segalman, R. A. (2005). Patterning with block copolymer thin films. *Materials Science and Engineering: R: Reports*, *48*, 191–226.
14. Vignolini, S., Yufa, N. A., Cunha, P. S., Guldin, S., Rushkin, I., Stefik, M., et al. (2012). A 3D optical metamaterial made by self-assembly. *Advanced Materials*, *24*, OP23–OP27.
15. Kim, S. O., Solak, H. H., Stoykovich, M. P., Ferrier, N. J., De Pablo, J. J., & Nealey, P. F. (2003). Epitaxial self-assembly of block copolymers on lithographically defined nanopatterned substrates. *Nature*, *424*, 411–414.
16. Oh, S. S., Demetriadou, A., Wuestner, S., & Hess, O. (2013). On the origin of chirality in nanoplasmonic gyroid metamaterials. *Advanced Materials*, *25*, 612–617.
17. Epps, T. H., & Bates, F. S. (2006). Effect of molecular weight on network formation in linear ABC triblock copolymers. *Macromolecules*, *39*, 2676–2682.
18. Cai, W., & Shalaev, V. (2010). *Optical metamaterials*. Berlin: Springer. ISBN 978-1-4419-1151-3.
19. Yu, X., Luo, C., Zhao, Q., Yang, H., & Han, Y. (2014). Order-order transitions of a triblock copolymer with a homopolymer (ABC/A) blend film induced by saturated solvent vapor annealing. *Journal of Polymer Science, Part B: Polymer Physics*, *52*, 1030–1036.
20. Wu, Y.-H., Lo, T.-Y., She, M.-S., & Ho, R.-M. (2015). Morphological evolution of gyroidforming block copolymer thin films with varying solvent evaporation rate. *ACS Applied Materials & Interfaces*, *7*, 16536–16547.
21. Chiang, Y.-W., Ho, R.-M., Burger, C., & Hasegawa, H. (2011). Helical assemblies from chiral block copolymers. *Soft Matter*, *7*, 9797–9803.

Curriculum Vitae

James Andrew Dolan
Email: james.dolan@cantab.net
Institute for Molecular Engineering
Argonne National Laboratory
9700 S. Cass Ave.
Lemont, IL 60439
U.S.A.

Education:

University of Cambridge, UK
PhD, Departments of Engineering and Physics 2013–2016
Supervisors: Profs. Timothy D. Wilkinson, Ullrich Steiner & Jeremy J. Baumberg
Nano Doctoral Training Centre 2012–2013
Supervisor: Prof. Jeremy J. Baumberg
University of Oxford, UK
MEng in Engineering Science 2008–2012
Supervisor: Prof. Antonis Papachristodoulou

Postdoctoral Research:

Argonne National Laboratory & University of Chicago, USA
Postdoctoral Researcher, Institute for Molecular Engineering 2017 (Sept.–)
Supervisor: Prof. Paul F. Nealey
University of Fribourg, Switzerland
Postdoctoral Researcher, Adolphe Merkle Institute 2017 (3 mths.)
Supervisor: Prof. Ullrich Steiner

Publications:

Cebo, T., Aria, A. I., **Dolan, J. A.**, Weatherup, R. S., Nakanishi, K., Kidambi, P. R., Divitini, G., Ducati, C., Steiner, U. & Hofmann, S. Chemical vapour deposition

© Springer Nature Switzerland AG 2018

J. A. Dolan, *Gyroid Optical Metamaterials*, Springer Theses,
https://doi.org/10.1007/978-3-030-03011-7

of freestanding sub-60 nm graphene gyroids. *Applied Physics Letters* **111**, 253103 (2017).

Dehmel, R.,* **Dolan, J. A.**,* Gu, Y., Wiesner, U., Wilkinson, T. D., Baumberg, J. J., Steiner, U., Wilts, B. D. & Gunkel, I. Optical imaging of large gyroid grains in block copolymer templates by confined crystallization. *Macromolecules* **50**, 6255–6262 (2017). *__Equal contribution.__

Khan, A. A., Rughoobur, G., Kamarudin, M. A., Sepe, A., **Dolan, J. A.**, Flewitt, A. J., Qasim, M. M. & Wilkinson, T. D. Homologous binary mixtures and improved hole conduction of self-assembled discotic liquid crystals. *Organic Electronics* **36**, 35–44 (2016).

Dolan, J. A., Saba, M., Dehmel, R., Gunkel, I., Gu, Y., Wiesner, U., Hess, O., Wilkinson, T. D., Baumberg, J. J., Steiner, U. & Wilts, B. D. Gyroid optical metamaterials: calculating the effective permittivity of multidomain samples. *ACS Photonics* **3**, 1888–1896 (2016).

Harris, A. W. K., **Dolan, J. A.**, Kelly, C. L., Anderson, J. & Papachristodoulou, A. Designing genetic feedback controllers. *IEEE Transactions on Biomedical Circuits and Systems* **99**, 1 (2015).

Dolan, J. A., Wilts, B. D., Vignolini, S., Baumberg, J. J., Steiner, U. & Wilkinson, T. D. Optical properties of gyroid structured materials: from photonic crystals to metamaterials. *Advanced Optical Materials* **3**, 12–32 (2015).

Dolan, J. A., Anderson, J. & Papachristodoulou, A. A loop shaping approach for designing biological circuits. *IEEE 51st Annual Conference on Decision and Control*, 3614–3619 (2012).

Presentations:

Metasurfaces on metamaterials: surface modes induce linear dichroism in gyroid optical metamaterials. *American Physical Society March Meeting*, Los Angeles, USA (2018).

Gyroid optical metamaterials: termination-induced anisotropy. *Deutsche Physikalische Gesellschaft Spring Meeting*, Dresden, Germany (2017).

Aligned crystallization within a single gyroid network of a semicrystalline triblock terpolymer. *Deutsche Physikalische Gesellschaft Spring Meeting*, Dresden, Germany (2017).

Liquid crystal-infiltrated self-assembled gyroid optical metamaterials. *Enrico Fermi Summer Course in Complex Photonics*, Varenna, Italy (2015).